DET NATURVIDENSKABELIGE FAKULTET
KØBENHAVNS UNIVERSITET

Master's Thesis

Schrödinger-Poisson Calculations for Majorana Devices

Author: August Edwards Guldberg Mikkelsen

mwt655@alumni.ku.dk

Supervisors: Karsten Flensberg and Peter Krogstrup

April 18, 2017

Abstract

This thesis is concerned with modelling the electrostatic environment in devices used for realizing Majorana zero modes (Majorana devices). A simulation model based on the Schrödinger-Poisson method is developed and applied to two geometries.

The first geometry is a planar semiconductor-metal heterostructure contacted to a gate electrode and with translational invariance in two directions. We show how to set up the Schrödinger-Poisson method and include hybridization between the metal and semiconductor in the Schrödinger equation. Simulation results based on an InAs-Al junction are then presented, and it is found that the electrostatic interaction creates wells at the various heterointerfaces. These results are then compared to an approximation, where the hybridization is neglected, and it is found that the two approaches produce comparable results with some deviation at the semiconductor-metal interface. Subsequently, the effects of this deviation on the wave functions of the hybrid system is investigated and found to be negligible with our parameters.

The second geometry is a cross section of a hexagonal semiconductor nanowire with translational invariance in the longitudinal direction. The nanowire is covered by a metallic superconductor on two facets and placed on a dielectric layer in contact to a gate electrode. We show how set up the Schrödinger-Poisson method and argue that including hybridization between the semiconductor and superconductor is too computationally demanding. Consequently a simpler approach is used where the Schrödinger equation is solved only in the semiconductor region. Simulation results based on an InAs nanowire with Al as the superconductor are presented and good agreement with the results from the planar geometry is found.

Acknowledgements

First and foremost I would like to thank Karsten Flensberg for his supervision during this project. Though technically not my main supervisor, Karsten showed interest in my project from early on and has helped me throughout the whole process. Whether the problems I faced were related to mathematical derivations, numerical details or physical understanding, Karsten was always willing to discuss them and could usually explain things in a language that was easy to understand.

Secondly, I would like to thank my main supervisor Peter Krogstrup for getting me interested in this project and giving me many opportunities for developing intuition of the experimental side of things.

I would also like to Panagiotis Kotetes for helping me during the times, where Karsten was abroad, as well as in the final month of the thesis writing. Panagiotis always had a nice way of telling me when what I did was complete bullshit.

A special thanks goes to my beloved girlfriend Clara, who has been invaluable to me during the final months of this project. Without her encouragement and support this process would have been a lot tougher.

Lastly a big thanks goes to all the people in QDev, who have been a part of my life for the past two years. You made my time here a lot more enjoyable.

Contents

Introduction

0.1 Topological Quantum Computers - From Theory to Experiment

Realizing a universal quantum computer is an idea that has sparked enormous scientific interest in recent years. Fuelled by the rapid advances in quantum nanoelectronics and massive financial interest from the semiconductor industry, quantum computers have gone from being a purely theoretical idea to being the supercomputers of tomorrow.
The basic idea of a quantum computer is to use the superpositional nature of quantum states to store information. The fundamental unit of quantum information is the quantum bit (qubit), which is a two-level quantum system described by a state vector $|\Psi\rangle$ that can be in any superposition of the system's two eigenstates $|\Psi\rangle = a|0\rangle + b|1\rangle$. This is in contrast to a classical computer, where information is stored in classical bits that are either 0 or 1.

Currently one of the biggest challenges for engineering a quantum computer is the fast decoherence time of quantum states. This has led to an approach known as topological quantum computation [1], which, if realizable, is intrisically protected from local environmental noise. Loosely stated, the idea of a topological quantum computer is to store information in exotic many-particle states called Ising anyons, which, due to their non-trivial topological properties, are immune to local sources of decoherence. Furthermore these exotic topological states are believed to obey non-Abelian exchange statistics, which enables quantum computations to be performed via simple particle exchanges.

The simplest and most promising way of realizing Ising anyons are as Majorana zero modes in condensed matter systems [2]. Majorana zero modes are quasiparticle states, which, among other key properties, are an equal superposition of an electron and a hole. An obvious type of system for realizing this type of state are superconducting systems, where the quasiparticles describing excitations above the superconducting ground state have both an electron- and a hole-component. However, as explained in the review of [3], the realization of Majorana zero modes requires these excitations to be effectively spinless, which is not the case for the most common type of superconductors, s-wave superconductors. Consequently Majorana zero modes were for years thought only to exist in few exotic states of matter which include

the rare p-wave superconductors [4] as well as certain states of the fractional quantum Hall effect [5]. While interesting theoretically, these systems are notoriously difficult to handle experimentally and consequently there has been great theoretical interest in finding more experimentally engineerable systems with Majorana zero modes.

A big breakthrough came in 2006, where Kane and Fu [6] showed that Majorana zero modes may also be realized in systems with conventional s-wave superconductors when coupled to a topological insulator with strong spin-orbit coupling. The essential discovery of Fu and Kane was that combining the strong spin-orbit coupling with a magnetic field and induced superconductivity allows an effectively spinless regime to be reached in the topological insulator. The pioneering proposal of Kane and Fu accelerated theoretical discoveries of systems hosting Majorana zero modes. Most notably the authors of [7] and [8] showed in 2010 that Majorana zero modes may also be realized in systems composed of one-dimensional semiconductor nanowires with strong spin-orbit interaction and induced superconductivity. With this discovery, the ground was paved for experimentally realizing Majorana zero modes.

The first reported signature of Majorana zero modes came in 2012, where a research group in Delft [9] published possible experimental evidence for the existence of Majorana zero modes in InSb nanowires deposited onto an s-wave superconductor. The schematics of their setup as well as their most important findings is shown in Fig. 1 (**a**). The experimental signature was in this case the emergence of a zero-bias conductance peak which showed up at a critical magnetic field [8]. These findings were later backed by experiments performed in other laboratories [10, 11]. A further breakthrough came from the materials department at the University of Copenhagen [12, 13], who discovered a way to epitaxially grow the superconductor onto the semiconductor nanowires as shown in Fig. 1 (**b**). This discovery has subsequently led to significant improvements in the observed experimental signatures of Majorana zero modes. While early experimental findings such as [9] are compelling, the non-Abelian nature of the observed Majorana zero modes still remains to be demonstrated, and as of today the hunt for decisive experimental evidence of the elusive quasiparticle continues.

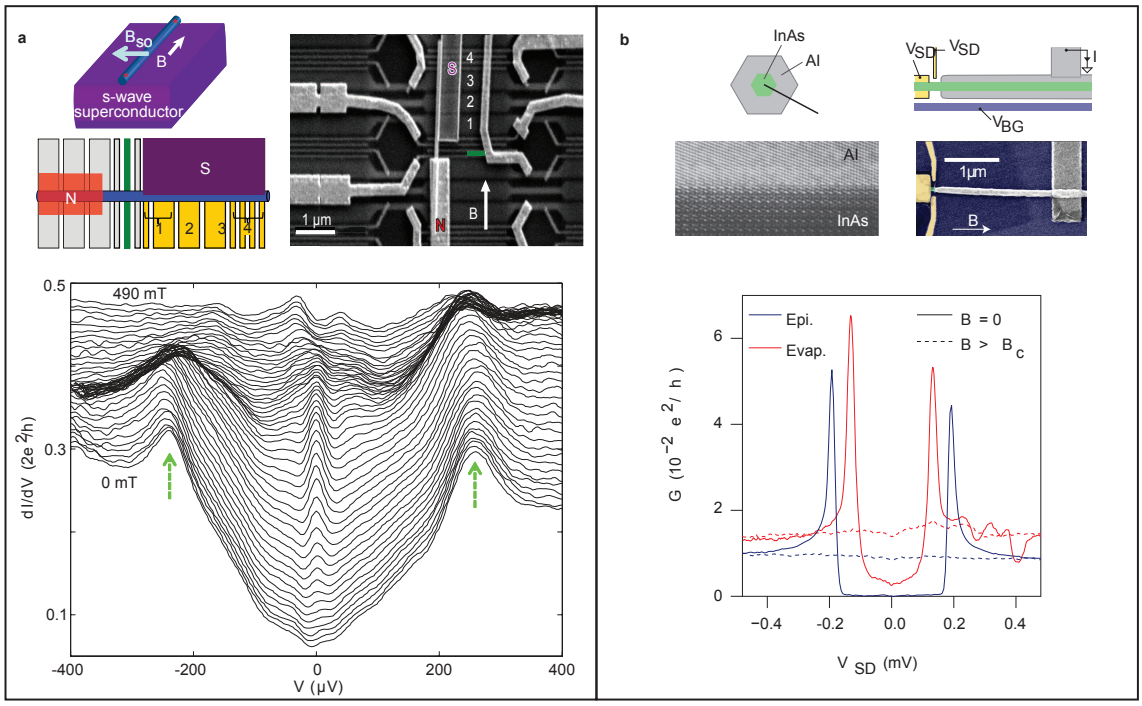

*Figure 1: Overview of some of the significant experimental breakthroughs in realizing Majorana zero modes. (**a**) First reported signature of Majorana zero modes by Mourik et. al. [9]. Top figure shows the schematics of their setup consisting of an InSb nanowire deposited onto an s-wave superconductor, which is then connected to various electrodes. Bottom figure shows the reported signature of Majorana zero modes, which is a zero-bias conductance peak inside the superconducting gap of the nanowire. (**b**) Discovery by Krogstrup et. al. of technique for epitaxially covering nanowires with a thin superconducting layer of Al [12, 13]. Top figure shows the schematics of a device with an epitaxially coated nanowire along with a TEM-inset of the epitaxial interface between the InAs nanowire and Al superconductor. Bottom figure shows the measurement of the superconducting gap in the device, which shows significant improvements compared to previous methods of depositing the superconductor.*

0.2 Example of a Majorana Device

As the search for conclusive evidence of Majorana zero modes continues, so does the complexity and engineerability of the experimental designs. As a motivation for the work of this thesis we will here consider an example of one of the current types of devices used for realizing Majorana zero modes. Throughout this thesis we will collectively refer to such devices as *Majorana devices*.

Fig. 2 shows a schematic example of a state of the art Majorana device, which has shown promising signatures of Majorana zero modes [14].

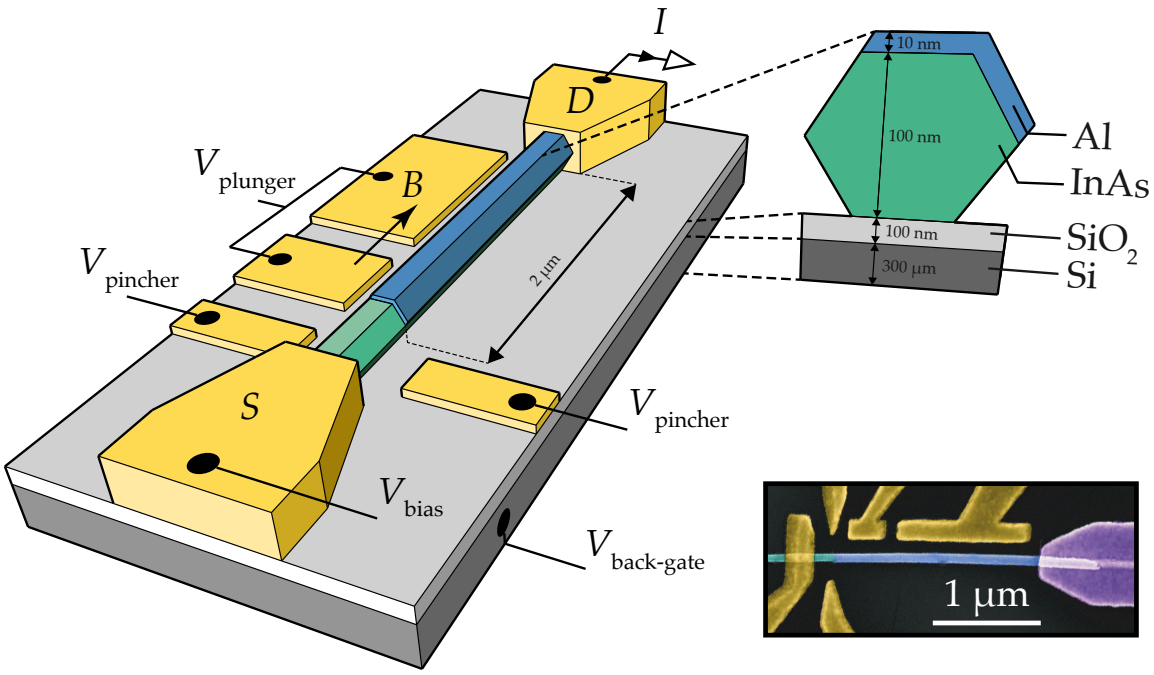

Figure 2: Example of a state of the art setup for detecting Majorana zero modes, which was used for the measurements presented in [14]. Here an InAs nanowire coated by an epitaxial layer of superconducting Al has been placed on a dielectric layer, which is connected to various electrodes. Bottom right image shows a TEM image of the device. This figure is used with permission from Saulius Vaitiekėnas, Center for Quantum Devices, University of Copenhagen.

The Majorana device in Fig. 2 consists of an InAs nanowire partially coated by an epitaxial layer of superconducting Al. This wire has been placed on a dielectric layer of SiO_2, which is connected to layer of doped Si that acts as a gate. A gate is essentially an electrode, which may be used to tune the electrostatic environment of the device. In the setup shown, the doped Si layer is denoted as the back gate. Additional gate electrodes include the pincher gates as well as the plunger gates. All the gate voltages are measured with respect to the grounded drain contact indicated by D, which is in direct contact with the superconducting layer of Al[1]. Finally the device includes a source electrode, indicated by S, which is connected to the drain electrode through a voltage source with a bias V_{bias}.

Loosely stated, the experimental recipe for creating Majorana zero modes in the setup shown is to tune the device to a regime, where transport through the source and drain contacts is dominated by tunelling of few transverse electronic modes in the wire[14]. This happens by applying negative voltages on the various gate electrodes in the system. Once such a regime has been achieved, a finite magnetic field, B, is applied along the wire, which is necessary for the emergence of Majorana zero modes. By subsequently sweeping B and V_{bias} a 2D map of

[1] A geometry like this, where the superconductor is grounded, is a common choice for Majorana devices, though a different variation is also used, where the superconducting layer effectively forms a floating island [15].

the differential conductance of the device is traced out, which potentially can show signatures of Majorana zero modes.

0.3 Outline

This thesis is concerned with modelling the electrostatic environment in Majorana devices. Based on the presentation of the experimental design of Fig. 2 it should come as no surprise that a detailed theoretical understanding of the electrostatics in such setups is of great interest for current research on topological quantum computation. This is also motivated by the fact that the measured values of certain physical quantities, such as for example effective g factors seem to vary greatly[2] depending on the concrete setup used for realizing Majorana zero modes. A plausible contribution to such variations is that the wave function describing the quasiparticle states may exhibit different degree of semiconductor/superconductor character depending on its weight in the respective regions. Understanding such details would obviously require knowledge of the electrostatic environment of the devices in question.

The scope of this thesis is to set up a model for the electrostatic environment in Majorana devices. This model is then applied to two simplified geometries inspired by the experimental device of Fig. 2. The results obtained from this investigation may then be used as a qualitative guidance of electrostatic effects in real Majorana devices.

The remainder of the thesis is divided into 6 chapters.

1. The first chapter describes basic theory needed for the development of our simulation model. This includes different theoretical tools from band structure theory as well as a brief introduction to band diagrams of semiconductors and metals.

2. The second chapter is devoted to explaining the idea behind the Schrödinger-Poisson method, which is the main theoretical tool that our model relies on. The first part of the chapter lays out the theoretical foundation of the method while the second part focuses on the numerical implementation of the method.

3. The third chapter begins by describing the qualitative idea behind our simulation model and subsequently moves on to discuss various assumptions that allow us to make it quantitative. The chapter is concluded with a presentation of two model geometries, that our simulation model will be applied to.

4. The fourth chapter is concerned with applying our simulation model to the first of the

[2]For example [14] reports effective g-factor values of 4 while [15] reports effective g-factor values of 20-50.

two model geometries presented. We first show how to set up our simulation model for the geometry and subsequently discuss various results.

5. The fifth chapter is concerned with applying our simulation model to the second of the two model geometries presented. Similar to the previous chapter we first show how to set up our simulation model for the geometry and subsequently discuss various results.

6. In the sixth chapter we sum up our conclusions and provide a brief discussion of the various results as well as future possible extensions of our model.

Chapter 1

Theoretical Background

In this chapter we set the theoretical foundation for the work carried out in this thesis. We start with some mathematical tools from band structure theory such as the effective mass approximation and the Schrödinger equation in the envelope function formalism. We then move on to discuss band diagrams and band bending in heterostructures. The experienced reader may want to skip this chapter.

1.1 The Effective Mass Concept

For many semiconductors[1] the conduction band energies, $E_c(\mathbf{k})$, may be locally approximated by an isotropic, parabolic dispersion around the conduction band minimum, E_c,

$$E_c(\mathbf{k}) = E_c + \frac{\hbar^2 \mathbf{k}^2}{2m^*} \tag{1.1}$$

When we compare the parabolic dispersion above to that of free electrons with mass m, we see that it has modified curvature which is determined by the quantity m^* as shown in Fig. 1.1 (**a**). m^* may thus be interpreted as an effective mass that the electrons in the conduction band acquire when subject to the periodic potential of the semiconductor crystal.

[1] See for example Chapter 5 of [16]. Examples of semiconductors with a conduction band dispersion described by (1.1) are InAs and Insb, which are the most promising semiconductors for engineering Majorana devices. The simulations presented later in this thesis will be based on semiconductor-metal heterostructures with InAs as the semiconductor.

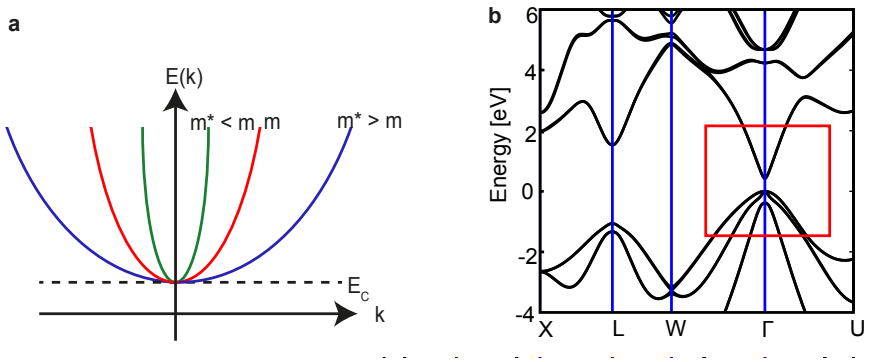

*Figure 1.1: (**a**) Illustration of the conduction band profile for a semiconductor with larger (blue) and smaller (green) effective mass than the free electron mass, m. (**b**) Section of the band structure for InAs obtained from DFT calculations. The approximate parabolic behaviour of the conduction band (shown inside the red box) is evident. InAs will be the most important semiconductor for the simulations in this thesis. Figure adopted from [17].*

Table 1.2 shows the value of the effective mass for some common semiconductors, which are relevant for Majorana devices. For the work described in this thesis, the effective mass will be important for describing the behaviour of electrons in the conduction band of semiconductor-metal heterostructures.

Semiconductor	Effective Mass [m]
GaAs	0.063
GaSb	0.041
InAs	0.023
InSb	0.014

Table 1.1: Values of the effective mass for selected semiconductors. Adopted from [18].

1.2 The Schrödinger Equation in the Envelope Approximation

Using the concept of effective mass, we can reformulate the standard Schrödinger equation in an alternative way that is particularly useful for the problems that will be worked on in this thesis.

To do so we consider a perfect, infinite semiconductor crystal with a conduction band that may be described by the parabolic dispersion in (1.1). We now wish to describe what happens to the conduction band electrons, when they are perturbed by an external potential $V(\mathbf{r})$. Provided that $V(\mathbf{r})$ varies slowly on the scale of the crystal lattice one can show that the electrons in the conduction band may be described by a Schrödinger equation on the form

$$\left(-\frac{\hbar^2}{2m^*}\boldsymbol{\nabla}^2 + E_c + V(\mathbf{r})\right)\psi(\mathbf{r}) = E\psi(\mathbf{r}). \tag{1.2}$$

From this equation we see that the conduction band electrons respond to the external potential as if they they were electrons with an effective mass m^* moving inside $V(\mathbf{r})$.
The derivation of (1.2) is based on the formalism of envelope functions. In this approximation the full wave functions, $\Psi_n(\mathbf{r})$, of the system are the products of a fast-oscillating Bloch function $u_{n\mathbf{0}}(\mathbf{r})$ and an envelope function, $\psi_n(\mathbf{r})$, which varies slowly on the scale of the crystal lattice

$$\Psi_n(\mathbf{r}) = u_{n\mathbf{0}}(\mathbf{r}) \cdot \psi_n(\mathbf{r}). \tag{1.3}$$

When calculating macroscopic properties of the system such as for example the electron density or electrostatic potential, the detailed microscopic behaviour of the wave function is irrelevant and the envelope functions of (1.2) may be used as the full wave functions of the system. We will here not go further into the mathematical details of the envelope function formalism. For a pedagogical introduction to the subject the reader is referred to Chapter 4 of [19] while for the original papers on the problem, [20] and [21] should be consulted.

1.3 The Schrödinger Equation for Heterostructures

The Schrödinger equation (1.2) assumed a single, bulk crystalline semiconductor. For our purposes we seek a more general form, which can describe the conduction band electrons in heterostructures, where the material is composed of bulk regions of different semiconductors or metals[2]. The proper generalization of (1.2) to this case is [22]

$$-\frac{\hbar^2}{2}\boldsymbol{\nabla} \cdot \left(\frac{1}{m^*(\mathbf{r})}\boldsymbol{\nabla}\psi(\mathbf{r})\right) + \left(E_c(\mathbf{r}) + V(\mathbf{r})\right)\psi(\mathbf{r}) = E\psi(\mathbf{r}). \tag{1.4}$$

This is one of the central equations for the models developed in this thesis and will be used extensively throughout the remaining chapters.
As it stands, there are two important differences between (1.2) and (1.4). First of all we see that the band offset $E_c(\mathbf{r})$ and effective mass $m^*(\mathbf{r})$ are now spatially dependent and take different values in the semiconductor and metal regions. Secondly the form of the kinetic energy operator is slightly different from what one might have expected, since the effective mass appears inside the outer gradient operator. The reason that the kinetic energy is written in this form is to ensure hermiticity of the full Hamiltonian. Details of the symmetrization of the kinetic operator and alternative symmetrized forms may be found in for example [23] and [22].

[2]For metals the effective mass description also holds. In this case the effective mass is simply the usual electron mass.

1.4 Band Bending

In (1.2) there are two potential terms. The first term stems from the spatial dependence of the conduction band edge $E_c(\mathbf{r})$, which is a consequence of the mismatch in band edges between the different materials in our system. The second term is the external potential $V(\mathbf{r})$, which varies slowly on the scale of the crystal lattice. In litterature one often sets

$$E_c(\mathbf{r}) \equiv E_c + V(\mathbf{r}). \tag{1.5}$$

This serves to underline the fact that $V(\mathbf{r})$ may simply be viewed as a local variation in the conduction band edge. We will not adopt this notation in thesis, but it is is important to keep the picture in mind that $V(\mathbf{r})$ indeed has the effect of changing the band edge locally. This is for example the principle behind band bending, where an electrostatical potential causes local bending of the band edge. In this case the slowly varying potential of (1.4) is given by $-e\phi(\mathbf{r})$, where $\phi(\mathbf{r})$ denotes the electrostatic potential in the system. This electrostatic potential could arise for example due to an external electrode or from the mutual interaction between the conduction band electrons themselves. Taking the latter into account is essentially the idea of the Schrödinger-Poisson method, which will be the main theoretical method for the work presented in the next chapters.

1.5 Band Diagrams

Fig. 1.2 (**a**) shows the band diagram for a semiconductor. In such a diagram we plot the energy of the valence and conduction band edge as a function of some spatial dimension, say z, in the crystal. These energies are measured with respect to the vacuum energy, which is indicated by the top line on the diagram. The Fermi level of the semiconductor is indicated by the dashed line, which for an intrinsic semiconductor lies in the middle of the band gap. If the semiconductor is n- or p-doped the position of this line will be closer to the conduction or valence band edge, respectively.

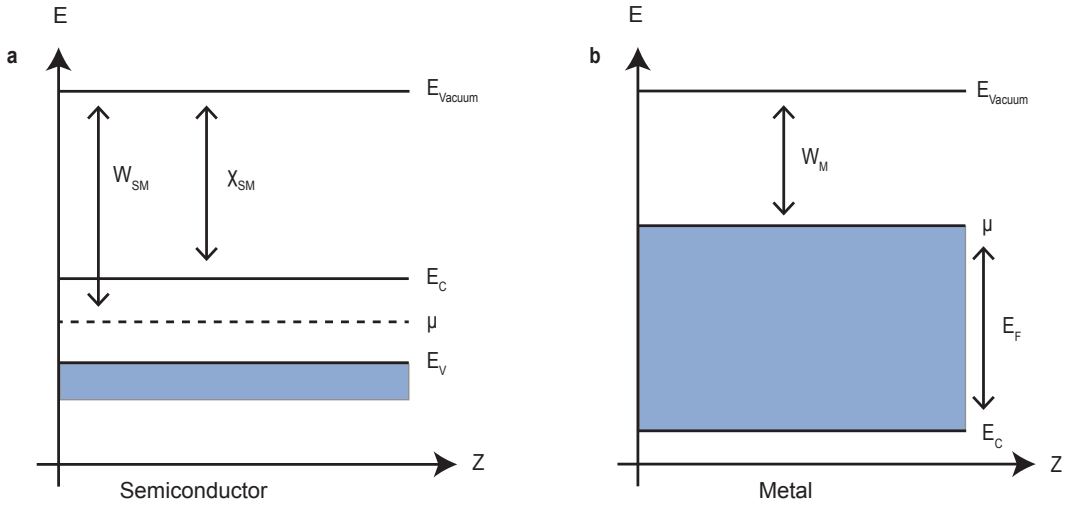

*Figure 1.2: (**a**) Band diagram of a semiconductor. (**b**) Band diagram of a metal.*

From the diagram we can read off two important material parameters of the semiconductor. The work function, W_{SM}, is the minimum work needed to excite an electron from the Fermi level of the semiconductor to vacuum. Since the position of the Fermi level depends on the doping level, so will the value of the work function.
The electron affinity, χ_{SM}, is the minimum work needed to excite an electron from the conduction band edge to vacuum. Ideally this value is unchanged by doping and is thus closer to being a material constant than the work function of the semiconductor. The electron affinity will be an important parameter for the model of semiconductor-metal heterostructures developed later in this thesis. Table 1.2 shows its value for some common semiconductors, which are relevant for Majorana devices.

Semiconductor	Electron Affinity [eV]
GaAs	4.07
GaSb	4.06
InSb	4.59
InAs	4.9

Table 1.2: Values of the electron affinity for some common semiconductors. Adopted from [18].

Fig. 1.2 (**b**) shows the band diagram for a metal with relevant parameters indicated. In this case the highest energy band is filled with states from the band edge up to its Fermi level. The distance between the vacuum energy and Fermi level of the metal is called the work function, W_M, and is the minimum work needed to excite and electron from the Fermi level to vacuum. The distance between the band edge and the Fermi level defines the Fermi energy of the metal.

Table 1.3 shows values of the work function and Fermi energy for some common metals. For metals both the Fermi energy and work function will be required parameters for modelling semiconductor-metal heterostructures later in this thesis.

Metal	Work Function [eV]	Fermi Energy [eV]
Al	4.08	11.7
Cu	4.7	7.00
Au	5.1	5.53
Fe	4.5	11.1
Pb	4.14	9.47
Nb	4.3	9.47
Mg	3.68	7.08

Table 1.3: Values of the work function and Fermi energy for some common metals. Adopted from [24].

In the above we considered the case of bulk systems. In reality band bending due to charge transfer at the surface of a material causes the surface value of the band edge to be different compared to inside the bulk region of the system. Since the work function and electron affinity of a material are measured from electrons emitted from the surface [25], these are generally surface-dependent parameters, which may vary depending on the physics and chemistry of the surface. For the theoretical model that we will develop later, this is problematic, since the work function and electron affinities are vital input parameters. The values given in Table 1.2 and 1.3 should therefore merely be seen as guiding values and not exact quantitative values for our model.

1.6 Semiconductor-Metal Junctions

Since the physical systems that will be considered in this thesis are essentially semiconductor-metal heterostructures, it is instructive to briefly summarize the classical theory of semiconductor-metal junctions. Later we will discuss how the model that we set up compares to the conventional theory.

When a metal is deposited onto a semiconductor two types of contacts may be formed: Ohmic contacts and Schottky contacts.

Ohmic contacts are characterized by zero contact resistance and happen if the carriers are free to flow in and out of the semiconductor. This is in contrast to Schottky contacts, where a barrier is formed at the semiconductor-metal interface. As a rule of thumb [26], a metal and n-type semiconductor will form an Ohmic contact if the work function of the metal is smaller than the electron affinity of the semiconductor, while a Schottky contact is formed if the opposite is true. For p-type semiconductors an Ohmic contact will occur if the work

function of the metal is larger than the sum of the electron affinity and the band gap of the semiconductor, while a Schottky barrier is formed in the opposite case.
It is instructive to summarize the main ideas behind the conventional theory of Schottky barrier formation[3]. To do so we consider a simple model for a Schottky contact, where a metal with work function W_M is deposited onto an n-doped semiconductor with electron affinity $\chi_{SM} < W_M$. The situation is shown in the band diagram of Fig. 1.3 (**a**).

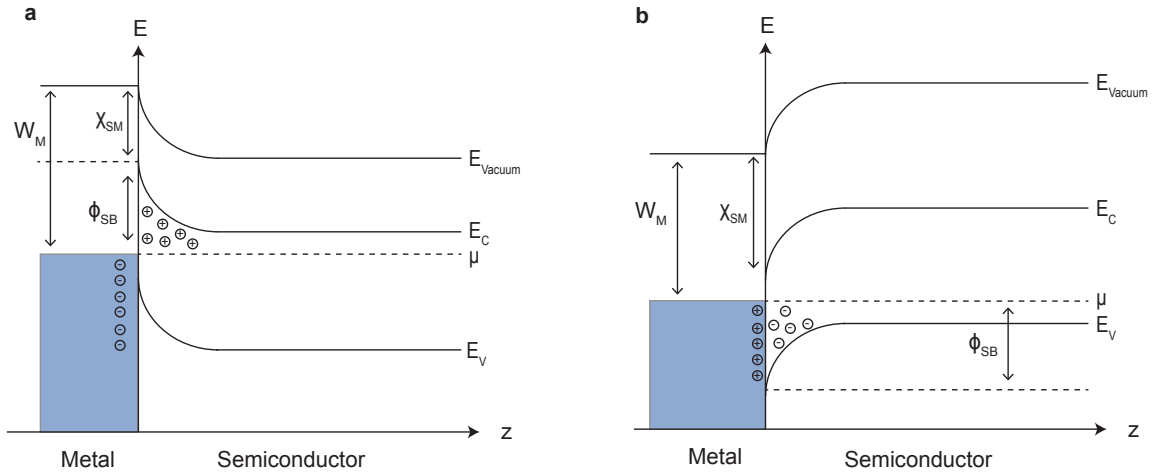

*Figure 1.3: Illustration of the Schottky barrier concept. (**a**) Schottky barrier for an n-type semiconductor. In this case the conduction band and valence band bend upwards thereby creating a barrier for electrons. (**b**) Schottky barrier for a p-type semiconductor. In this case the conduction and valence band bend downwards thereby creating a barrier for hole carriers.*

To understand Fig. 1.3 (**a**) we note that when the metal and semiconductor are brought together their Fermi levels will align due to thermodynamic equilibrium. Far from the interface, in the bulk of the semiconductor, the Fermi level must be close to the semiconductor band edge due to the n-doping, while at the interface it must match the work function set by the metal contact. The way this is achieved is by band bending in the semiconductor, in which the value of the band edge bends due to an electrostatic potential at the interface. As shown in Fig. 1.3 (**a**) the effect of the band bending is to create a barrier of height ϕ_{SB} at the inteface, which is termed a Schottky barrier. Physically the band bending may be understood as a result of donor ionization in the semiconductor, which creates a positive depletion region in a small region around the semiconductor-metal interface.
For an p-type semiconductor the same arguments as the above may be applied, though in this case the depletion region will be negative, since it arises from ionization of acceptors close to the valence band of the semiconductor. The result in this case will therefore be that the

[3]This summary is largely based on Chapter 5 of [19].

bands will bend downwards as shown in Fig. 1.3 (**b**), which in this case creates a barrier for hole carriers.

Above we argued for band bending in semiconductor-metal junctions based on donor- and acceptor ionization close to the metal interface, without however going into the physical details of this phenomenon. It turns out that understanding this effect and understanding Schottky barrier formation in general is more complicated and is closely tied to surface and interface physics, in which one must include effects of induced interfacial states at the semiconductor-metal interface. In fact, it turns out, that due to these complicated interfacial effects even the simple assumption that the total band bending is determined by the difference in work function and electron affinity of the semiconductor and metal is also not generally true. We will not go into the details of understanding Schottky barrier formation in this thesis. The interested reader is refered to [27, 28, 29].

Chapter 2

The Schrödinger-Poisson Method

With the most basic theory in place, we are now ready to focus on our main theoretical tool, which is the Schrödinger-Poisson method. We will start by laying out the theoretical foundations of the Schrödinger-Poisson method and subsequently move on to discuss its numerical aspects.

2.1 The Schrödinger-Poisson Problem

The Schrödinger-Poisson method is a mean-field method used to describe a system of interacting electrons. The key assumption is that the behaviour of the electrons may be described using the Hartree approximation[1]. To understand this consider the many-body Schrödinger equation for a system of electrons with Coulomb interaction

$$\left(\underbrace{\sum_i H_0(\mathbf{r}_i)}_{\text{Single Particle Terms}} + \underbrace{\frac{1}{2}\sum_{i\neq j}\sum_j \frac{e^2}{4\pi\epsilon}\frac{1}{|\mathbf{r}_i-\mathbf{r}_j|}}_{\text{Interaction Terms}} \right) \Psi(\mathbf{r}_1,\mathbf{r}_2,....) = E\Psi(\mathbf{r}_1,\mathbf{r}_2,....). \tag{2.1}$$

Where $\Psi(\mathbf{r}_1,\mathbf{r}_2,....)$ denotes the full many-body wave function of the system. The idea of the Hartree approximation is to assume that Ψ is a product of single-particle states $\Psi = \psi_1(\mathbf{r}_1)\psi_2(\mathbf{r}_2)\psi_3(\mathbf{r}_3)...$. Using this assumption it may be shown that (2.1) can be reduced to a set of single-particle equations on the form

$$\left(H_0 \quad - e\int d\mathbf{r}' \, \frac{1}{4\pi\epsilon}\frac{\rho(\mathbf{r})}{|\mathbf{r}-\mathbf{r}'|} \right) \psi_i(\mathbf{r}) = E\psi_i(\mathbf{r}). \tag{2.2}$$

[1]For a derivation of the Hartree approximation see the first chapters of [30].

With the single-particle electron charge density[2] given by

$$\rho(\mathbf{r}) = -e\sum_j |\psi_j(\mathbf{r})|^2, \tag{2.3}$$

which runs over all occupied single-particle states in our system.
Those familiar with the classical theory of electrostatics will notice that the second term in (2.2) is nothing but the interaction of each electron with the electrostatic potential $\phi(\mathbf{r})$ generated by the electrons in our system. Consequently (2.2) may be written simply as

$$\Big(H_0 - e\phi(\mathbf{r})\Big)\psi_i(\mathbf{r}) = E\psi_i(\mathbf{r}). \tag{2.4}$$

With the electrostatic potential described by the solution of Poisson's equation of classical electrostatics

$$\boldsymbol{\nabla}\cdot(\epsilon_r\boldsymbol{\nabla}\phi) = \frac{-\rho}{\epsilon_0}. \tag{2.5}$$

The combined equations (2.3), (2.4) and (2.5) are the fundamental equations of the Schrödinger-Poisson method. Together (2.3) and (2.4) define a functional, which yields a charge density $\rho[\phi]$ for a given electrostatic potential, while Poisson's equation (2.5) defines a functional yielding an electrostatic potential $\phi[\rho]$ for a given charge density. To solve the coupled system one must thus look for a self-consistent solution for which

$$\rho[\phi[\rho]] = \rho. \tag{2.6}$$

The standard way to do this is through an iterative process, which will be described in detail when we address the numerical details of the Schrödinger-Poisson method. Before doing so, let us however quickly recap some basic facts about solving Poisson's equation for a general system.

2.2 Solving Poisson's Equation for the Electrostatic Potential

Once we know the electron density in our system we can calculate the electrostatic potential using Poisson's equation (2.5). To proceed with such a calculation we will need knowledge of the specific geometry and boundary conditions of our system. Nonetheless some general points can be made if we consider a generic system as shown in Fig. 2.1 consisting of a combination of different semiconductors, metal electrodes and insulating dielectrics.

[2]We write charge density to separate it from the particle density. From now on we will simply mean charge density when we refer to the electron density in our system.

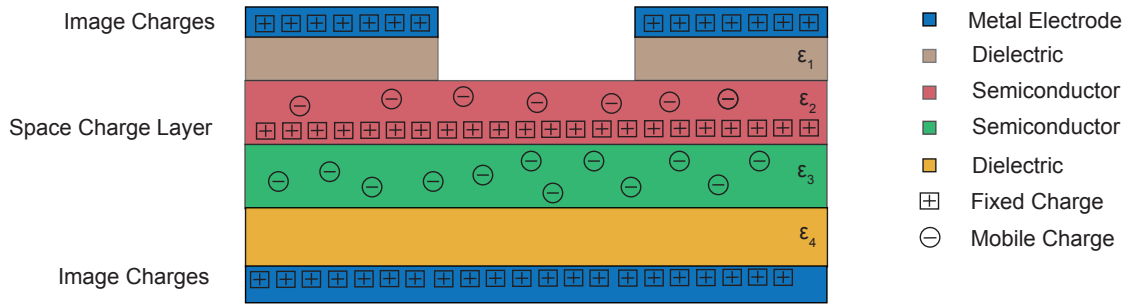

Figure 2.1: Sketch of a generic setup for solving Poisson's equation with different types of charges present.

We first note that since Poisson's equation must be solved in all space the dielectric constant, ϵ_r, in (2.5) will be spatially dependent, taking different values in the different material regions in our system. Table 2.1 lists some values of ϵ_r for common semiconductors and insulators, some of which will be used for the simulations presented in the next chapters.

Material	Dielectric constant, ϵ_r
Vacuum	1.0
Si	11.9
SiO_2	4.7
Ge	4.0
GaN	4.1
GaAs	5.1
GaSb	4.5
InAs	4.14
InSb	4.3

Table 2.1: Values of the relative dielectric constant for various semiconductors and insulators. Adopted from [18].

We also note that the spatial dependence of ϵ_r has consequences for the electrostatic boundary conditions across the various heterointerfaces in our system. If we denote the dielectric constants of two materials by ϵ_1 and ϵ_2, the electrostatic boundary conditions at their interface are generally given by (see for example Chapter 4 of [31])

$$\phi_2 - \phi_1 = 0 \tag{2.7}$$

$$\mathbf{E}_2^{\parallel} - \mathbf{E}_1^{\parallel} = 0 \tag{2.8}$$

$$\epsilon_2 E_2^{\perp} - \epsilon_1 E_1^{\perp} = \frac{\sigma_f}{\epsilon_0} \tag{2.9}$$

From this we see that the electrostatic potential and parallel components of the electric field are continuous while the perpendicular component of the electric field is discontinuous with the discontinuity determined by the mismatch of ϵ_1 and ϵ_2 as well as the free surface charge, σ_f, on the interface.

Let us now focus on the charges in our system. In the generic problem these can originate from multiple sources as shown in Fig. 2.1. First of all there will be mobile charges in the semiconducting regions, which must be treated using the Schrödinger equation for heterostructures (1.4).
Secondly there may be space charge layers due to ionized dopants or due to the filling of surface and interfacial states at the various heterointerfaces. We mention the latter two types of charges for completeness, though they will not be relevant for the model that we will develop in the next chapter.
Finally there may be image charges due to the metal electrodes as shown in Fig. 2.1. Such charges arise from the fact that the metal electrodes are conductors for which the interior electric field must vanish. The metal electrodes achieve this by inducing a density of image charges on their surfaces, which screens the electric field from the charges in the semiconductor regions. Since the electric field is zero inside the metallic components of Fig. 2.1, this implies that the electrostatic potential must be constant in these regions. When solving Poisson's equation for the generic heterostructure in Fig. 2.1, one should therefore not solve Poisson's equation in the metallic regions. Instead the metal electrodes act as boundary conditions requiring that the electrostatic potential should take constant values on their surfaces S_i

$$\phi(\mathbf{r})|_{S_i} = \phi_i. \tag{2.10}$$

With the values of ϕ_i chosen to match the voltage differences between the different electrodes in the system.

2.3 The Numerical Details

So far nothing has been said about how to obtain the solutions to the Schrödinger equation (2.4) and Poisson's equation (2.5). In general these will not be solvable analytically and one must resort to numerical methods. For the calculations presented in this thesis the finite difference method has been used [32]. The basic idea of this method is to approximate differential equations by difference equations, which may then be solved by linear algebra methods. This is illustrated in the subsections below, where the numerical details of solving the Schrödinger and Poisson equation are outlined. Furthermore we address the numerical aspects of obtaining the self-consistent solution to the Schrödinger-Poisson problem.

2.3.1 Solving the Schrödinger Equation Using the Finite Difference Method

Inspired by (1.4) let us consider a 2D Schrödinger equation on the form[3],

$$-\frac{\hbar^2}{2}\left(\frac{\partial}{\partial x}\left(\frac{1}{m^*(x,y)}\frac{\partial\psi}{\partial x}\right)+\frac{\partial}{\partial y}\left(\frac{1}{m^*(x,y)}\frac{\partial\psi}{\partial y}\right)\right)+V(x,y)\psi=E\psi, \tag{2.11}$$

where $V(x,y)$ represents the two potential terms in (1.4).
Suppose we wish to solve this equation on a domain Ω with boundary $\partial\Omega$ as shown in Fig. 2.2 (**a**). To obtain a unique solution (2.11) must be supplemented by a complete set of boundary conditions. Since the numerical implementation of different types of boundary conditions is rather technical, we will skip the details here. For a treatment of the problem with boundary conditions the reader is referred [32].

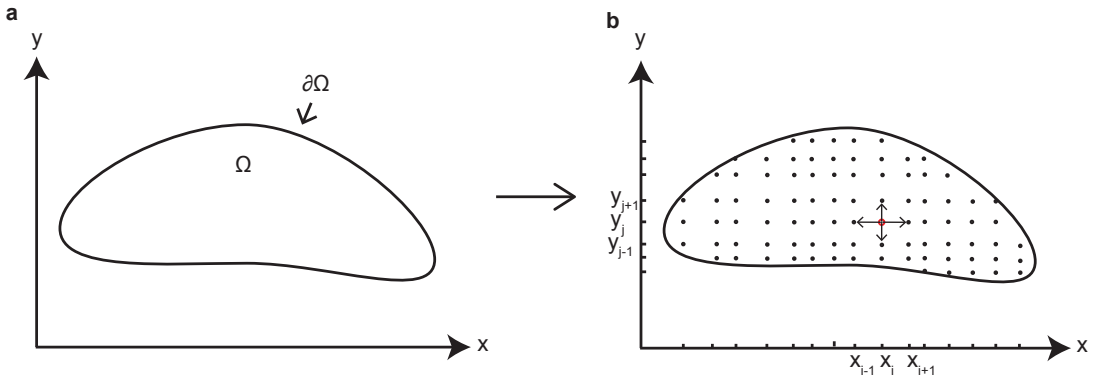

*Figure 2.2: Illustration of the finite difference method. (**a**) Continuous domain on which we want solve the Schrödinger equation* (2.11)*. (**b**) Discretized domain with an illustration of the idea behind the finite difference formula used in* (2.13)*.*

The first step of the finite difference method is to reduce the continuous domain Ω to a finite number of points (x_i, y_j) as shown in Fig. 2.2. Doing so (2.11) is reduced to a set of equations for each grid point,

$$-\frac{\hbar^2}{2}\left(\left[\frac{\partial}{\partial x}\left(\frac{1}{m^*}\frac{\partial\psi}{\partial x}\right)\right]_{i,j}+\left[\frac{\partial}{\partial y}\left(\frac{1}{m^*}\frac{\partial\psi}{\partial y}\right)\right]_{i,j}\right)+\ V_{i,j}\psi_{i,j}=E\psi_{i,j}. \tag{2.12}$$

In this notation $\psi_{i,j}\equiv\psi(x_i,y_j)$ and similarly for $V_{i,j}$ and the derivative terms.
The problem is now how to calculate the derivative terms appearing in (2.12). The central idea

[3]The form and dimensionality of the Schrödinger equation can of course be very different depending on the physical system of interest. The one chosen is appropriate for the 2D heterostructure systems, that will be studied in this thesis. For 1D planar heterostructures, which will also be considered, the derivations and conclusions in this section are essentially the same.

of the finite difference method is to approximate such terms with finite difference formulas. To clarify this consider the derivative term with respect to x appearing in (2.12). The finite difference approximation to this term can be taken as[4],

$$\left[\frac{\partial}{\partial x}\left(\frac{1}{m^*}\frac{\partial \psi}{\partial x}\right)\right]_{i,j} \approx \frac{1}{(x_{i+1}-x_{i-1})/2}\left(\frac{1}{m^*_{i+1/2,j}}\frac{\psi_{i+1,j}-\psi_{i,j}}{x_{i+1}-x_i} - \frac{1}{m^*_{i-1/2,j}}\frac{\psi_{i,j}-\psi_{i-1,j}}{x_i-x_{i-1}}\right). \tag{2.13}$$

Here the notation $m^*_{i\pm 1/2,j}$ means the average value of the effective mass between the two grid points (x_i, y_j) and $(x_{i\pm 1}, y_j)$.
A corresponding formula for the derivative term with respect to y appearing in (2.12) can be obtained in a similar way. Doing so (2.12) may therefore be rewritten as,

$$\begin{aligned} &\frac{-\hbar^2}{x_{i+1}-x_{i-1}}\left(\frac{1}{m^*_{i+1/2,j}}\frac{\psi_{i+1,j}-\psi_{i,j}}{x_{i+1}-x_i} - \frac{1}{m^*_{i-1/2,j}}\frac{\psi_{i,j}-\psi_{i-1,j}}{x_i-x_{i-1}}\right) \\ &- \frac{\hbar^2}{y_{j+1}-y_{j-1}}\left(\frac{1}{m^*_{i,j+1/2}}\frac{\psi_{i,j+1}-\psi_{i,j}}{y_{j+1}-y_j} - \frac{1}{m^*_{i,j-1/2}}\frac{\psi_{i,j}-\psi_{i,j-1}}{y_j-y_{j-1}}\right) + V_{i,j}\psi_{i,j} = E\psi_{i,j}. \end{aligned} \tag{2.14}$$

This is now the central equation for solving the Schrodinger equation. It is a difference equation in the sense that it connects the value of the wave function at the grid point (x_i, y_j) to its values at the neighbouring grid points $(x_{i\pm 1}, y_j)$ and $(x_i, y_{j\pm 1})$ as shown in Fig. 2.2.
The simplest way to solve (2.14) is to invoke standard linear algebra methods where the wave function is expressed as a column vector

$$\boldsymbol{\psi} = \begin{bmatrix} \psi_1 \\ \psi_2 \\ \vdots \end{bmatrix} \tag{2.15}$$

containing the value of the wave function at each grid point. However, to do so it is clear that the grid must be ordered according to a single index rather than the double index (i,j). This ordering may in principle be chosen in many different ways but for most purposes the simplest way is to use natural ordering, where the points of Fig. 2.2 would be ordered by starting from one corner and then scanned in either vertical or horizontal lines. Once a suitable ordering has been chosen (2.14) may be be put in the form of a eigenvalue equation

$$\hat{H}\boldsymbol{\psi} = E\boldsymbol{\psi}. \tag{2.16}$$

Here the matrix Hamiltonian must include both the potential and kinetic terms in (2.14). It is

[4] In general there may several finite difference formulas that can be used to achieve the same results. We will stick to the one presented here.

clear that the potential term will always enter on the diagonal entries of the Hamiltonian, while the kinetic energy terms will also give rise to non-zero off-diagonal elements since it couples neighbouring grid points. The exact form of $\hat{H}$ will of course depend on the ordering and geometry of the grid. Once this has been established, the wave functions $\boldsymbol{\psi}$ may be computed as the eigenvectors of $\hat{H}$. Since the numerical work of this thesis was done in MATLAB, this was most easily done using the in-built algorithm eigs. This algorithm takes a given matrix and a natural number N as input, and then computes the N smallest eigenvalues of the matrix and the corresponding eigenvectors using sparse matrix methods. It is numerically efficient to compute only the eigenvectors that correspond to occupied electronic states, since only these enter in the expression for the electron density (2.3) used in the Schrödinger-Poisson method.

2.3.2 Solving Poisson's Equation Using the Finite Difference Method

Consider the 2D Poisson equation on the form[5]

$$\frac{\partial}{\partial x}\left(\epsilon_r(x,y)\frac{\partial \phi}{\partial x}\right)+\frac{\partial}{\partial y}\left(\epsilon_r(x,y)\frac{\partial \phi}{\partial y}\right)=\frac{-\rho(x,y)}{\epsilon_0}. \tag{2.17}$$

This equation has similarities with the Schrödinger equation in (2.11) but while the Schrödinger equation is an eigenvalue equation the Poisson equation above contains a source term. This means that many of the numerical procedures described in the previous section carry over to the treatment of (2.17), but there will also be important differences.

Suppose we wish to solve (2.17) on the domain Ω with boundary $\partial\Omega$ shown in Fig. 2.2. We will once again skip the technical details of the boundary condition, but the interested reader is referred [32].

Similar to the method used for the Schrödinger equation we reduce Ω to a finite number of points (x_i, y_i). Doing so then yields a set of equations for each grid point,

$$\left[\frac{\partial}{\partial x}\left(\epsilon_r(x,y)\frac{\partial \phi}{\partial x}\right)\right]_{i,j}+\left[\frac{\partial}{\partial y}\left(\epsilon_r(x,y)\frac{\partial \phi}{\partial y}\right)\right]_{i,j}=\frac{-\rho_{i,j}}{\epsilon_0} \tag{2.18}$$

Where we have adopted a similar notation as in (2.14). Approximating the derivate terms by a finite difference formula then yields,

$$\frac{1}{(x_{i+1}-x_{i-1})/2}\left(\epsilon_{r,i+1/2,j}\frac{\phi_{i+1,j}-\phi_{i,j}}{x_{i+1}-x_i}-\epsilon_{r,i-1/2,j}\frac{\phi_{i,j}-\phi_{i-1,j}}{x_i-x_{i-1}}\right) \tag{2.19}$$

$$+\frac{1}{(y_{j+1}-y_{j-1})/2}\left(\epsilon_{r,i,j+1/2}\frac{\phi_{i,j+1}-\phi_{i,j}}{y_{j+1}-y_j}-\epsilon_{r,i,j-1/2}\frac{\phi_{i,j}-\phi_{i,j-1}}{y_j-y_{j-1}}\right)=\frac{-\rho_{i,j}}{\epsilon_0}. \tag{2.20}$$

[5] Again we restrict ourselves to study the 2-dimensional case, since this is relevant for the 2D heterostructures that will be presented in this thesis. The method is essentially the same for the one-dimensional planar structures that will also be studied.

Where the notation $\epsilon_{r,i+1/2,j}$ means the average value of ϵ_r between the two points (x_i, y_j) and (x_{i+1}, y_j).
The easiest way to solve (2.20) is to put it in matrix form, where the electrostatic potential $\boldsymbol{\phi}$ and density $\boldsymbol{\rho}$ are expressed as vectors of values belonging to each grid point. To do so we must order the grid points according to a single index k, just like we did with the Schrödinger equation. Once a proper ordering has been chosen we can then write (2.20) as

$$\hat{D}\boldsymbol{\phi} = \frac{-\boldsymbol{\rho}}{\epsilon_0}. \tag{2.21}$$

This equation may then be solved for the electrostatic potential by matrix inversion yielding

$$\boldsymbol{\phi} = \hat{D}^{-1}\frac{-\boldsymbol{\rho}}{\epsilon_0}. \tag{2.22}$$

2.3.3 Validity of The Finite Difference Approximation

Due to its time-consuming and technical nature, we will not address the general validity of the finite difference approximations (2.14) and (2.20). For a thorough treatment of this subject the reader is referred to [32].
There is however a simple and intuitive argument for the validity of the finite difference approximation of the Schrödinger equation that we will mention, since it will play a role for the way we set up our numerical model in the next chapters.
To understand the argument let us for simplicity suppose that we want to solve the Schrödinger equation (2.11) on a uniform 1D grid with a constant effective mass m^* and potential V_0. In this case the finite difference approximation (2.14) reads

$$\frac{-\hbar^2}{m^*} \cdot \frac{1}{2\Delta x^2}(\psi_{i+1} + \psi_{i-1} - 2\psi_i) + V_0\psi_i = E\psi_i. \tag{2.23}$$

With $\Delta x \equiv x_i - x_{i-1}$.
For the continuous problem the eigenstates of the uniform Schrödinger equation above are plane waves with the standard parabolic energy dispersion of free particles

$$\psi_k(x) = e^{ikx} \quad , \quad E(k) = V_0 + \frac{\hbar^2 k^2}{2m^*}. \tag{2.24}$$

The corresponding eigenstates of the discrete problem are given by

$$\psi_k(x_i) = e^{ikx_i} \qquad E(k) = V_0 + \frac{\hbar^2}{m^*} \cdot \frac{1}{\Delta x^2}(1 - \cos(k\Delta x)) \tag{2.25}$$

As may easily by verified by insertion into (2.23).
At first sight the two dispersions (2.24) and (2.25) look quite different. But if we assume that our grid is fine such that $k\Delta x << 1$ we find by Taylor expansion $\cos(k\Delta x) \approx 1 - \frac{1}{2}k^2\Delta x^2$

leading to

$$E(k) = V_0 + \frac{\hbar^2}{m^*} \cdot \frac{1}{\Delta x^2}(1 - \cos(k\Delta x)) \approx V_0 + \frac{\hbar^2 k^2}{2m^*}. \tag{2.26}$$

The interpretation of this result is simple. For accurate results we should use a grid distance such that $k\Delta x << 1$ implying that it should be chosen significantly smaller than the wavelength of the states we wish to describe.

2.3.4 Obtaining the Self-Consistent Solution

We previously saw that the solution to the Schrödinger-Poisson problem must be calculated self-consistently due to the mutual dependence of the electron density and electrostatic potential. The standard way to do this is through an iterative process, which in our case may be summarized in the steps below.

1. Using a suitable input potential for the electrostatic potential $\phi_0^{in}(\mathbf{r})$ the Schrödinger equation (2.4) is solved yielding a set of electronic wave functions $\{\psi_0^n(\mathbf{r})\}$.

2. From these wave functions one can then calculate the electron density in the system $\rho_0(\mathbf{r})$ through (2.3), which may be used to solve Poisson's equation for an output electrostatic potential $\phi_0^{out}(\mathbf{r})$.

3. Using a suitable mixture of $\phi_0^{in}(\mathbf{r})$ and $\phi_0^{out}(\mathbf{r})$ a new input potential $\phi_1^{in}(\mathbf{r})$ is calculated. With this new potential one proceeds to solve (2.4) again, yielding a new set of electronic wave functions $\{\psi_1^n(\mathbf{r})\}$.

4. The process is repeated until the error between two successive iterations falls below some predefined accuracy.

The process is shown diagramatically in the flowchart of Fig. 2.3.
The mixture of $\phi_n^{in}(\mathbf{r})$ and $\phi_n^{out}(\mathbf{r})$ for the n'th iteration must of course be chosen such that the problem converges to a solution. For the work in this thesis a simple mixing scheme was used, where the new input potential was calculated according to

$$\phi_{n+1}^{in}(\mathbf{r}) = (1 - \lambda)\phi_n^{in}(\mathbf{r}) + \lambda\phi_n^{out}(\mathbf{r}). \tag{2.27}$$

Here λ is a mixing parameter for which the typical value was chosen to be $\lambda = 0.1$. The initial input potential was simply chosen as $\phi_0^{in} = 0$.
While more advanced mixing schemes exist [33, 34], which typically provide faster convergence, implementing these has not been a focus of the work described in this thesis.

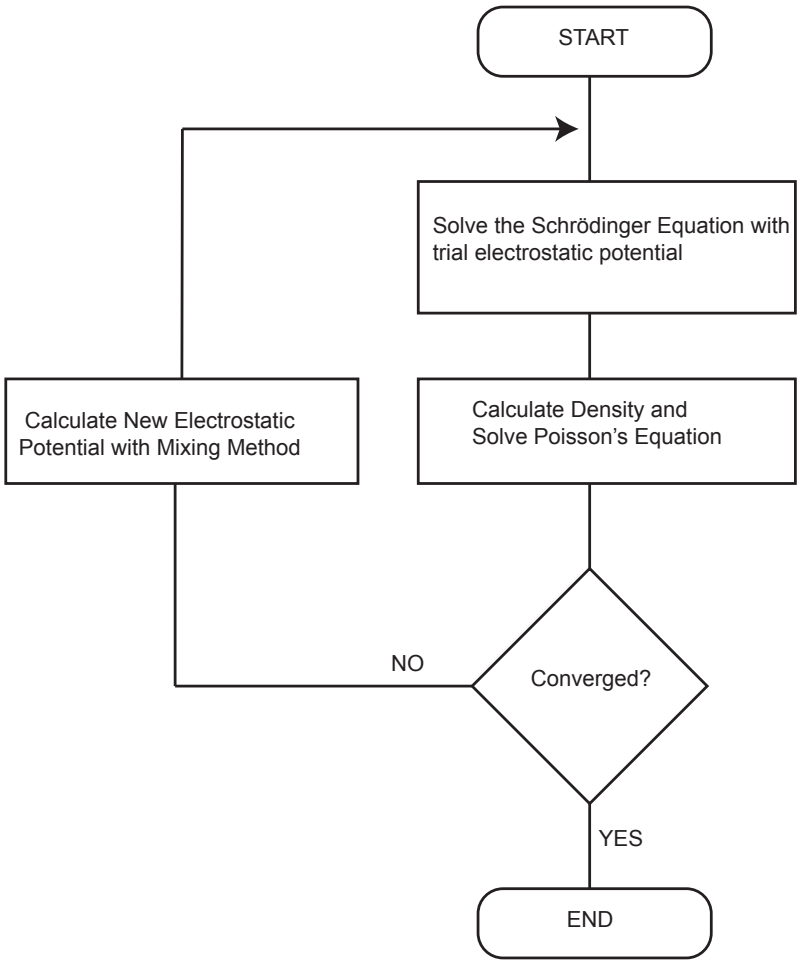

Figure 2.3: Flowchart of our self-consistent Poisson solver.

Chapter 3

The Simulation Model

With the necessary theory in place, we are now ready to introduce our simulation model. The main tool of this model is the Schrödinger-Poisson method that we introduced in Chapter 2 though we will also build on the various theoretical methods presented in Chapter 1.
We will begin this chapter with a qualitative motivation for our model and then discuss various assumptions that allow us to make it quantitative. Finally we will introduce two simple geometries, which are inspired by the Majorana device of Fig. 2 and to which our model will be applied in Chapter 4 and 5.

3.1 The Qualitative Picture

Since the fundamental building blocks of the Majorana device of Fig. 2 is a semiconductor and a metallic superconductor, a natural starting point is to understand the physics of what happens as these are brought together to form a heterostructure. We have already described the conventional theory of band bending and Schottky barrier formation in such structures but, as it turns out, the physics behind our model is different in several aspects, which we now address.
First of all the conventional theory relied on the semiconductors being either n- or p-type such that the ionization of donors or acceptors would create a depletion layer at the semiconductor-metal interface. This is not the case for Majorana devices, where the semiconductor components are intrinsic semiconductors.
Secondly we are interested in semiconductor-metal combinations for which the work function of the metal is smaller than the electron affinity of the semiconductor. This is for example the case for InAs-Al junctions, which is the material combination used in the experimental device of Fig. 2, and which the results of Chapter 4 and 5 will be based on. In this case the metal and semiconductor will form an Ohmic contact with no interfacial barrier. However, there will still be band bending due to the metal donating electrons to the conduction band

of the semiconductor. This is essentially what we wish to describe.
With this in mind let us now turn to the qualitative idea behind our model, which is shown in the band diagrams of Fig. 3.1 (**a**) and (**b**). Fig. 3.1 (**a**) shows the band diagram for a metal with work function W_M and a semiconductor with electron affinity $\chi_{SM} > W_M$ at zero temperature before contact. In this case the metal is filled up to its own Fermi level while the semiconductor has a filled valence band and a Fermi level in the middle of the band gap. We now imagine that the two materials are brought together to form a heterostructure. In this case the electrons of the metal will spill in and hybridize with the empty conduction band states of the semiconductor. Doing so an electrostatic potential builds up in the semiconductor which opposes the flow of charge by band bending. The final result will be as shown in Fig. 3.1 (**b**), where the band edges of the semiconductor bend down towards the metal due to electrostatic interaction.

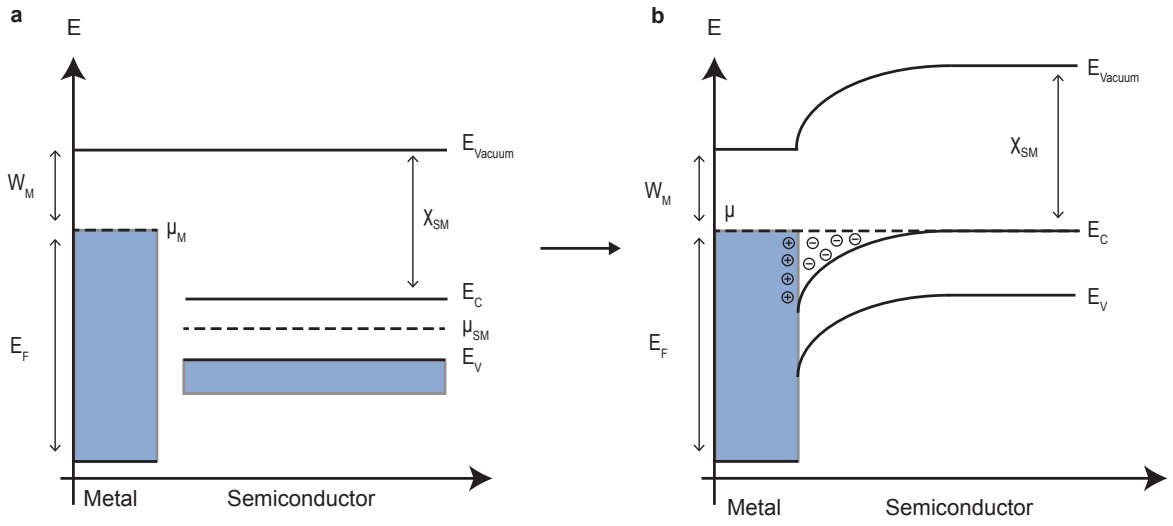

*Figure 3.1: Illustration of the qualitative idea behind our model. (**a**) Band diagram of a metal with work function W_M and semiconductor with electron affinity $\chi_{SM} < W_M$ before contact. (**b**) Band diagram of the hybrid system. In this case electrons have spilled in from the metal and filled some of the empty conduction band states in the semiconductor. This has caused the conduction band edge to bend downwards. The positive charges in the metal are screening charges which are present to keep the electric field constant inside the metal.*

3.2 The Quantitative Model and Simplifying Assumptions

Let us now attempt to make a quantitative model for the above using the theoretical tools of the previous sections. To do so we will need to make different simplifying assumptions and approximations, which we will point out and discuss, as we go along.

The central idea of our model is that the conduction band electrons in the hybrid semiconductor-metal system may be described by the Schrödinger-Poisson model. The fundamental Schrödinger equation for our problem is

$$-\frac{\hbar^2}{2}\boldsymbol{\nabla}\cdot\left(\frac{1}{m^*(\mathbf{r})}\boldsymbol{\nabla}\psi\right)+E_c(\mathbf{r})\psi-e\phi(\mathbf{r})\psi=E\psi. \tag{3.1}$$

Which is the effective-mass Schrödinger equation for heterostructures (1.4) with the slowly varying potential given by the electrostatic potential in our system. Depending on the geometry of the system, (3.1) will be solved either in both the metal and semiconductor region of the system or only in the semiconductor region. We will address this in the next chapters where we apply our model to two specific geometries. Notice also that we have completely neglected effects of the valence band electrons in the semiconductor. Physically this amounts to the assumption that these electrons simply form a filled band with no effects on the properties of the conduction band electrons. Such a description is only correct for small temperatures for which thermal excitations of valence band electrons are negligible. But this is exactly the relevant regime for measurements on Majorana devices, which are performed at temperatures on the milli-Kelvin scale. For these temperatures $k_BT << E_g$ such that thermal excitations on the order of the semiconductor band gap, E_g, are heavily suppressed. For our simulations we will simply assume zero temperature.

Having solved the Schrödinger equation (3.1) for our system the density may be calculated according to (2.3). To do this we must specify the Fermi level in our system. For our model we will assume that the metal sets the Fermi level of the hybrid system. Physically the metal is thus assumed to act as a resevoir of electrons whose physical properties are unchanged by being merged with the semiconductor.

As for Poisson's equation (2.5), this may be solved once we have computed the electron density in our system. For our model Poisson's equation will be solved in the semiconductor region of Fig. 3.1 as well as inside a dielectric region. The exact details of this will depend on the specific geometry we wish to model. In all cases we will assume that the metallic superconductor acts as a perfect conductor such that the boundary condition (2.10) applies. This means that the metal will screen the electric field in the semiconductor by placing image charges at the semiconductor-metal interface as shown in Fig. 3.1 (**b**).

A last assumption of our model is that we completely neglect effects of surface and interfacial states in our system, since including these would generally be complicated and would introduce several unknown parameters in our model. Whether the assumption of neglecting them is physically valid is currently unknown, though for interfacial states at the semiconductor-metal interface a simple ad-hoc argument could be that these would merely contribute to a surface charge density whose effect would be cancelled out by screening charges of the metal. Regardless of whether this argument is valid or not, it still leaves us with the question of the

effect of surface states at other interfaces in our system. In particular this question is relevant for the interfaces between the semiconductor and vacuum regions, where band bending due to surface charges is an experimentally known effect for many semiconductors. Most notably InAs, which our simulations will be based on, is known to exhibit strong band bending at the semiconductor-vacuum interface due to surface states [35, 36].
We will not discuss effects of surface and interfacial states further in this thesis but silently assume that they may be neglected.

3.3 The Two Geometries

We now turn to our two model geometries, which are shown in Fig. 3.2. These are inspired by the Majorana device of Fig. 2 but with some simplications, which we address below.

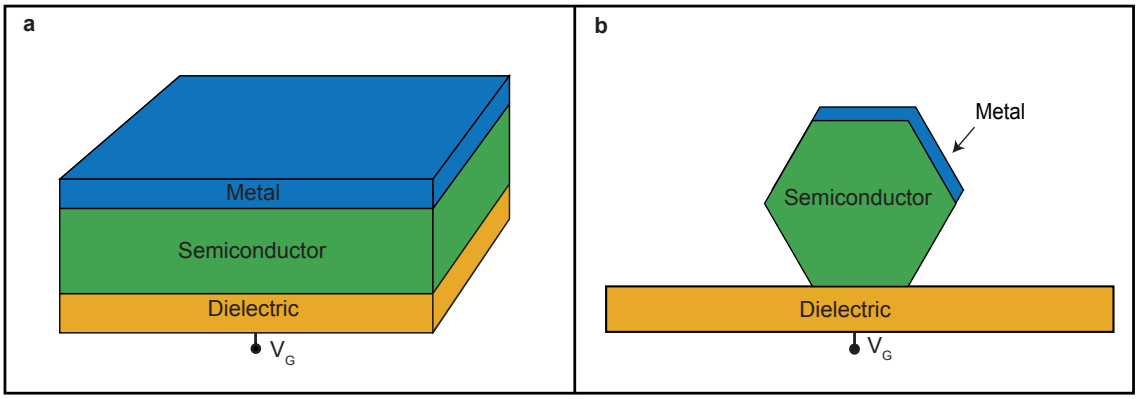

*Figure 3.2: Sketch of our two model geometries. (**a**) Planar geometry consisting of a metal, semiconductor and dielectric layer. The dielectric is connected to a gate electrode from below, which is held at a gate voltage V_G with respect to the grounded metallic layer. (**b**) 2D geometry consisting of the cross section of a hexagonal nanowire, which is coated by a metallic superconductor on two facets. The nanowire sits on a dielectric layer, which is connected to a gate electrode from below. This is held at a voltage V_G with respect to the grounded metallic superconductor.*

The first model geometry, shown in Fig. 3.2 (**a**), is a planar structure of metal, semiconductor and dielectric, which is connected to a gate electrode from below. We will assume this gate to be held at a voltage V_G with respect to the grounded metallic layer on top. It thus behaves essentially like the back gate of the Majorana device in Fig. 2. When setting up the Schrödinger-Poisson model for this structure, we will assume translational invariance along its planar directions, which will reduce the Schrödinger (3.1) and Poisson equation (2.5) to 1D equations, which are computationally easy to handle. Most importantly we will see that this allows us to include hybdridization effects between the metal and semiconductor in the quantum mechanical description of the system.

The second model geometry, shown in Fig. 3.2 (**b**), is essentially a cut through the 2D cross

section of the experimental device in Fig. 2 (**a**). Here we have thus assumed translational invariance along the nanowire and focused on the electrostatic effects of the back gate below the dielectric layer. Similar to the planar geometry we assume this to be held at a voltage V_G with respect to the grounded metallic superconductor. Because of translational invariance along the wire, the Schrödinger equation (2.4) and Poisson's equation (2.5) for this geometry will be 2D equations, which are computationally harder to handle than the 1D versions used for the planar structure. Notably we will see that this forces us to neglect hybridization effects between the metal and semiconductor.

Chapter 4

The Planar Geometry

We are now ready to apply our simulation model to the planar geometry. We start by outlining the details of how to set up the Schrödinger-Poisson model and then move on to discuss various simulation results.

4.1 Setting Up the Schrödinger-Poisson Model

We will start by setting up the Schrödinger-Poisson model for the planar geometry. Doing so, we will also discuss the simpler case of the same geometry but without the gate and dielectric. As we shall see the only difference between the two cases is the boundary condition used for Poisson's equation (2.5).

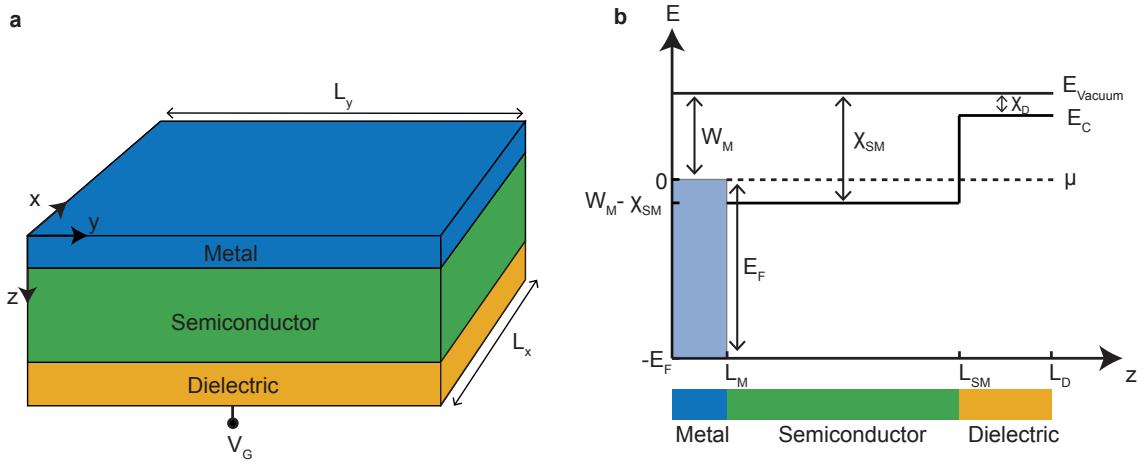

*Figure 4.1: Geometry and band diagram for the planar structure. (**a**) Sketch of the planar geometry oriented with its planar directions along the x- and y-direction and the perpendicular direction along the z-axis. The lengths of the structure along the x- and y-direction are denoted L_x and L_y, respectively. (**b**) Band diagram along the z-direction for the planar structure without electrostatic interaction. We choose the Fermi level, which is set by the work function of the metal, to be at zero energy.*

4.1.1 The Structure

We consider the structure shown in Fig. 4.1 (**a**), which shows a planar semiconductor-metal junction placed on top of a dielectric layer. The dielectric material is contacted to a gate electrode from below, which is held at a voltage V_G with respect to the metallic layer. The lengths of the structure in the x- and y-direction are denoted as L_x and L_y and we will assume that these are much longer than the thickness of the junction such that translational invariance along these directions may be employed.
Fig. 4.1 (**b**) shows the band diagram for the system without electrostatic effects. The relative offset between the band edges of the different materials is determined by the electron affinities of the semiconductor and dielectric as well as the work function and Fermi energy of the metal. Since the dielectric is an insulator its electron affinity, χ_D, is assumed close to the vacuum level while the semiconductor electron affinity, χ_{SM}, is closer to the work function of the metal, W_M. As discussed in the previous chapter we will assume that it is the work function of the metal that sets the Fermi level of the hybrid system and therefore choose this as our reference energy.

4.1.2 The Schrödinger Equation

Let us first discuss how to solve the Schrödinger equation for our system. As previously mentioned we will assume that the conduction band electrons may be described by the Schrödinger equation (3.1), which in the presence of translational invariance in the planar directions has the form

$$-\frac{\hbar^2}{2}\boldsymbol{\nabla}\cdot\Big(\frac{1}{m^*(z)}\boldsymbol{\nabla}\psi\Big)+\big(E_c(z)-e\phi(z)\big)\psi=E\psi. \tag{4.1}$$

From Fig. 4.1 (**b**) we see that the band edge term $E_c(z)$ is given by

$$E_c(z)=\begin{cases}-E_F & 0\leq z\leq L_M\\ W_M-\chi_{SM} & L_M<z\leq L_{SM}\\ W_M-\chi_D & L_{SM}<z\leq L_D\\ W_M & \text{Elsewhere}\end{cases} \tag{4.2}$$

For our model only states with energies far below the vacuum level $E<0<<W_M$ will be important, since these are the ones that contribute to the electron density in the system. We may therefore without loss of generality assume that $E_c(z)$ is infinite in the vacuum and

dielectric regions such that[1]

$$\psi(x,y,0) = \psi(x,y,L_{SM}) = 0.$$

The essential parameters of (4.2) is therefore the Fermi energy of the metal as well as the offset between the electron affinity of the semiconductor, which we throughout this chapter will denote as $\Delta = \chi_{SM} - W_M$.
As it stands (4.1) represents a three-dimensional eigenvalue problem. Because of translational invariance in the parallel directions, we can however reduce it to a one-dimensional problem by inserting an ansatz wave function of the form

$$\psi(\mathbf{r}) = \psi(z)e^{i\mathbf{k}_\parallel \cdot \mathbf{r}} \quad , \quad \mathbf{k}_\parallel = (k_x, k_y, 0).$$

Doing so we find

$$-\frac{\hbar^2}{2}\frac{d}{dz}\Big(\frac{1}{m^*(z)}\frac{d\psi}{dz}\Big)+\Big(\frac{\hbar^2\mathbf{k}_\parallel^2}{2m^*(z)} + E_c(z) - e\phi(z)\Big)\psi(z) = E\psi(z). \tag{4.3}$$

From this we can see that the effect of the parallel directions is an additional potential term given by

$$\frac{\hbar^2\mathbf{k}_\parallel^2}{2m^*(z)} = \begin{cases} \frac{\hbar^2\mathbf{k}_\parallel^2}{2m} & 0 \le z \le L_M \\ \\ \frac{\hbar^2\mathbf{k}_\parallel^2}{2m^*} & L_M < z \le L_{SM} \end{cases} \tag{4.4}$$

To handle this term we must know the quantization values of the parallel momenta, which may be found by imposing standard periodic boundary conditions[2] in the x- and y-directions yielding

$$k_x = 0,\ \pm\frac{2\pi}{L_x},\ \pm\frac{4\pi}{L_x},\ \pm\frac{6\pi}{L_x}, ... \qquad k_y = 0,\ \pm\frac{2\pi}{L_y},\ \pm\frac{4\pi}{L_y},\ \pm\frac{6\pi}{L_y}, ... \tag{4.5}$$

For each $\mathbf{k}_\parallel$ there is now a set of distinct wave functions $\{\psi_{n,\mathbf{k}_\parallel}\}$, which may be found by inserting in (4.3) and solving. We note that it is the mismatch between the effective masses in the two systems that creates this complication. Had the effective mass in the metal and the semiconductor been the same, the wave functions would be unchanged by the term (4.4)

[1] The problem of solving the Schrödinger Equation the gate and dielectric is therefore the same, since in both cases (4.1) is only solved in the metal and semiconductor region.

[2] see for example Kittel [16] page 137.

since it would simply represent a constant shift of the energies[3].

4.1.3 Calculating the Electron Density

The next step of the Schrödinger-Poisson method is to calculate the electron density according to (2.3), where the sum index runs over all occupied states in our system. These are the solutions to (4.3) whose energies lie below the Fermi level. In general there will be a huge number of wave functions satisfying this condition since there is a distinct wave function belonging to each combination of the parallel momenta (4.5) as we saw in the previous subsection.
Suppose that we have actually solved the Schrödinger equation for each $\mathbf{k}_\parallel$ yielding a set of wave functions $\{\psi_{n,\mathbf{k}_\parallel}\}$ with energies $E_{n,\mathbf{k}_\parallel}$. In this case the electron density may be computed as

$$\rho(z) = \frac{-2e}{L_x L_y} \cdot \sum_{\substack{n,\mathbf{k}_\parallel \\ E_{n,\mathbf{k}_\parallel}<0}} |\psi_{n,\mathbf{k}_\parallel}(z)|^2. \tag{4.6}$$

Where the factor of 2 comes from the fact that all wave functions are two-fold degenerate in spin space.
In practice (4.6) is tedious to work with. A simpler formula may be obtained by using that, since L_x and L_y are long compared to the thickness of the structure, the values of k_x and k_y may be assumed practically continuous, thus allowing us to replace the summation over $k_\parallel$ in (4.6) by an integration in polar coordinates

$$\rho(z) \approx -e \cdot \frac{1}{(2\pi)^2} \cdot 2 \cdot 2\pi \cdot \int dk_\parallel \; k_\parallel \sum_{\substack{n \\ E_{n,k_\parallel}<0}} |\psi_{n,k_\parallel}(z)|^2. \tag{4.7}$$

This is now the central equation for calculating the electron density. To use it in our numerical model we must first solve the Schrödinger equation for a set of values for $k_\parallel$ and then perform the integral numerically. Details of this numerical integration will be addressed later.

4.1.4 Poisson's Equation

Having calculated the electron density in our system we must calculate the electrostatic potential from Poisson's equation (2.5), which with translational invariance along the x- and y-directions takes the form

$$\frac{d}{dz}\left(\epsilon_r(z)\frac{d\phi}{dz}\right) = -\frac{-\rho(z)}{\epsilon_0}. \tag{4.8}$$

[3]Formally, if ψ_n is an eigenfunction of some Hamiltonian, H, then it is also an eigenfunction of $H + \frac{\hbar^2\mathbf{k}_\parallel^2}{2m^*}$ with energy $E_n + \frac{\hbar^2\mathbf{k}_\parallel^2}{2m^*}$.

To solve (4.8) we must specify the electrostatic boundary conditions in our system.
The first boundary condition should be specified at the semiconductor-metal interface and applies for both the case with and without contact to a gate and dielectric. Here we have the standard requirement (2.10) that the electrostatic potential goes to a constant value. We will choose the value of ϕ at this interface as the reference value for the electrostatic potential, that is

$$\phi(L_M) = 0.$$

The second boundary condition differs for the case with and without contact to a gate and dielectric. For the gated junction the boundary condition is simple. In this case the gate electrode imposes the requirement that the electrostatic potential should match the voltage set by the gate electrode, V_G, that is

$$\phi(L_D) = V_G. \tag{4.9}$$

For the case without a gate we must be more careful, since in this case there is no electrode that fixes the value of the electrostatic potential at the lower edge of the semiconductor. In this case we can argue as follows: Since we have assumed translational invariance in the x- and y-directions, we are basically studying the problem of calculating the electrostatic potential from an infinite slab of charged semiconductor with a total surface charge density given by

$$\sigma = \int_{L_M}^{L_{SM}} \rho(z) dz. \tag{4.10}$$

The electric field outside an infinite slab is generally given by[4]

$$E = \frac{\sigma}{2\epsilon_0}. \tag{4.11}$$

Which notably is independent on the distance from the slab. We can use this observation to argue that in order for the electric field to be zero inside the metal, there must be a layer of screening charges of opposite surface charge density $-\sigma$ at its surface, which exactly cancels out the field from the semiconductor charges.
At the lower edge of the semiconductor the total surface charge of the system, given by the surface charge of the semiconductor, σ, and the screening charge at the metal interface, $-\sigma$, will exactly cancel out such that the electric field at this point must also be zero. For the

[4]See for example Chapter 2 of [31].

electrostatic potential this amounts to the Neumann boundary condition that

$$-\frac{d\phi}{dz}\Big|_{z=L_{SM}} = 0. \tag{4.12}$$

4.2 Results

Let us now turn to the different results obtained from applying our model to the planar geometry in Fig. 4.1. We will start by focusing on the simple case without a gate electrode and subsequently move on to discuss effects of the latter. Finally we will focus on varying different parameters in our model and comparing it to simpler approaches.
The results of this chapter were mainly obtained for an InAs-Al junction with layer thicknesses 100nm and 5nm, respectively. In the cases, where we include a gate electrode, SiO_2 was used as the dielectric material with a layer thickness of 10nm. The values for the work function and Fermi energy of Al, electron affinity of InAs as well as the various dielectric constants were taken from the tabulated values shown in Table 1.2, 1.3 and 2.1. Notably these values yield and offset of $\Delta = 0.82$eV between the conduction band of InAs and Fermi level of Al. Altogether the values above define our standard choice of parameters and were used unless anything else is specified.

4.2.1 Semiconductor-Metal Junction without Gate Electrode

We focus first on the simplest case of an InAs-Al junction without a gate electrode and with the standard choice of parameters. Fig. 4.2 shows the converged band diagram for such a junction, where we have also provided a zoom-in around the Fermi level (black dashed line). The diagram shows both the band edge obtained from the self-consistent Schrödinger-Poisson method (solid blue line) and the band edge without electrostatic interaction (blue dashed line), which one would get from simply matching the band edges of the two isolated materials.

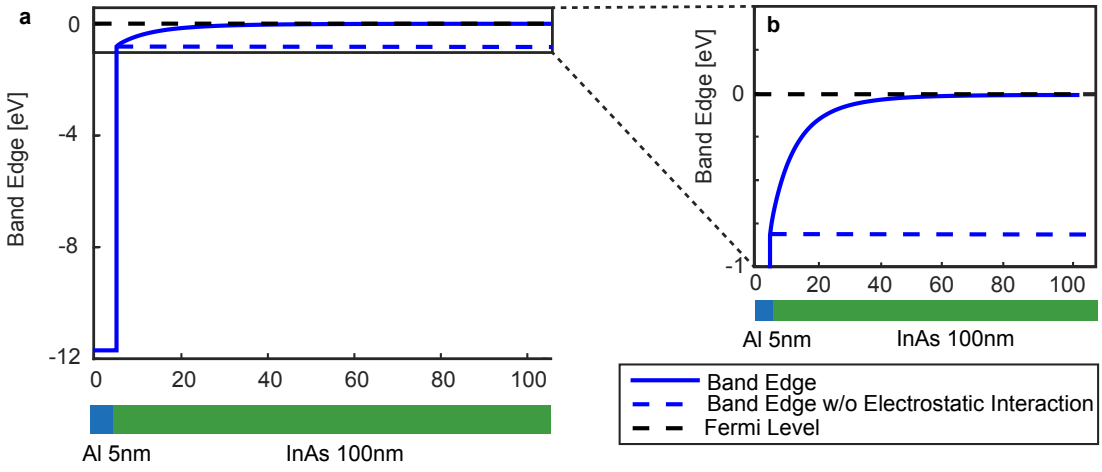

*Figure 4.2: Band diagram for an InAs-Al junction without a gate electrode and with the standard choice of parameters. (**a**) Full band diagram showing the band edge in both the metal and semiconductor region obtained from the self-consistent solution of the Schrödinger-Poisson problem (solid line) and without electrostatic interaction (blue dashed line). For the self-consistent solution the band edge saturates at the Fermi level of the system (black dashed line). (**b**) Zoom-in around the semiconductor band edge showing the electrostatic well at the semiconductor-metal interface.*

The most important feature of Fig. 4.2 is the character of the band bending. Moving away from the InAs-Al interface we see that the effect of the electrostatic potential is an upwards bending of the conduction band edge, which flattens out far from the interface due to the boundary condition that the field vanishes at the edge of the semiconductor. The effect of the band bending is therefore to create an electrostatic well in a region close to the InAs-Al interface. The physical origin of this well is the screening of the electric field from the Al, which is strong close to the interface.

A second important feature is the alignment of the band edge far from the interface. From Fig. 4.2 we see that this aligns with the Fermi level of the hybrid system. This expresses the physically reasonable result, that the electron density must vanish far from the InAs-Al interface. It may seem confusing that the band edge saturates *at* the Fermi level and not above it, which is the standard assumption in litterature on semiconductor-metal junction [19]. However, as we address later, this is an effect that owes to thermal excitations at finite temperatures and is consequently not captured by our simple model. For the subkelvin temperature regime relevant for measuring on Majorana devices, thermal excitations are negligible and our simple model produces identical results compared to a more complicated model, where finite temperature effects are included.

Let us now investigate the profile of the electron density in the system, which is shown in Fig. 4.3. Here Fig. 4.3 (**a**) shows the electron density in the full system while Fig. 4.3 (**b**)

and (**c**) show zoom-ins on particular regions of interest.

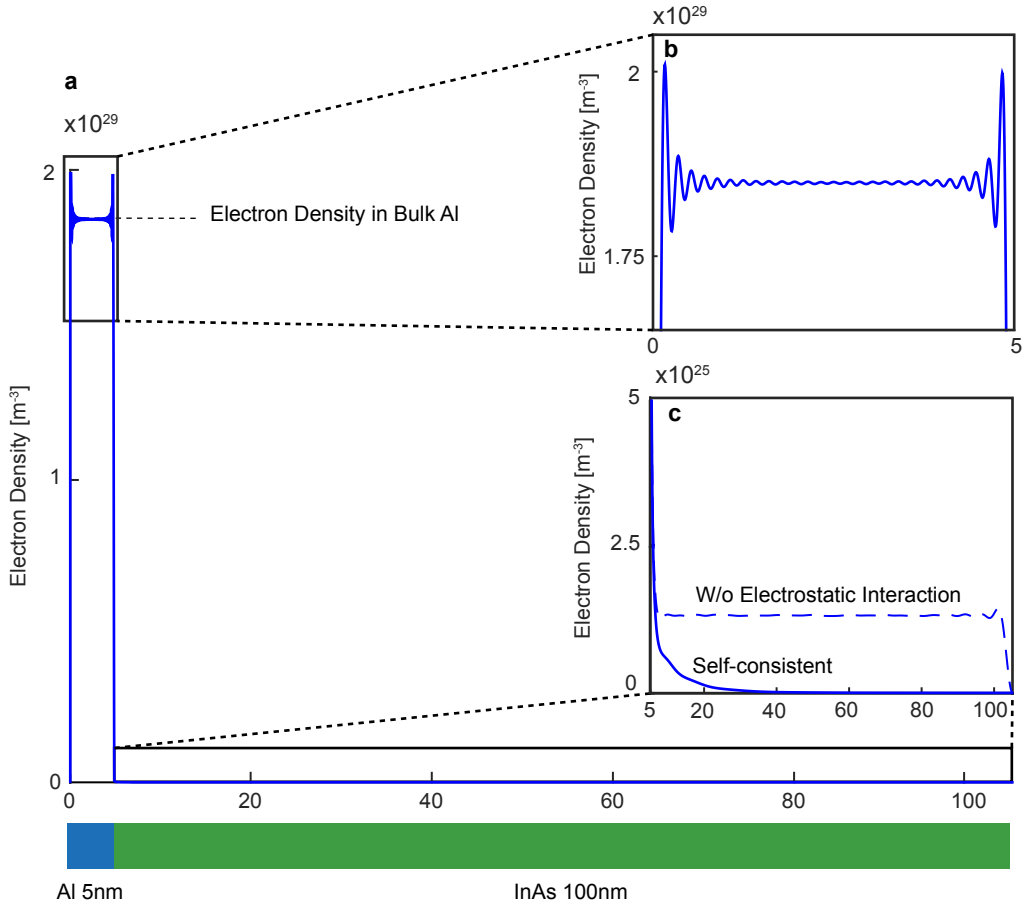

*Figure 4.3: Electron density for an InAs-Al junction without a gate electrode and with the standard choice of parameters. (**a**) Electron density profile in full system. This is completely dominated by the metallic region, where the electron density is centered around the bulk value with Friedel oscillations around the edges of the metal. (**b**) Zoom-in on the density profile in the metal showing the Friedel oscillations more clearly. (**c**) Zoom-in on the density profile in the semiconductor region. Evidently the density here is around three orders of magnitude smaller than inside the metal layer, indicating that only a small fraction of the electrons in the metal are allowed to spill in and hybridize with the conduction band states of the semiconductor.*

Evidently the profile of the electron density is dominated by the metallic region for which the density profile is centered around the bulk value of the electron density in Al with oscillations at the edges. These oscillations are shown more clearly in the zoom-in provided by Fig. 4.3 (**b**) and are a special case of the well-known Friedel oscillations that one observes at the boundaries of a solid or at defects in general [37].

For our purposes we are mainly interested in the density profile in the semiconductor region, which can be seen in the zoom-in in Fig. 4.3 (**c**). Here we show both the density obtained from

the self-consistent Schrödinger-Poisson method (solid line) as well as the one obtained without including electrostatic interaction (dashed line). Evidently the electrostatic interaction forces the density to decay inside the semiconductor region, which is consistent with the band edge profile of Fig. 4.2.

From Fig. 4.3 (**c**) we also see that only a tiny fraction of electronic states are allowed to spill in and hybridize with the empty conduction band states of InAs. In fact one sees that the electron density induced in the semiconductor is around three orders of magnitude smaller than that of the metal. The physical origin of this is of course the large Fermi energy of Al, which effectively creates a deep well in the metal region. Looking at Fig. 4.2 or consulting Table 1.3 we see that this mismatch is on the order of 10eV, which means that almost all electrons in the system are confined to the narrow metallic region in the system.

The above point can be made more evident if we make a small detour and look at the different types of solutions that one can expect to find from (4.3). In general these will depend on the value of the transverse momentum $k_{\|}$ so let us focus on the solutions for $k_{\|} = 0$. We will refer to these particular solutions as the different subband solutions of the hybrid system[5]. Fig. 4.4 shows a plot of three different subband solutions with their corresponding energies plotted inside the band edge profile of the system.

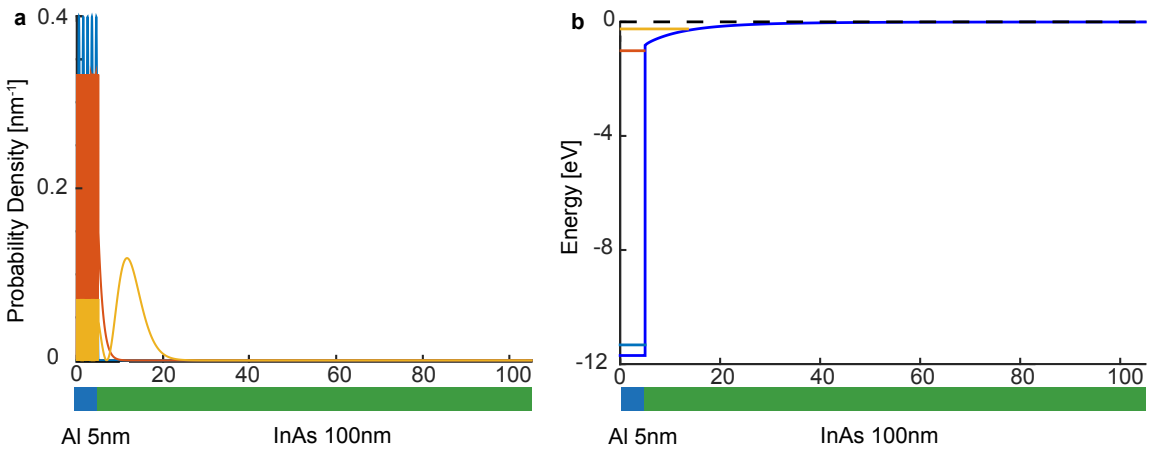

*Figure 4.4: Illustration of the different types of subband solutions found from solving the Schrödinger equation in the hybrid system. (**a**) Wave functions corresponding to a metallic state (blue), evanescent state (red) and delocalized state (yellow). (**b**) corresponding energies of the wave functions plotted inside the converged band diagram.*

[5]The origin of this language is the fact that if the effective mass had been constant over the junction, the solutions of the Schrödinger equation (4.3) would be independent of $k_{\|}$ and thus each would be degenerate with a parabolic band of energies belonging to it. For the present case the energy spectrum will still form a quasi-parabolic set of energy bands (see the section on the $k_{\|}$ dependence), and we therefore refer to the solutions for $k_{\|} = 0$ of these individual bands as the different subband solutions.

Let us discuss the character of the wave functions shown in Fig. 4.4 (**a**). In general they represent the different types of solutions that one can expect to find for our system.
The lowest energy wave function (blue) has an energy close to the band edge of Al and is therefore completely localized in the metallic region of the system. We will refer to this type of subband solution as metallic.
The solution with second lowest energy is marked by red. Similar to the first wave function it has an energy below the InAs conduction band edge but this time its energy is much closer to the conduction band edge, which therefore allows it to have a significant leak into the semiconduction region as seen from its decaying tail in the InAs region. We will refer to this type of subband solution as evanescent due to its evanescent character in the semiconductor region.
Finally the wave function marked by yellow has an energy above the conduction band of InAs. In this case the wave function is delocalized both inside the metal and semiconductor region. For this reason we refer to this type of subband solution as delocalized.
Returning to the original question, the crucial point is now that most of the electrons that contribute to the density in the hybrid system belong to metallic solutions which are confined to the metallic region. Only a small fraction of states close to the conduction band edge of InAs has a significant contribution to the density in the semiconductor region.
You may think that the argument above is flawed, since we only argued based on the different types of subband solutions and did not discuss the effect of the $k_{\|}$-dependence. Since the effective mass is smaller in the InAs region, we can however see from (4.4) that finite values of $k_{\|}$ only has the effect of localizing the states even more inside the metal. We will discuss this in more detail, when we later address the exact dependence of the energies on $k_{\|}$.

4.2.2 Gated Semiconductor-Metal Junction

Let us now turn to the gated junction, for which the semiconductor-metal heterostructure sits on top of a gated slab of dielectric. A calculation for this structure is shown in Fig. 4.5 which shows the converged band diagram (**a**) and electron density profile (**b**) with the standard choice of parameters. The gate voltage is here set to $V_G = 0$ but below we will also investigate effects of varying this value.

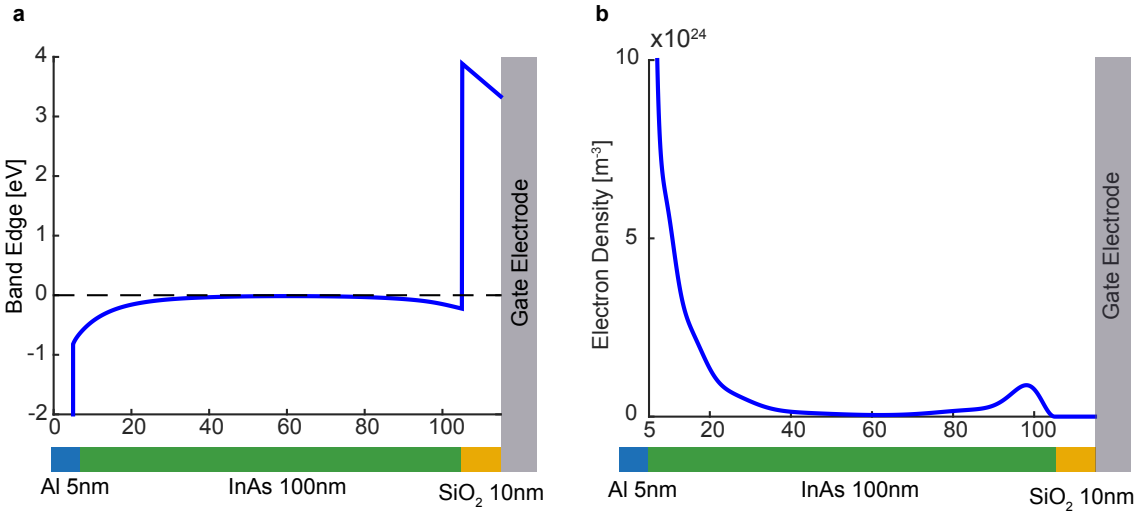

*Figure 4.5: Self-consistent solutions for a gated junction with $V_G = 0V$. (**a**) Band edge profile which clearly shows an electrostatic well on either side of the InAs region. (**b**) Density profile in the InAs region. In this case the density is peaked both at the InAs-Al interface as well as the InAs-SiO_2 interface.*

Comparing Fig. 4.5 (**a**) to the band diagram without the gate electrode in Fig. 4.2 we notice several differences.

First of all we have included the dielectric region in the band edge profile of the system. Since the dielectric is an insulator $E_c(z)$ is close to the vacuum level (see Fig. 4.1 (**b**)) in this region, which is the reason that the band edge profile jumps abruptly at the semiconductor-dielectric interface.

A second important difference is the character of the band bending. From Fig. 4.6 we see that when moving away from the InAs-Al interface the band edge first rises similarly to Fig. 4.2 thereby creating an electrostatic well at the InAs-Al interface. But rather than saturating at the Fermi level it starts to decrease towards the dielectric region thus creating a second electrostatic well at the opposite end of the semiconductor layer. Once inside the dielectric region this decrease continues linearly, which reflects the fact that the charge density is zero such that Poisson's equation (4.8) reduces to Laplace's equation[6]. The effect of the dielectric region is thus simply a renormalization of the value of the electrostatic potential at the semiconductor edge, which can be calculated trivially for any dielectric layer of arbitrary thickness as long as the electrostatic potential and electric field are known at this point. Assuming that these are known to be V_{SM} and E_{SM} we find from combining the solution of

[6]Formally the solution to $\frac{d^2\phi}{dz^2} = 0$ is on the form $\phi(z) = az + b$ with constants that must be determined by matching with the electrostatic potential at the semiconductor edge.

Laplace's equation and the standard boundary conditions (2.9)

$$V_G = V_{SM} - \frac{\epsilon_{SM}}{\epsilon_D} E_{SM} \cdot (L_D - L_{SM}). \tag{4.13}$$

For the results presented in the remainder of this chapter we will simply specify the electrostatic potential and electric field at the semiconductor edge. These results may then be interpolated to the gate voltage corresponding to a dielectric of arbitrary thickness and dielectric constant using (4.13).

Let us also discuss the profile of the electron density for the gated junction, which is shown for the semiconductor region in Fig. 4.5 (**b**). Similar to the case without a gate (Fig. 4.3 (**c**)) we observe that the electron density is peaked at the InAs-Al interface indicating the presence of an electrostatic well due to the screening of the Al layer. But unlike the case without a gate we also observe that the electron density is peaked at the semiconductor-dielectric interface. This behaviour is in agreement with our observation that the band edge in Fig. 4.5 effectively creates an electrostatic well on either end of the semiconductor layer. The origin of the well at the dielectric interface is of course not surprising since for $V_G = 0$ both the gate electrode and metallic layer act as screeners for the electric field. The screening from the gate electrode is however weaker, since the dielectric here acts as a buffer layer for the decay of the electrostatic potential.

Based on our discussion above, it is natural to ask how the electrostatic profile and electron density in our system will respond as we change the gate voltage in our system. The result of such an investigation is shown in Fig. 4.6 (**a**), which shows the converged band profile in our system for different values of the V_{SM}.

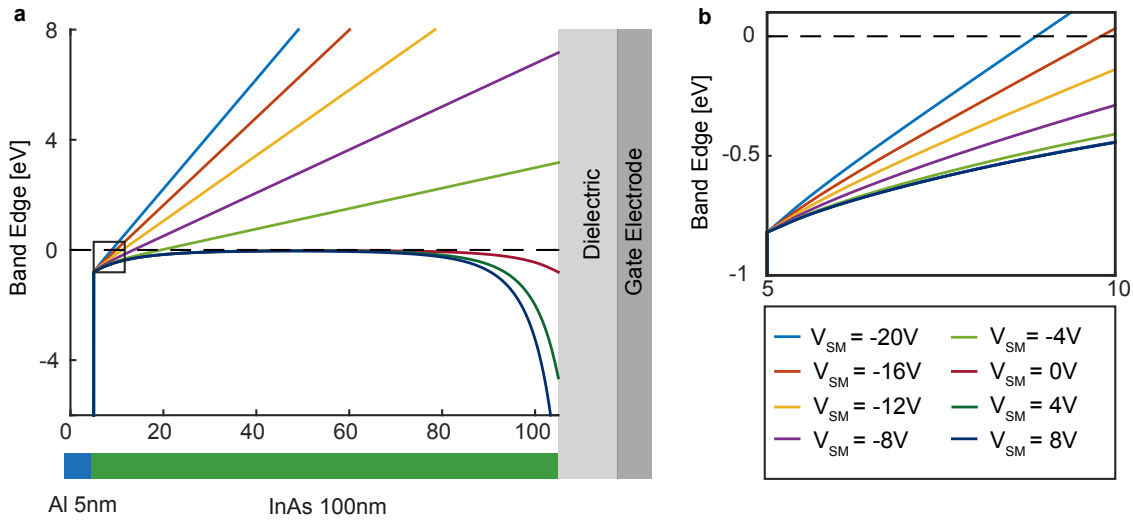

Figure 4.6: Band edge profile for different values V_{SM}. Values of the electric field at the semiconductor edge are (starting from most negative value of V_{SM} indicated by blue): 0.199V/nm, 0.159V/nm, 0.119V/nm, 0.078V/nm, 0.037V/nm, -0.0815V/nm, -0.769V/nm, -1.659V/nm.
*(**a**) Band edge profile in the full system. The profile is approximate linear for negative values of V_{SM} and then starts to flatten as we approach positive values. (**b**) Zoom in around the InAs-Al interface. Evidently the band edge tends to a constant slope when approaching positive values of V_{SM}.*

Starting from negative values of V_{SM} we see that the band edge profile is approximately linear but as we approach positive values the band bending starts to flatten out in the middle of the InAs region. For positive values of V_{SM} this behaviour persists but the band edge now starts to bend down on the right hand side to match the voltage set by the gate electrode.
Fig. 4.6 (**b**) shows a zoom-in of the band edge at the interface. Evidently as we increase the value of V_{SM} the profile of the band edge around the interface changes less and less and tends towards a constant electric field.
Let us try to understand the physics behind the flattening of the band edge in Fig. 4.6. To do so it is useful to think about what happens physically as we iterate towards the self-consistent solution of the problem. During the first iteration the band edge will simply be linear with a slope given by $\frac{V_{SM}}{L_{SM}-L_M}$, since in this case we have not yet included the electrostatic interaction between the electrons in the semiconductor. As we then start to iterate towards the self-consistent solution, the electrostatic interaction will begin to push up the band edge of the semiconductor. The effect is most prominent in the middle of the InAs region, since the value of the electrostatic potential is fixed on either end of the junction by the Al layer and gate electrode, reflecting the screening properties of these components. This behaviour continues until effectively all electrons have been away from the middle region. A closer inspection of Fig. 4.6 reveals that this happens when the middle part of the band edge hits the Fermi level, which is exactly what one would expect from a simple classical argument where the electrons have an energy given by the local value of the band edge.

From the argument above one would expect that the density profile in our system will be peaked around the edges of our system and vanishing in the middle of the junction. To confirm this suspicion we consider Fig. 4.7 shows the corresponding density profiles in the system.

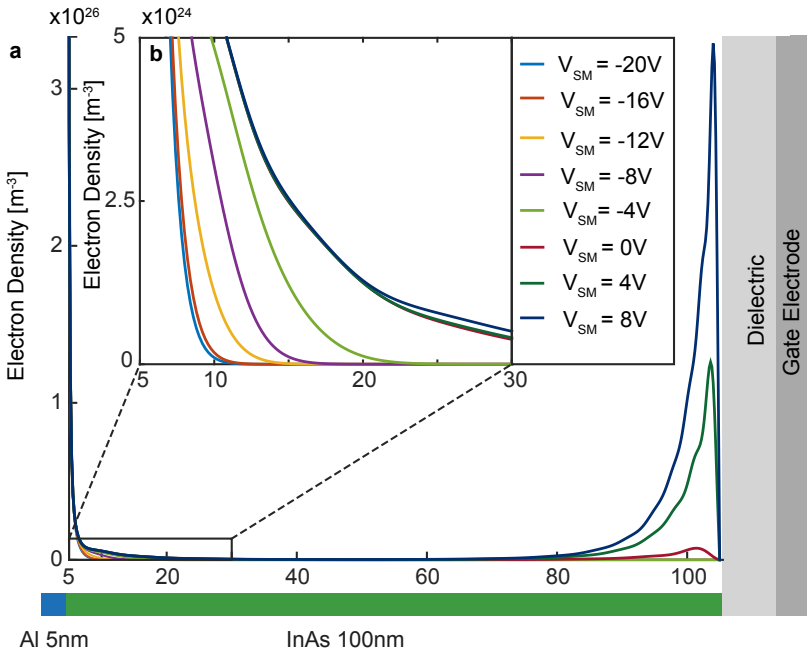

*Figure 4.7: Density profile in InAs region corresponding to the band edges of Fig. 4.6. (**a**) Density profiles in the full system. This plot is dominated by the electron density for the positive values of V_{SM}. (**b**) Zoom-in around the metal interface showing the profiles for negative values of V_{SM}. Evidently the electron density is pushed closer to the metallic edge by larger negative values of V_{SM}.*

As we expected, the density profiles for all values of V_{SM} is vanishing in the middle part of the InAs region. For the negative values shown in Fig. 4.7 (**a**) the density is confined to a narrow region around the InAs-Al interface, which is what one would expect by looking at the band edge profiles in Fig. 4.6. For the positive values of V_{SM} shown in Fig. 4.7 (**b**) the density profile is non-vanishing both at the semiconductor-metal interface as well as the semiconductor-dielectric interface reflecting the downwards bending towards the dielectric interface.

4.2.3 The Effective Mass Mismatch

We now focus on the consequences of the mismatch between the effective mass of the semiconductor and metal region. We previously argued that the effects of this mismatch is that the electron density should be calculated using (4.7), which forces us to solve the Schrödinger

equation (4.3) a large number of times within each iteration. Since this is obviously computationally demanding, let us first investigate the dependence of the wave functions on $k_\parallel$ to determine whether this is significant or may be neglected without loss of generality.
We consider once again an InAs-Al junction with the standard choice of parameters. We focus on the first subband, which has an energy above the conduction band minimum of InAs[7]. Fig. 4.8 shows what happens to the form of the wave functions belonging to this subband for succesively larger values of $k_\parallel$.

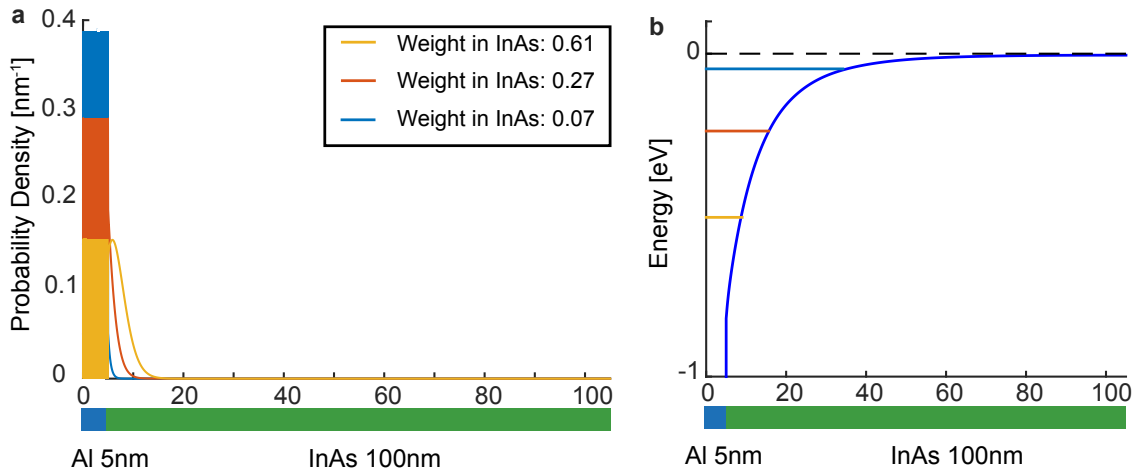

*Figure 4.8: Illustration of the strong dependence of the wave functions on $k_\parallel$. (**a**) Wave functions for three different values of $k_\parallel$. The yellow wave function ($k_\parallel = 0$) has the largest weight in the semiconductor region, since the effect of larger values of $k_\parallel$ is to localize the wave functions more in the metallic region. (**b**) Energies of the corresponding wave functions. Note that the energy differences are purely due to different values of $k_\parallel$.*

Evidently the wave functions become increasingly localized in the metallic region for larger values of $k_\parallel$, which is consistent with the term (4.4) and the fact that the effective mass is smaller in the InAs region. The physical interpretation of this is that the electrons prefer to be localized in the metallic region since the kinetic energy due to their movement in the planar directions is then smaller. From Fig. 4.8 we also see that the effect of the $k_\parallel$-term on the wave functions is not small, since the weight in the InAs region of the wave function with highest energy is only 12% of the weight for the wave function corresponding to $k_\parallel = 0$.
To dig further into the problem, let us investigate the dependence of the subband energies on $k_\parallel$[8] and compare to the situation, where the masses in the semiconductor and metallic region

[7] As we shall see below this is the most relevant state since it contributes most to the density in the semiconductor region.

[8] Here we include negative values of $k_\parallel$, which is a slight abuse of notation since this is, strictly speaking, the modulus of $\mathbf{k}_\parallel$. The plots below should therefore be seen as a cut through the 2D bandstructure, which one would obtain from plotting $E(\mathbf{k}_\parallel)$.

are the same. In the latter case we already know that the $k_{\|}$-term of (4.3) simply represents a constant offset and the energies belonging to each subband would therefore simply be a set of paraboloids in $\mathbf{k}_{\|}$-space with a curvature determined by the common effective mass of the two regions. For our case, where there is a mismatch between the effective masses, this will not be the case, since the effective mass of each subband dependends on its weight in the semiconductor and metallic region. This is evident in Fig. 4.9 which shows the dependence of the subband energies on $k_{\|}$ for an InAs-Al junction with the standard choice of parameters.

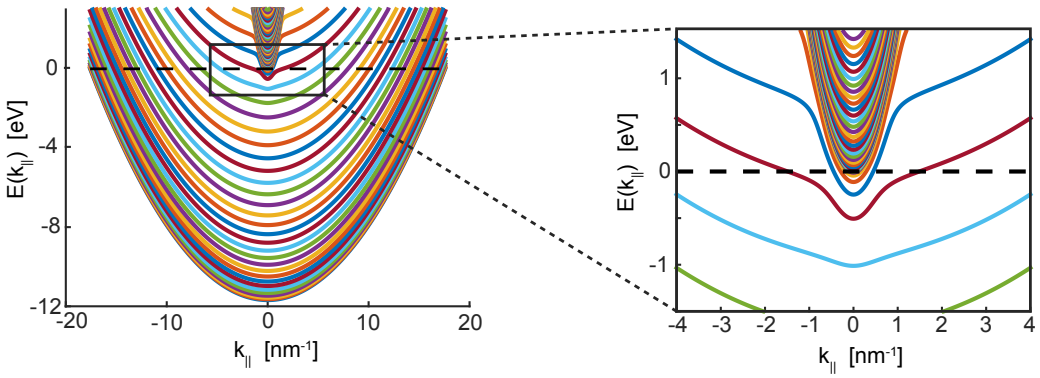

Figure 4.9: Cut through $E(\boldsymbol{k}_{\|})$ showing the effect of the effective mass mismatch in the InAs and Al region. For the lowest energy subbands the coupling is weak and they have parabolic dispersions determined by the electron mass in Al. As we approach subbands close to the Fermi level, hybridization effects become stronger and the dispersions show both semiconductor and metallic character.

In Fig. 4.9 each colored line represents a subband of energies. Starting from the ones with energies far below the Fermi level, we see that these subbands have approximately parabolic dispersions with a curvature determined by the mass in the metallic region. This is exactly what one would expect since these are predominantly metallic and have vanishing coupling to the semiconductor. As we approach the Fermi level the subbands start to couple to the semiconductor making their energy dispersions sharper due to the lower effective mass of InAs. This effect is for example evident for the subband marked by the magenta color in Fig. 4.9. The states of this subband have a high InAs character around $k_{\|} = 0$ and then become increasingly more metallic for larger values of $k_{\|}$ as is evident from the flattening of the energy dispersion. The wave functions belonging to this subband are exactly the ones we plotted in Fig. 4.8.

It is natural to ask which subbands of Fig. 4.9 contribute significantly to the density in the semiconductor region. To answer this question we consider Fig. 4.10, which shows the integrated density in the semiconductor region for each subband of (4.3).

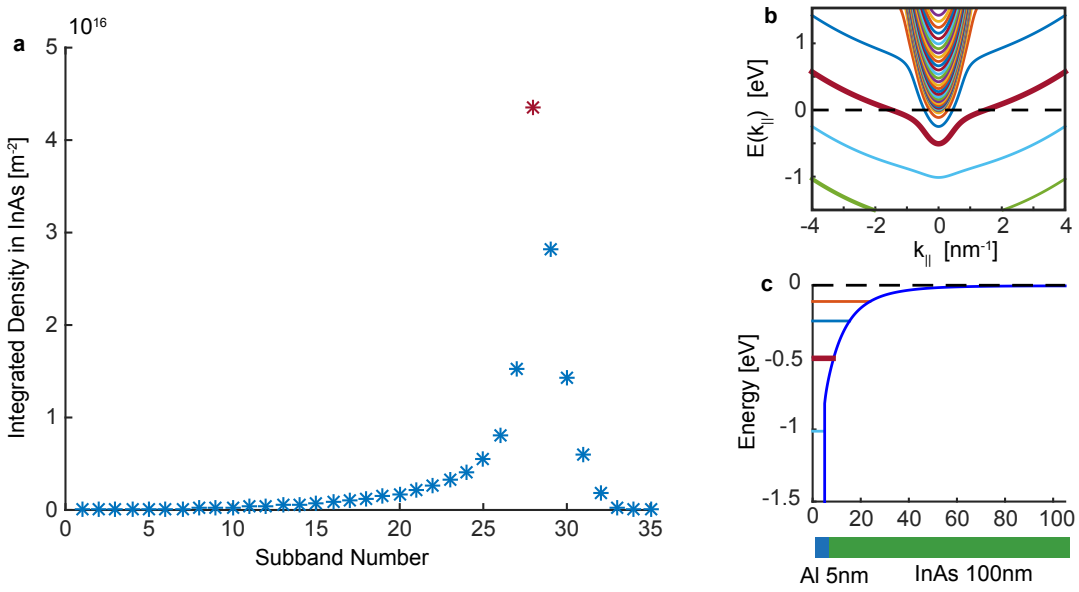

*Figure 4.10: Investigation of the contribution to electron density in the semiconductor region of each subband. (**a**) Integrated density in semiconductor region for each subband. Evidently the highest contribution comes from the one highlighted in magenta. (**b**) Plot of $E(k_{\|})$ around the Fermi level with the subband with largest contribution to the semiconductor density highlighted. (**c**) Self-consistent energies of the Schrödinger equation (4.3) with $k_{\|} = 0$. The energy corresponding to the subband with highest contribution to the density in the semiconductor is highlighted in magenta.*

From Fig. 4.10 we see that the most significant contribution to the electron density in the InAs region comes from the subband highlighted in magenta. This is exactly the subband that we investigated in Fig. 4.8, which therefore also serves to show that the effect of the effective mass mismatch cannot be neglected.

4.2.4 The Hybridization Between the Metal and Semiconductor

One of the biggest motivations for our work is that a detailed understanding of the electrostatics of Majorana devices could prove important for understanding variations in physical quantities related to the formation of Majorana zero modes. For a quantitative description of such variations we would need a more detailed microscopic model than ours, which explicitly includes effects such as a finite magnetic field, spin-orbit coupling and induced superconductivity, which are the key components of realizing Majorana zero modes. Details such as these are beyond the scope of this thesis. We can however make a qualitative motivation for the relevance of our work by investigating how the hybdrization between the metal and semiconductor depends on the value of the electrostatic potential at the semiconductor edge, V_{SM}. As a measure of the hybridization we will use the weight of the wave function in the semiconductor region for the different subbands in our system. We focus only on the wave functions with energies at the Fermi level since these are the ones that would be probed in transport

experiments. Furthermore we will focus only on the subbands with wave functions that have a significant weight in the semiconductor chosen as 0.1 or above. Fig. 4.11 shows the result of such an investigation with the relevant subbands indicated on the right for the smallest and largest of the investigated values of V_{SM}. Notice that we only plot the weight of the wave function if the corresponding subband is occupied.

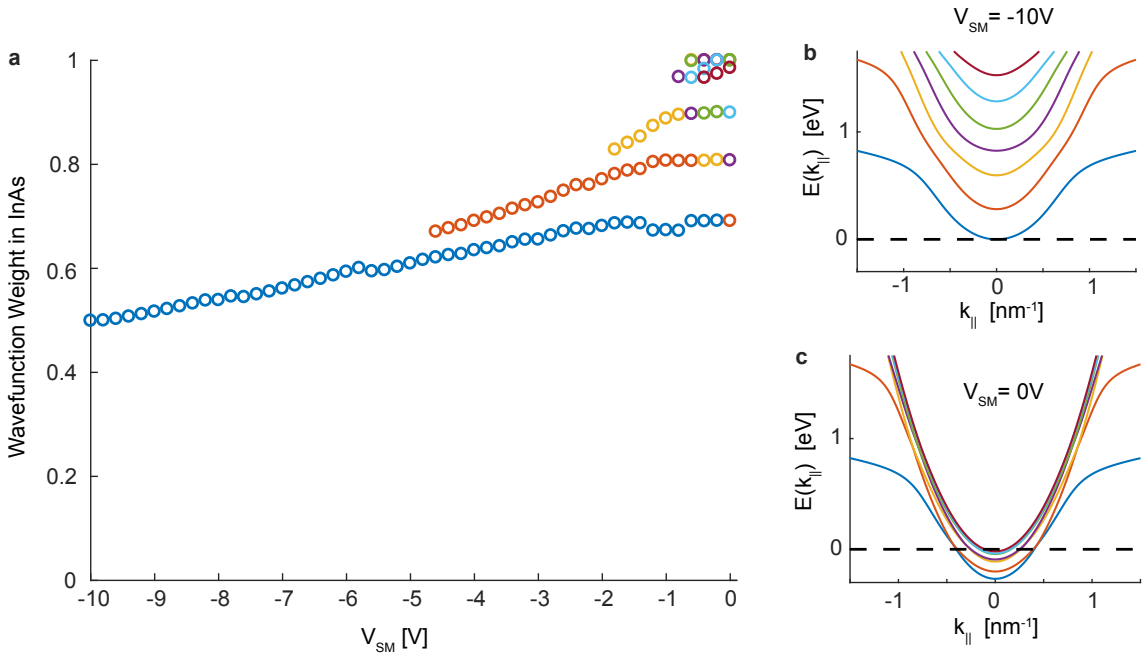

*Figure 4.11: (**a**) Weight in the InAs region of selected wave functions. Only wave functions with energies at the Fermi level and with a weight of 0.1 or above are shown. Note that some of the points are not visible due to overlapping. (**b**) Subbands at $V_{SM} = -10V$ corresponding to the wave function weights on the left. In this case only one of the corresponding subbands is occupied. (**c**) Subbands at $V_{SM} = 0V$ corresponding to the wave function weights on the left. In this case all subbands are occupied.*

From Fig. 4.11 (**a**) we see that for large negative values of V_{SM} only one occupied subband has a significant weight in the semiconductor. This corresponds to the situation shown in Fig. 4.11 (**b**), where all subbands except the lowest are above the Fermi level. As we then move towards positive values of V_{SM} more and more subbands become occupied which at the final value $V_{SM} = 0$ results in several subbands being occupied with weights ranging between 0.5 and 1. Interestingly we note that there appear to be no wave functions with weights between the critical value 0.1 and 0.5, which seems to hold even for more negative values of V_{SM} not included in Fig. 4.11. This should however be more carefully investigated in future work.

4.2.5 Varying the Model Parameters

So far all the results presented were obtained for a particular thickness of the metal and semiconductor region as well as the tabulated values of the work function and electron affinities of Table 1.2 and 1.3.

An important question to ask is how our overall conclusions change as we vary these input parameters. For the thicknesses such an investigation is important since the ultimate goal of our model would be to compare its results to actual experiments for which the exact physical dimensions will vary. For the values of the electron affinity and work function such an investigation is however equally important, since the tabulated values for these parameters should be seen as guiding values with some uncertainty to them.

There are essentially two reasons for this uncertainty. The first is that these values appear to fluctuate substantially in litterature. The work function for Al has for example been reported to have values between 4.08eV [24] and 4.28eV [38], which is a large deviation on the energy scales that we are interested in. The second reason, which is connected to the first, is that the values of the work function and electron affinity for a material are surface-dependent parameters, which are sensitive to several factors related to its surface chemistry such as its morphology, the method of preparation, oxidation etc.

We start off by investigating effects of varying the thickness of the Al layer while the keeping the other parameters fixed at their standard values. Fig. 4.12 shows the band edge profile (**a**) and electron density (**b**) in our system for three different values of the Al thickness. The calculation is here based on the simple case without a gate electrode, but the overall conclusion holds true also for the gated junction.

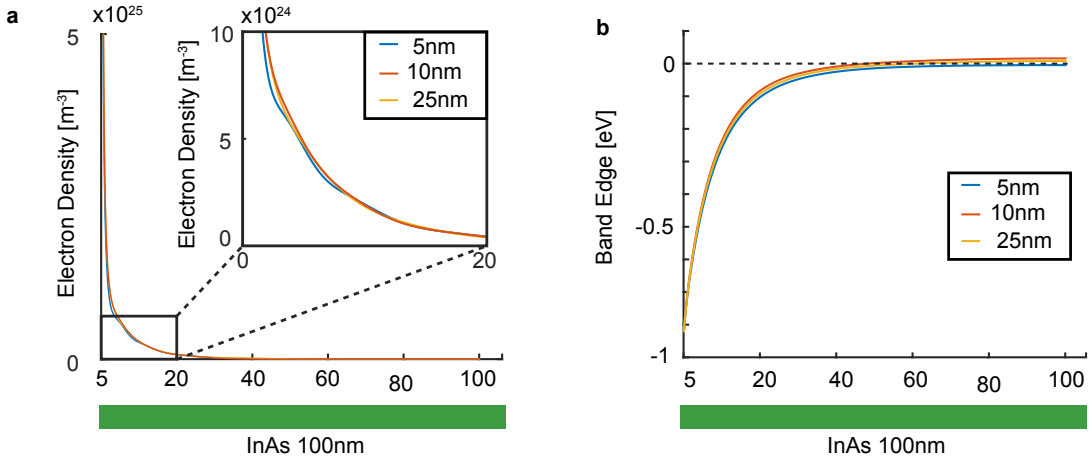

*Figure 4.12: (**a**) Band edge profiles for Al layer thicknesses of 5nm, 10nm and 25nm respectively. (**b**) Electron density profiles for Al layer thicknesses of 5nm, 10nm and 25nm respectively.*

From Fig. 4.12 we see that the profiles of the electron density and electrostatic potential are

quite stable to changing the width of the metal layer, which indicates that the results of this chapter are not just a coincidence of the particular value chosen for the thickness of the Al layer.

Focusing next on varying the thickness of the InAs layer, the result of such an investigation is shown in Fig. 4.13. Here we once again plot the band edge (**a**) and density profile (**b**) for the simple case without a gate electrode.

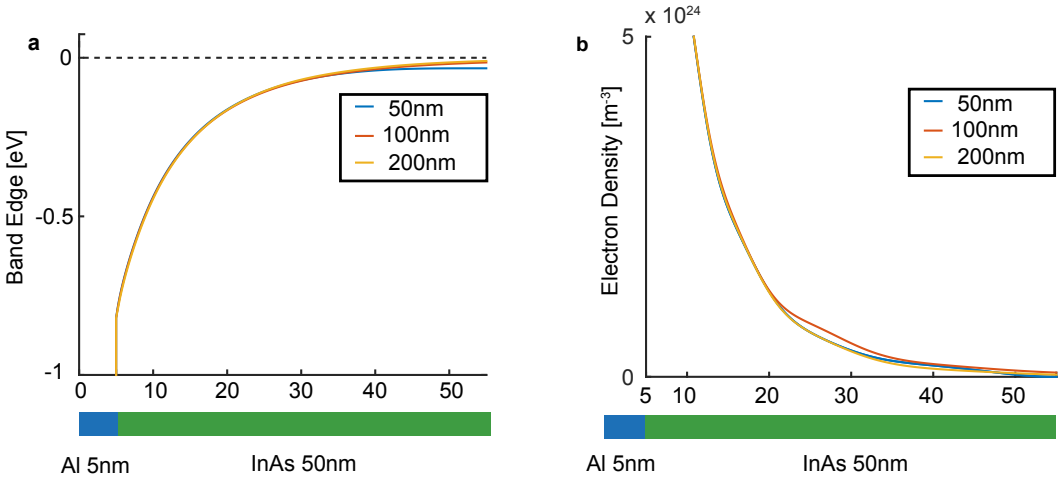

*Figure 4.13: (**a**) Band edge profiles for InAs layer thicknesses of 50nm, 100nm and 200nm respectively. (**b**) Electron density profiles for InAs layer thicknesses of 50nm, 100nm and 200nm.*

Similar to before we see that the profiles of the electron density and electrostatic potential are quite stable to changing the width of the semiconductor layer, indicating once again that the results of this chapter are not just a coincidence of the particular value chosen for the thickness of the InAs layer. We should however note, that for the case where the gate electrode is included the band edge and density profiles will of course depend on the semiconductor thickness, since in this case the semiconductor thickness determines the distance from the gate electrode to the semicondictor-metal interface.

Let us finally investigate effects of varying the offset between the work function of Al and electron affinity of InAs, which for all our simulations so far was assumed to be $\Delta = 0.82$eV. Fig. 4.14 shows the electrostatic and density profile for different values of this offset. The calculations below were once again done for the simplest case without a gate.

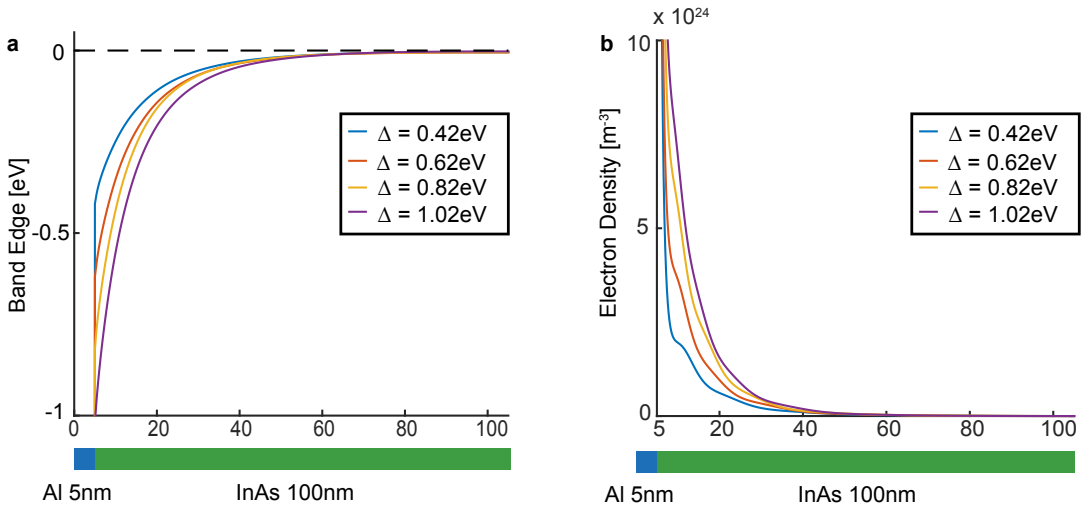

*Figure 4.14: (**a**) Band edge profiles for different values of the offset, Δ, between the metal work function and electron affinity of the semiconductor. In this case there are significant differences between the resulting electrostatic profiles. (**b**) Electron density profiles for different values of the offset, Δ, between the metal work function and electron affinity of the semiconductor, indicating that our results for the density profile are very dependent on this value.*

This time we see that there are substantial differences between both the band edge (**a**) and density profiles (**b**). This is not very surprising since the value of Δ determines how many electronic states of the metal that spill in and hybridize with the semiconductor, but it does show us that we should be careful about applying our model to experimental systems. The safest approach would probably be to use Δ as an unknown fitting parameter, which could then be extracted by comparing to different experiments. It is however likely that these values would fluctuate, because of the sensitivity of Δ to factors related to the surface chemistry of the system.

4.3 Comparison with Simpler Models

The above concludes the results obtained from applying our model to the planar structure. This section is devoted to comparing some of the above results to simpler approaches, which are computationally easier to handle. We will also address effects of adding a finite temperature to our model.

4.3.1 Neglecting the Metal in the Schrödinger Equation

In the model we have set up the Schrödinger equation (4.3) is solved both inside the metal and semiconductor region of Fig. 4.1. An obvious question to ask is how the results of this

approach compare to a more simple approach where (4.3) is solved only in the semiconductor region with the boundary condition that the wave function is zero at the InAs-Al interface. This question is especially interesting since we will use this simpler approach in the next chapter, where we solve the Schrödinger equation in a 2D nanowire system. For understanding hybdridization effects such as those of Fig. 4.11 the comparison seems a bit meaningless since the essence of the simpler approach is precisely to neglect these. If however the two approaches turned out to yield identical results, one could argue for using the simpler approach for solving the self-consistent problem and then "adding" the resulting electrostatic profile to a more detailed model which included the hybridization between the metal and semiconductor as well as other microscopic effects. We will return to this point later in this section.
Fig. 4.15 shows a comparison between the band edge in the semiconductor region for the two approaches above. The profiles shown were calculated for an InAs-Al junction with the standard choice of parameters and for three different values of V_{SM}.

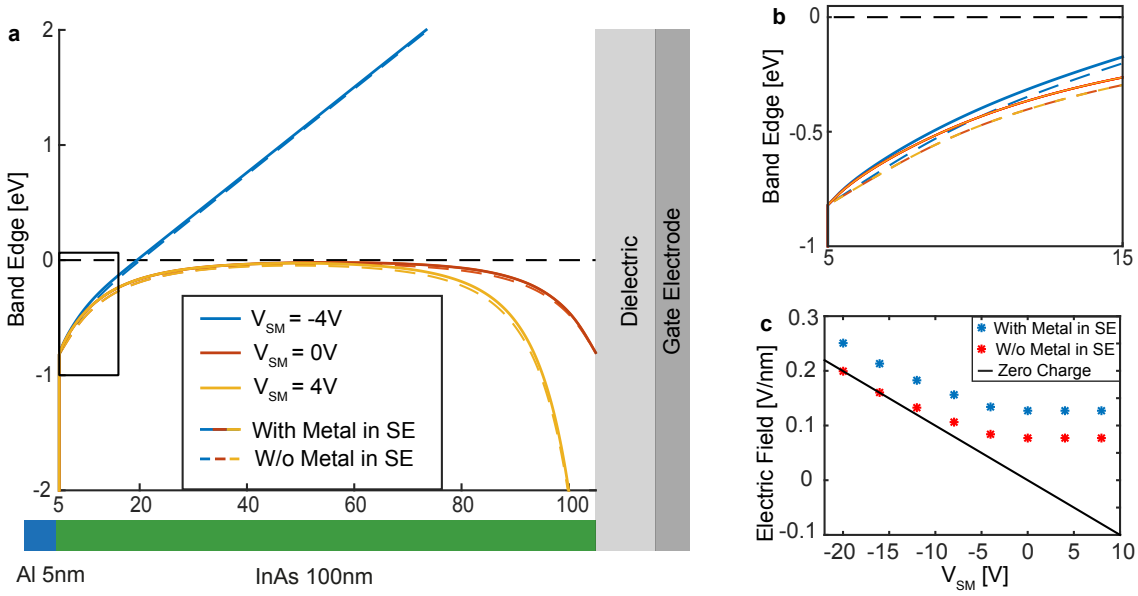

*Figure 4.15: (**a**) Band edge profiles for three different values of V_{SM} obtained from two approaches: Solid lines: Self-consistent solution obtained from the full Schrödinger equation* (4.3).
Dashed lines: Self-consistent solution where the metallic region is neglected in the Schrödinger equation (4.3) *and the wave functions are set to zero at the semiconductor-metal interface.*
*(**b**) Zoom-in at the semiconductor-metal interface. In this case the band edge profiles show some deviation. (**c**) Plot of the electric field at the semiconductor-metal interface corresponding to the band edges on the left. Black line indicates the electric field one would find without electrons in the semiconductor region.*

From Fig. 4.15 (**a**) we see that the band edge profiles for the two approaches are quite similar far from the metallic region while there is some deviation close to the semiconductor-metal

interface as shown in the zoom-in in Fig. 4.15 (**b**). This is also evident in Fig. 4.15 (**c**) which plots the value of the electric field at the semiconductor-metal interface for the two approaches for a wider range of values of V_{SM}. Interestingly we see that the electric fields from the two approaches appear to follow the same trend but with an offset that persists even for large negative values of V_{SM}. For these values the semiconductor region in the simpler approach has been completely depleted of electrons which is evident from the fact that the electric field approaches the zero charge solution of Poisson's equation. Consequently the offset in the electric fields must be due to the excess charge density that is stuck to the semiconductor-metal interface when solving the Schrödinger equation (4.1) in both the Al and InAs region. This is confirmed by Fig. 4.16, which shows the density profiles obtained from the two approaches. Evidently these differ substantially close to the semiconductor-metal interface, which is of course not surprising since in the simpler approach, the density must go to zero at the boundary of the metal.

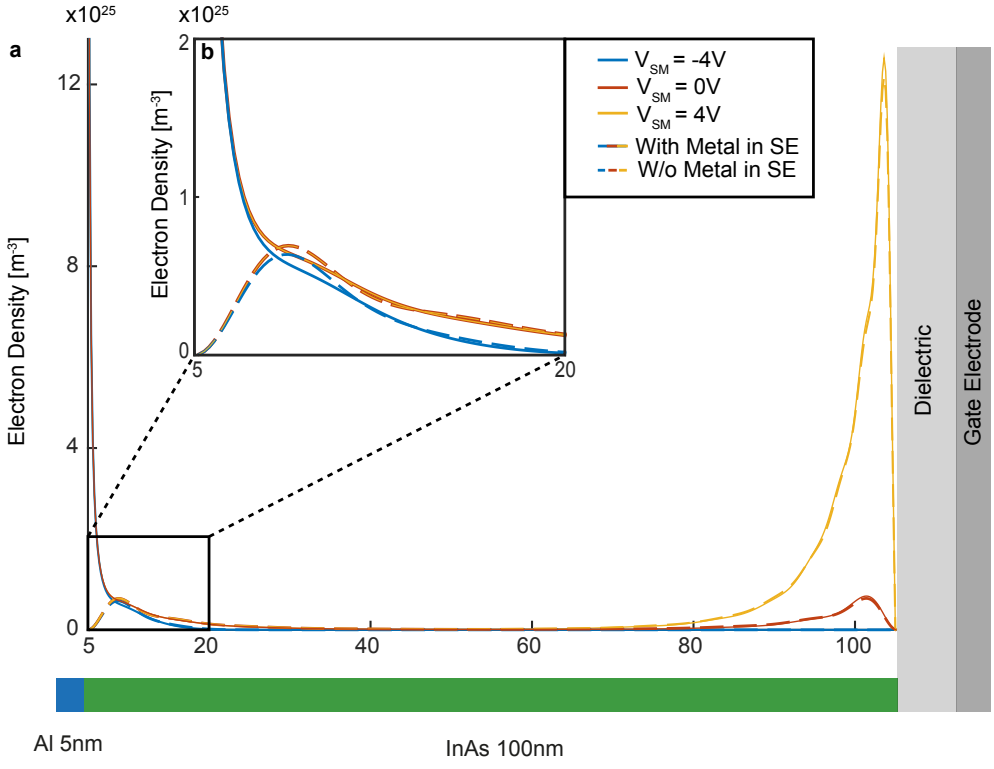

Figure 4.16: Density profiles for three different values of V_{SM} obtained from two approaches: Solid lines: Self-consistent solution obtained from the full Schrödinger equation (4.3). *Dashed lines: Self-consistent solution where the metallic region is neglected in the Schrödinger equation* (4.3) *and the wave functions are set to zero at the semiconductor-metal interface.*

As previously mentioned, the obvious question to ask is how the differences between the two approaches above will influence results such as those of Fig. 4.11, where we investigated the weight of the wave functions in the InAs region. To address this we will focus on the wave function corresponding to the weights indicated by blue in Fig. 4.11 and plot these for different values of V_{SM}. We do this for both the case where the wave function of the hybrid system is solved for using the electrostatic profile from the simpler approach as well as for the case where it is solved for using the electrostatic profile from the approach with hybridization included in the self-consistent calculation.

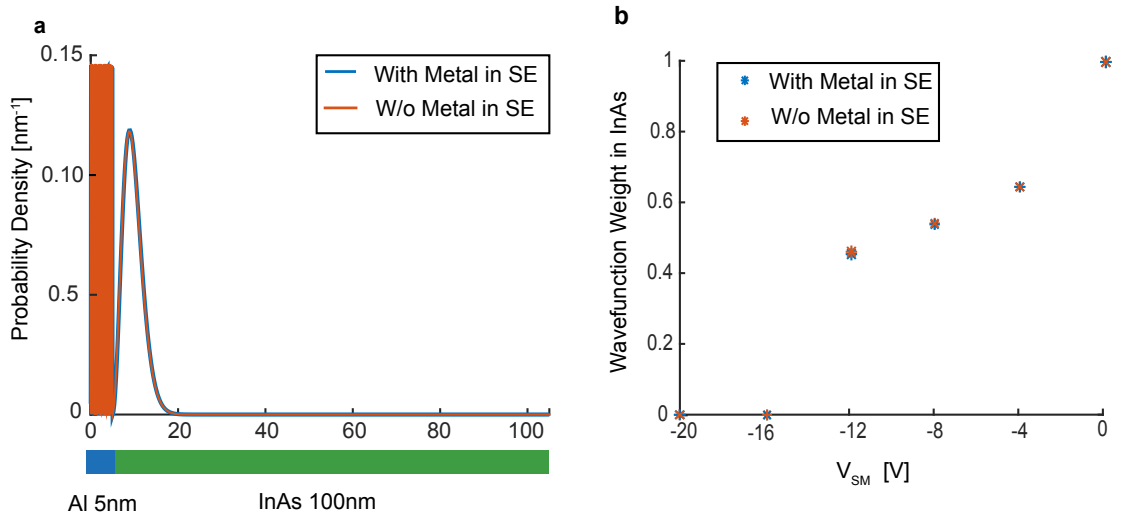

*Figure 4.17: (**a**) Wave functions at $V_{SM} = -4V$ corresponding to the two approaches described above. (**b**) Weight of the wave functions for selected values of V_{SM}. SE is short for Schrödinger Equation.*

Evidently the result of the two approaches produce identical results within numerical uncertainties. If this result is general, which in future should be investigated more carefully, it shows that we can neglect hybdrization effects on the self-consistent calculation of the electrostatic profile. This would be a huge advantage when setting up more complicated models, since including hybdridization effects is very demanding computationally as we will see in the next chapter, where we are forced to neglect these due to limited computational power.

4.3.2 The Thomas-Fermi Approximation and Finite Temperature Effects

As an interesting side note, we will use this section to compare our results with the Thomas-Fermi approximation. The results shown for this approximation were obtained from a Mathematica script written by Karsten Flensberg, University of Copenhagen. Below we briefly address the idea behind the script while details concerned with the numerical solving are neglected.

The central idea of the Thomas-Fermi approximation is to assume that the electrons in the semiconductor may be treated as a homogeneous 3D electron gas with a density given by the standard relation (see for example Chapter 6 of [16])

$$\rho(z) = \frac{-e}{3\pi^2} \cdot \left(\frac{2m^* U_f(z)}{\hbar^2} \right)^{\frac{3}{2}}. \tag{4.14}$$

Here $U_f(z)$ is the local Fermi energy in the semiconductor, which is determined by the offset of the Fermi level and conduction band edge. With our definitions (see Fig. 4.1) we have

$$U_f(z) = \chi_{SM} - W_M + e\phi(z). \tag{4.15}$$

Combining (4.14) and (4.15) with Poisson's equation (4.8) yields the following equation

$$\frac{d^2\phi}{dz^2} = \frac{-e}{3\epsilon\pi^2} \cdot \left(\frac{2m^*(\chi_{SM} - W_M + e\phi(z))}{\hbar^2} \right)^{\frac{3}{2}} \tag{4.16}$$

This is a non-linear differential equation for $\phi(z)$ which may be solved with the boundary conditions (4.12) and (4.9) using numerical techniques. The Thomas-Fermi approximation is thus computationally much easier to handle than the Schrödinger-Poisson approach since the self-consistent problem has been reduced to a single differential equation.
Fig. 4.18 shows a comparison between the band edge profile in the semiconductor obtained from the self-consistent Schrödinger-Poisson method and the Thomas-Fermi approximation for the simple case without a gate electrode and with an InAs layer thickness of 35nm.

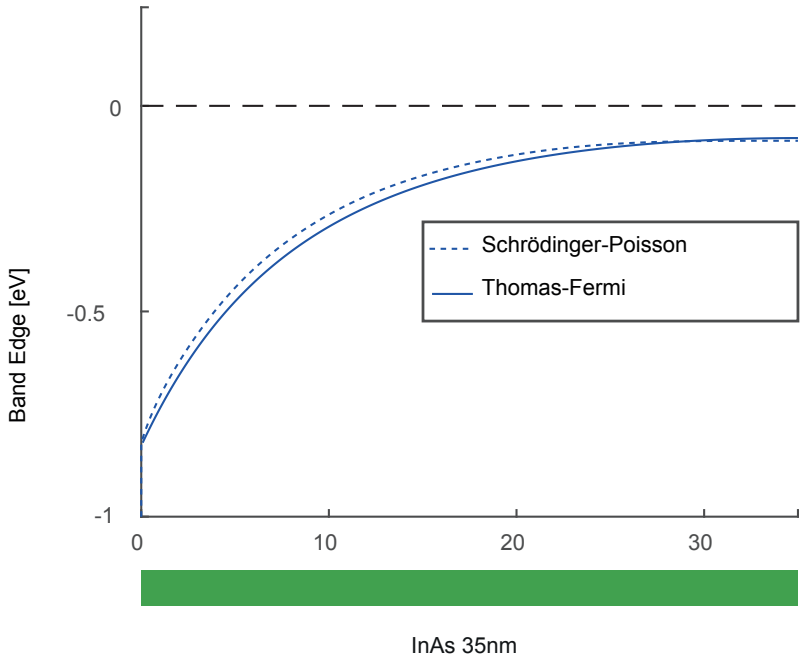

Figure 4.18: Comparison between the band edge profiles in the InAs region obtained from the Schrödinger-Poisson method and the 3D Thomas-Fermi approximation. Here an InAs thickness of 35nm was used.

We see that in this case there is quite good agreement between the result of the two methods indicating that the Thomas-Fermi approximation may be a good approximation for modelling the electrostatics of Majorana devices. In future work this would of course need to be investigated more carefully using a similar approach as in Fig. 4.17, where the eletrostatic profile obtained from the Thomas-Fermi approximation is added to the full Schrödinger equation with hybridization effects similar to the approach discussed for Fig. 4.17.
The simplicity of the Thomas-Fermi approximation also allows us to incorporate finite temperature effects in our system. To do so we again use the assumption of a homogeneous electron gas but now with a charge density in our system given by

$$\rho(z) = \rho_e(z) + \rho_h(z) \tag{4.17}$$

With the electron and hole densities determined by the standard relations (see e.g. Chapter

4 of [19])

$$\rho_e(z) = -e \int_{E_c(z)}^{\infty} D_c(E - E_c(z)) \cdot f(E, \mu)\, dE \quad , \tag{4.18}$$

$$\rho_h(z) = e \int_{-\infty}^{E_v(z)} D_v(E - E_v(z)) \cdot (1 - f(E, \mu))\, dE.. \tag{4.19}$$

Here $\mu = 0$ is the Fermi level in our system and $D_c(E - E_c(z))$ and $D_v(E - E_v(z))$ are the local 3D density of states[19] for the conduction and valence band states with $E_c(z)$ and $E_v(z)$ determined by

$$E_c(z) = W_M - \chi_{SM} - e\phi(z) \tag{4.20}$$

$$E_v(z) = W_M - \chi_{SM} - E_g - e\phi(z). \tag{4.21}$$

Fig. 4.19 shows the results of the Thomas-Fermi approximation for different values of kT given in units of the band gap of InAs, $E_g = 0.43$eV.

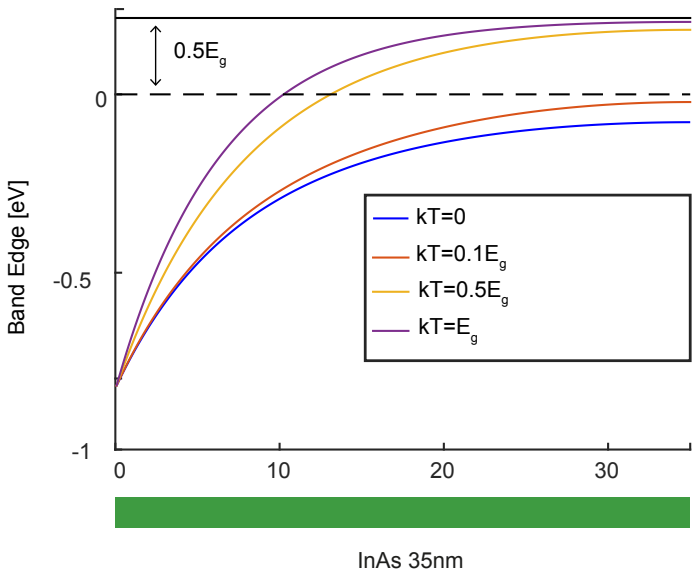

Figure 4.19: Band edge profiles in the InAs region obtained from the Thomas-Fermi approximation with finite temperature excitations included. The band edges shown correspond to different temperatures measured in units of the band gap of InAs. The dashed black line is the Fermi level in the system.

In this case we see that for large temperatures the band edge deviates substantially from the zero temperature solution with the band edge saturating such that the Fermi level is approximately in the middle of the semiconductor band gap. This reflects the conventional

rule of heterojunctions [19], where the Fermi level is assumed to be in the middle of the band gap far from the interface due to thermodynamic equilibrium. On the other hand, for small temperatures compared to the semiconductor band gap, which is the relevant regime for our investigations, the band edge has close resemblance to the zero temperature solution saturating close to the Fermi level of the system. In practice $kT = 0.1E_g$ is already a large temperature. For temperatures that are relevant for experiments on Majorana devices, kT is several orders of magnitude smaller than the semiconductor band gap, and in this case the solutions would be practically indistinguishable from the zero temperature solution.

4.4 Convergence and Other Numerical Aspects

This section is devoted to discussing convergence of the results presented above as well as other important numerical details.

4.4.1 Numerical Parameters

All numerical results of this chapter were obtained using a grid distance of 0.1Å in the metallic region and 1Å in the semiconductor region. These distances were chosen based on the previously discussed criterion that the grid spacing should be significantly smaller than the wavelength of the wave functions used to calculate the electronic density[9]. Furthermore the mixing parameter of the self-consistent calculation was chosen as $\lambda = 0.1$.

4.4.2 Convergence of the Schrödinger-Poisson Method

To address the convergence of our calculations we will take the results without a gate electrode as an example (see Fig. 4.2 and 4.3), though our overall conclusions are general. Fig. 4.20 shows the profile of the electrostatic bending ,$-e\phi$, for selected iterations of the self-consistent calculation.

[9]The Fermi wavelength of Al is quite small $\lambda_F = \frac{2\pi\hbar}{\sqrt{2mE_F}} \approx 3.6$Å, which explains why we choose to use a significantly smaller grid distance in the metallic region.

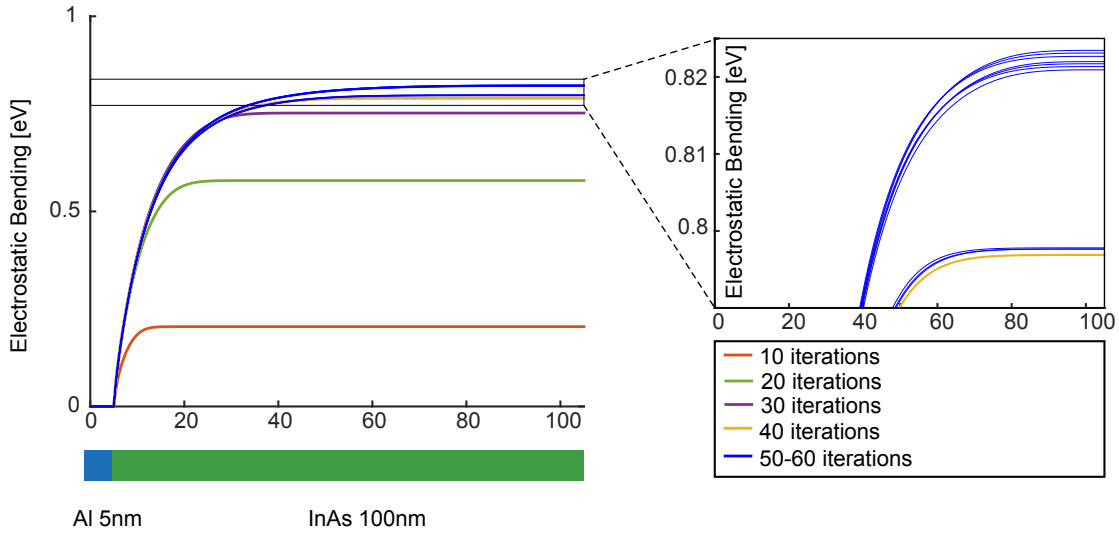

Figure 4.20: Profile of the electrostatic bending $-e\phi$ for selected iterations within the self-consistent calculation of the band edge of Fig. 4.2.

From Fig. 4.20 we see that although the band edge appears to saturate after a certain number of iterations, there are some oscillations in the value at which it saturates. Such oscillations are also found in the corresponding densities which are shown in Fig. 4.21.

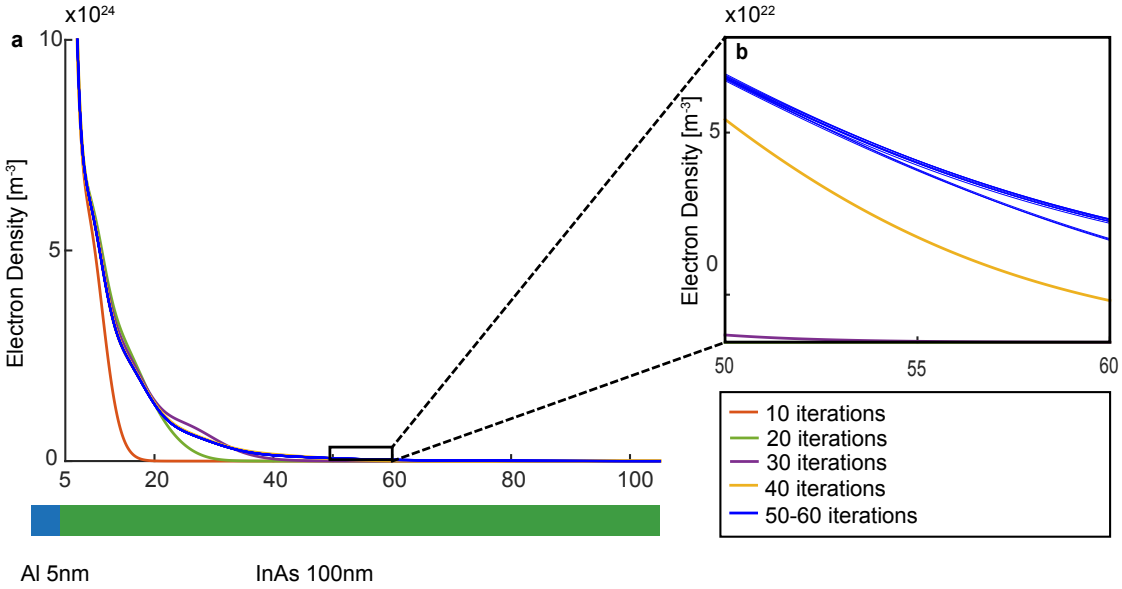

Figure 4.21: Density profiles for the self-consistent calculation described in Fig. 4.20.

For the conclusions of this chapter, these oscillations have little significance since they are small and appear far from the semiconductor-metal interface where the electron density is practically zero. In future work it would however be preferable if such oscillations in the results could be avoided by for example using more advanced mixing schemes such as [33, 34].

4.4.3 Comparison with Analytical Solutions

In this section we compare the numerical solutions obtained from our Schrödinger- and Poisson-solvers to problems where the analytical solution is known. The result of this comparison is shown in Fig. 4.22.

Here Fig. 4.22 (**a**) shows the eigenenergies of (4.3) with $k_{\|} = 0$ and $\phi = 0$ and compares to those obtained by solving the Schrödinger equation analytically by matching boundary conditions and numerically solving the resulting transcendental equation given by

$$\sqrt{\frac{m_1(E-\Delta)}{m_2(E-E_F)}} \cdot \tan\left(\sqrt{2m_1(E-E_F)L_M}\right) = \tan\left(\sqrt{2m_2(E-\Delta)(L_{SM}-L_M)}\right). \quad (4.22)$$

Where m_1 and m_2 denote the effective masses of the metal and semiconductor regions, respectively. Evidently the agreement between our numerical Schrödinger solver and the analytical solutions are good.

Fig. 4.22 (**b**) shows the numerical and analytical solutions of Poisson's equation for a flat charge distribution in the InAs region with density $\rho_0 = 10^5 \mathrm{C}m^{-3}$ for the cases with the boundary condition (4.12) and with the boundary condition that $V_{SM} = 5V$. For these cases the analytical solutions are

$$\phi_1(z) = \frac{\rho_0}{\epsilon}\left(-\frac{1}{2}(z-L_M)^2 + (L_{SM}-L_M)(z-L_M)\right), \quad (4.23)$$

$$\phi_2(z) = \frac{\rho_0}{\epsilon}\left(\frac{(L_{SM}-L_M)(z-L_M)}{2} - \frac{(z-L_M)^2}{2}\right) + V_{SM}\frac{z-L_M}{L_{SM}-L_M}. \quad (4.24)$$

We see that for both solutions the agreement with our numerical solver is good.

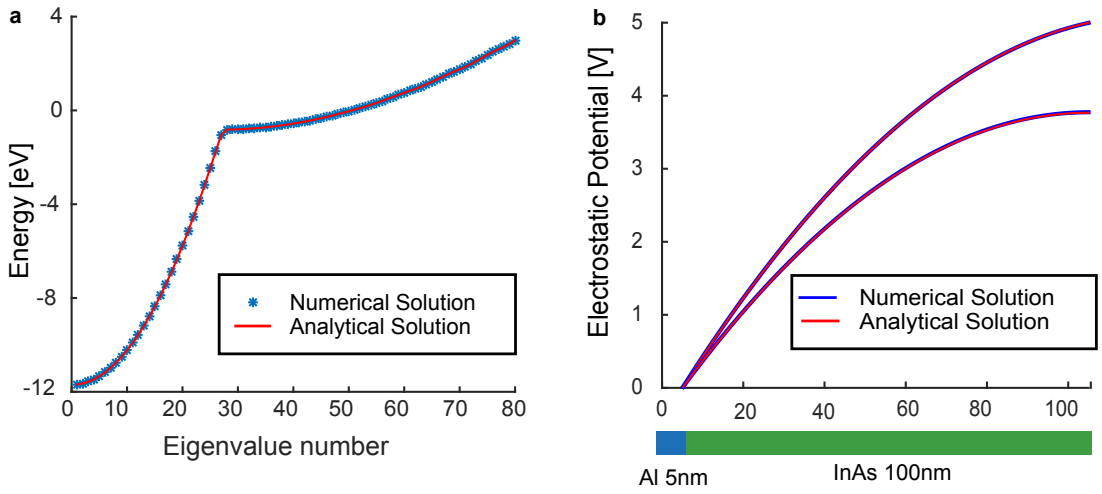

*Figure 4.22: Comparison with analytical solutions. (**a**) Energies of* (4.3) *for* $k_{\|} = 0$ *and* $\phi = 0$ *calculated using our numerical solver (blue stars) and calculated analytically (red line) by matching boundary conditions and solving the resulting transcendental equation numerically. (**b**) Electrostatic potential for flat charge distribution with* $\rho_0 = 10^5 Cm^{-3}$ *obtained using our numerical solver (blue line) and from analytical calculation (red line). The comparison is done both for the solution using the boundary condition of zero derivative at the InAs edge* (4.12) *and with the boundary that* $V_{SM} = 5V$.

4.4.4 The Numerical Integration over $k_{\|}$

We previously argued that it is necessary to integrate over the transverse momentum $k_{\|}$ using (4.7) in order to correctly calculate the density profile in the system. This integration must be performed numerically and is computationally expensive since it requires knowledge of the wave functions for many values of $k_{\|}$, forcing us to solve the Schrödinger equation many times within each iteration of the Schrödinger-Poisson method. For the work in this thesis the simplest possible approach to the problem was taken, where the integration was performed with an equidistant step size in $k_{\|}$. The step size was chosen carefully such that convergence in the density profile was obtained while still providing reasonable computation times. An illustration of the importance of choosing an optimal step size is shown in Fig. 4.23 (**a**), which presents the density profile obtained with three different values of the step size. For the largest step size the density profile is far from converged while the two smallest appear closer to convergence. The computation time for the smaller of these step sizes is 10 times longer than the other indicating the importance of choosing an optimal step size. Another obvious optimization is to use the observation that the wave functions become almost completely localized in the metallic region for large values of $k_{\|}$ as shown in Fig. 4.8. This hints to an approach where, instead of integrating over all values of $k_{\|}$ up to the Fermi level, we only integrate over the first N values of $k_{\|}$, where N should be chosen carefully. Fig. 4.23 (**b**)

shows the density profile in the semiconductor obtained with $\Delta k = 10^{-8}$ by integrating over all values of $k_{\|}$ up to the Fermi level (in this case there were ~ 400 values) as well as from integration over only the first 50 or 100 values. Evidently the integrating over the first 50 values produces a poor result while integrating over the first 100 produces a result which is practically indistinguishable from the full integration.
With all this said, the numerical integration was a very time-consuming part of the numerical model used in this thesis and should there be significantly optimized for future uses.

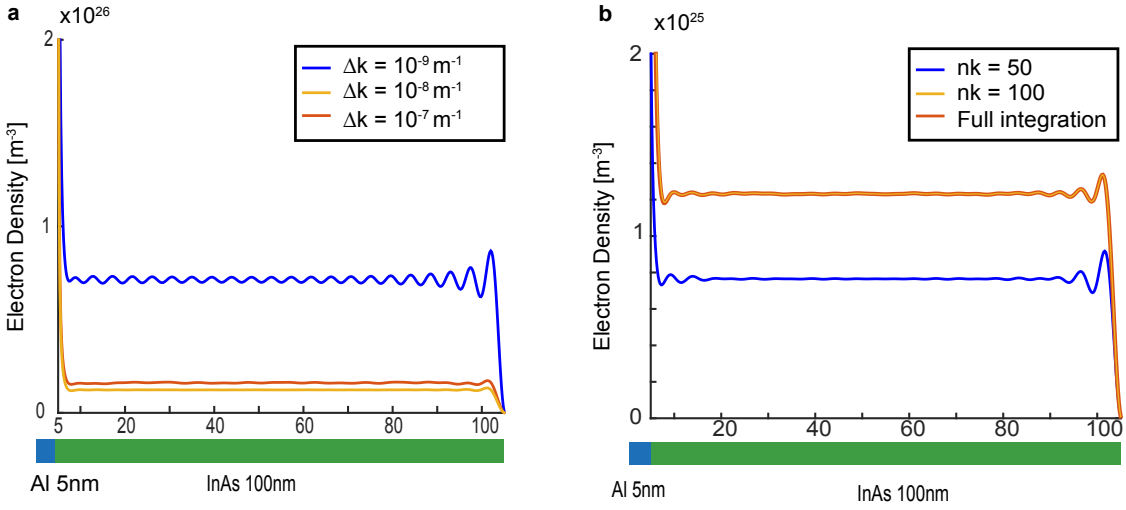

*Figure 4.23: Density profile in the semiconductor region obtained from various approaches to the numerical integration over $k_{\|}$. (**a**) Density profile obtained for three different values of the step size in $k_{\|}$. Evidently the largest step size produces a poor result while the two smaller appear close to convergence. (**b**) Density profile obtained with $\Delta k = 10^{-8}$ by integrating over all values of $k_{\|}$ up to the Fermi level as well as from integration over only the first 50 or 100 values. Evidently integration over the first 50 values produces a poor result while integrating over the first 100 produces a density profile very close to the one obtained from the full integration.*

Chapter 5

The Nanowire Geometry

Having studied the planar geometry, we now turn to the nanowire geometry introduced in Fig. 3.2. While providing a more realistic geometrical description of the Majorana device in Fig. 2 we will see that this model is computationally much more demanding, which notably forces us to neglect hybridization between the semiconductor and superconductor in the system. The results of this chapter will therefore be of more qualitative character than the previous.
It should also be mentioned that the Schrödinger-Poisson problem for this type of structure has already been investigated in the works of [39] and many of the considerations in this chapter are inspired by this reference.

5.1 Setting Up the Schrödinger-Poisson Model

Similar to what we did for the planar structure, we will start by setting up the Schrödinger-Poisson problem for the system. We will see that there are some similarities but also important differences.

5.1.1 The Structure

We consider Fig. 5.1 (**a**) which shows the 2D nanowire geometry that we introduced in Chapter 3. It consists of a 2D cross section of a hexagonal wire, which is partially coated by a metallic superconductor. The nanowire is placed on a dielectric layer contacted to a gate electrode from below, which holds the lower dielectric edge at a voltage V_G with respect to the grounded metallic layer. Finally we have highlighted different surfaces in the system S_M, S_V, S_D, which are where we must specify boundary conditions for Poisson's equation as discussed later.

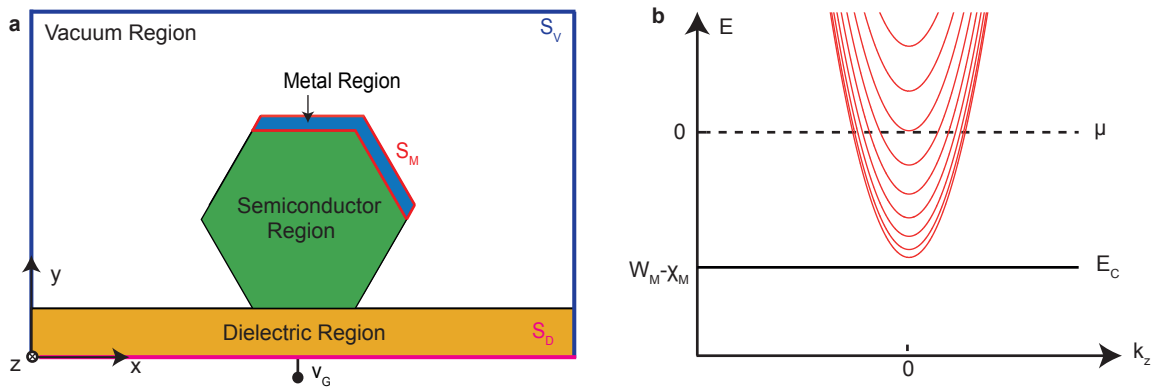

*Figure 5.1: (**a**) The nanowire geometry consisting of a hexagonal nanowire partially coated by a metallic superconductor. The nanowire sits on a dielectric layer which is connected from below to a back gate held at a voltage V_G with respect to the grounded metallic layer. The coloured lines indicate the surfaces S_M, S_V, S_D, which are where we must specify boundary conditions for Poisson's equation. (**b**) Parabolic subbands corresponding to the transverse energy modes inside the wire.*

5.1.2 The Schrödinger Equation

Similar to the planar structure we will assume that the electrons in our system may be described by the Schrödinger equation (3.1). With translational invariance along the wire direction, z, this has the form

$$-\frac{\hbar^2}{2}\boldsymbol{\nabla}\cdot\Big(\frac{1}{m^*(x,y)}\boldsymbol{\nabla}\psi\Big)+\big(E_c(x,y)-e\phi(x,y)\big)\psi=E\psi. \tag{5.1}$$

Where the effective mass, $m^*(x,y)$, conduction band edge, $E_c(x,y)$ and electrostatic potential $\phi(x,y)$ are now dependent on the two transverse directions, x and y.
As before we assume that the Fermi level in our system is set by the metal, which we choose as the reference energy for the band edge $E_c(x,y)$ such that this term is given by

$$E_c(x,y)=\begin{cases}-E_{F,M} & \text{in metal region}\\ W_M-\chi_S & \text{in semiconductor region}\\ W_M-\chi_D & \text{in dielectric region}\\ W_M & \text{in vacuum region}\end{cases} \tag{5.2}$$

with the work function, Fermi energy and electron affinities as defined in Fig. 4.1.
Similar to the planar junction we are interested only in states with energies below the Fermi level such that $E<0<<W_M$, and we may therefore without loss of generality assume that the wave function is zero at the boundaries to vacuum and the dielectric. But while (4.3) was solved both inside the metal and semiconductor region of the planar structure, we will for the nanowire system only solve (5.1) in the green semiconductor region of Fig. 5.1. Furthermore

we will assume that the wave function is zero at the semiconductor-metal interface. With these assumptions the Schrödinger equation (5.1) reduces to

$$-\frac{\hbar^2}{2m^*}\boldsymbol{\nabla}^2\psi - (\Delta + e\phi(x,y))\,\psi = E\psi. \tag{5.3}$$

With m^* being the effective mass of the semiconductor and with the boundary condition that $\psi(x,y) = 0$ at the boundary of the hexagonal nanowire cross section. Furthermore we have defined $\Delta = X_{SM} - W_M$ similar to the previous chapter.
Let us furthermore exploit the translational invariance in the z-direction and insert an ansatz wave function of the form $\psi(\mathbf{r}) = \psi(x,y)e^{ik_z z}$ yielding

$$-\frac{\hbar^2}{2m^*}(\frac{\partial^2\psi}{\partial x^2} + \frac{\partial^2\psi}{\partial y^2}) + \left(\frac{\hbar^2 k_z^2}{2m^*} + \Delta + e\phi(x,y)\right)\psi = E\psi. \tag{5.4}$$

This is the final form of the Schrödinger equation that will be used for our model. It represents a 2D eigenvalue problem, which is computationally much harder to handle than the 1D equation (4.3). On the other hand, the density is more easily computed as we shall see in the next section.
Before moving on let us discuss why we are forced to neglect the coupling to the metal in the Schrödinger equation (5.4). To understand this let us calculate the Fermi wavelength for Al. Using table 1.3 we find

$$\lambda_F = \frac{2\pi\hbar}{\sqrt{2mE_F}} \approx 3.6\text{Å}. \tag{5.5}$$

As discussed in Chapter 3 this means that our grid distance inside the metallic region must be significantly smaller than this value. If we for simplicity assume that we choose a rather coarse grid distance of 1Å this would for a wire diameter of 100nm and a metal layer thickness of 5nm mean that we would need $\sim 50 \cdot 1000$ points in the metallic region alone. This is significantly above the number of points that our simple finite difference method can handle. On top of this comes the fact that we would need to sum over an order of magnitude more wave functions when calculating the density. A rough estimate of this number yields $\frac{5nm \cdot 100nm}{\lambda_F^2} \sim 4000$, which is an extremely large number of wave functions to solve for. In practice sparse matrix methods are only efficient if one needs to calculate a relatively small number of wave functions.

5.1.3 Calculating the Electron Density

Similar to the planar structure we use (2.3) to calculate the electronic density in the system. In this case calculating the density is however a lot easier since the solutions $\psi_n(x,y)$ of (5.4) are independent of k_z and thus degenerate with a parabola of energies belonging to each

solution as shown in Fig. 5.1 (**b**)

$$E_n(k_z) = E_n + \frac{\hbar^2 k_z^2}{2m^*}. \tag{5.6}$$

Where E_n denotes the n'th eigenenergy of (5.4) for $k_z = 0$.
To calculate the electron density we use

$$\rho(x,y) = \frac{-2e}{L_z} \sum_{n, E_n<0} \sum_{k_z} |\psi_n(x,y)|^2 \ , \tag{5.7}$$

where L_z denotes the length of the nanowire in Fig. 5.1. Assuming that this is long compared to the wire diameter[1] we may approximate this sum by an integral to obtain

$$\rho(x,y) \approx -2e \cdot \frac{1}{2\pi} \sum_n \int_{-k_{F,n}}^{k_{F,n}} |\psi_n(x,y)|^2 \ dk_z = \frac{-2e}{\pi} \sum_n |\psi_n(x,y)|^2 \cdot \ k_{F,n} \tag{5.8}$$

Here $k_{F,n}$ denotes the value of k_z at the Fermi level for each subband. Using (5.6) we find

$$k_{F,n} = \frac{\sqrt{2m^*|E_n|}}{\hbar} \tag{5.9}$$

Where the absolute value stems from the fact that the occupied states in the system have negative energies (see Fig. 5.1 (**b**)). Inserting the above in (5.8) yields

$$\rho(x,y) = -e \sum_n \frac{\sqrt{8m^*|E_n|}}{\pi\hbar} \ |\psi_n(x,y)|^2. \tag{5.10}$$

Which is the central formula for calculating the electron density in the system.

5.1.4 Poisson's Equation

Let us now turn to Poisson's equation (2.5). In our case translational invariance along the z-direction reduces this equation to a 2D equation on the form[2]

$$\frac{\partial}{\partial x}\left(\epsilon_r(x,y)\frac{\partial \phi}{\partial x}\right) + \frac{\partial}{\partial y}\left(\epsilon_r(x,y)\frac{\partial \phi}{\partial y}\right) = -\frac{-e\rho(x,y)}{\epsilon_0}. \tag{5.11}$$

This equation should be solved in both the dielectric, semiconductor and vacuum region indicated in Fig. 5.1 (**a**), though the charge density is non-zero only in the semiconductor region. It remains now to specify the boundary conditions for (5.11).

[1] This is a feasible approximation since the lengths of the nanowires used for Majorana devices are typically on the order of several μm while the wire diameters are $\sim 100nm$. This is for example the case for the device shown in Fig. 2.

[2] This is on the same form as the Poisson equation (2.17) discussed in the chapter on the numerical details.

For the first boundary condition we have the standard requirement (2.10) that the electrostatic potential goes to a constant at the surface S_M of the metallic layer as shown in red in Fig. 5.1. Choosing this as the reference value for the electrostatic potential we thus require

$$\phi(x,y)\Big|_{S_M} = 0. \tag{5.12}$$

The second boundary condition is determined by the gate electrode, which sits on the lower surface, S_D, of the dielectric layer as indicated in purple in Fig. 5.1. In this case we require that

$$\phi(x,y)\Big|_{S_D} = V_G. \tag{5.13}$$

Finally we must specify the boundary condition on the surface S_V indicated in Fig. 5.1 (**a**). In this case we require that the electric field perpendicular to the surface vanishes such that

$$-\boldsymbol{\nabla}\phi\Big|_{S_V} = 0. \tag{5.14}$$

The physical motivation for this boundary condition is the fact that the field vanishes far away from an infinite line charge. This is essentially the problem that we are studying, since we have assumed translational invariance along the nanowire. The idea is then that we can make the vacuum region large enough to mimic an infinite box. This is obviously bound to fail close to the gate electrode, where the electrostatic potential must fullfill (5.13). Fortunately we will see that the exact boundary condition at the vacuum edge has almost no influence on the electrostatic profile inside the nanowire region, which therefore allows us to use (5.14).

5.2 Results

We are now ready to proceed with discovering the different results that may be obtained from our model. As in the previous chapter we will begin with some basic results and then move on to a more systematic investigation of various phenomena.

The simulations presented in this chapter were obtained for an InAs nanowire with diameter 100nm covered by a 5nm Al layer as shown in Fig. 5.1. The dielectric layer was chosen to be SiO_2 with a thickness of 10nm. The values for the work function and Fermi energy of Al, electron affinity of InAs as well as the various dielectric constants were taken from the tabulated values shown in tables 1.2, 1.3 and 2.1. Similar to the previous chapter these values yield an offset of $\Delta = 0.82$eV between the InAs conduction band and Fermi level of Al. Altogether these values above defines our standard choice of parameters for the simulations below and were used unless anything else is specified.

5.2.1 Introductory Results

As an introduction let us consider the result of a self-consistent calculation of the electrostatic profile in our system for the standard choice of parameters. The result of such a calculation is shown in Fig. 5.2 for the case where the gate voltage is set to 0V.

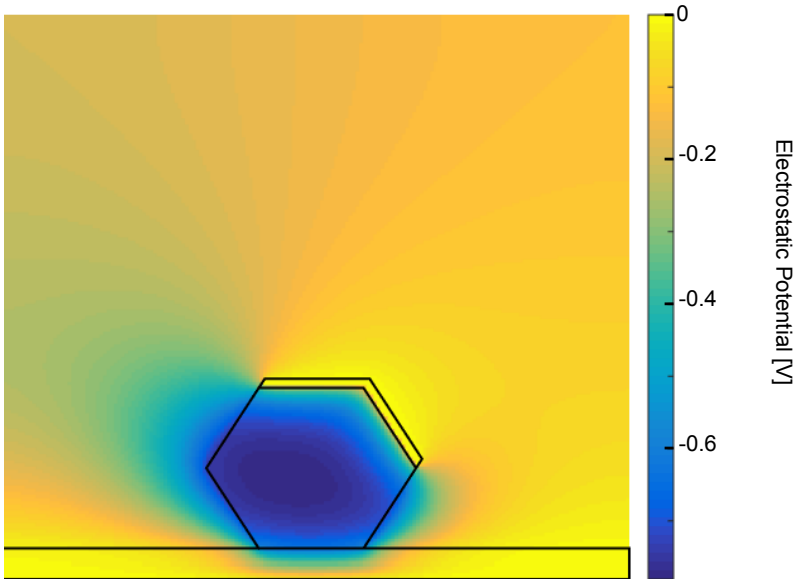

Figure 5.2: Self-consistent calculation of the electrostatic potential in the nanowire geometry. The most drastic changes in the electrostatic potential happen close to the metal layer and gate electrode, where the electrostatic potential must increase to satisfy the required boundary conditions.

For the behaviour of the electrostatic potential it is clear that this is mainly interesting inside the nanowire region, where there is a finite charge density. In this region we see that the most drastic changes happen close to the edge of the metal layer, where the electrostatic potential rises sharply to match the boundary condition set at this edge. The same thing happens as we approach the gate electrode, since in this case the boundary condition at the two edges are the same. However, in the latter case we see that the changes in the electrostatic potential happen also inside the dielectric layer which thus acts as a buffer layer, suppressing the influence of the gate electrode[3].

Since the electrostatic interaction felt by the electrons in the wire is given by $-e\phi$ the behaviour observed in Fig. 5.2 is essentially the same that we found for the gated planar structure in

[3] In general, the stronger the dielectric, the less is the suppresion of the gate electrode. We have used SiO_2 for our simulations, which is a relatively weak dielectric and thus supresses the influence of the gate electrode significantly.

Fig. 4.5, where the electrostatic potential had the effect of creating wells at the edges of the semiconductor. One would therefore expect that the effect of the electrostatic interaction is a localization of the electron density to the edge of the metallic layer as well as a weaker localization at the edge of the dielectric. To confirm this suspicion we consider Fig. 5.3, which shows the electron density profile obtained self-consistently as well as the profile obtained without electrostatic interaction for comparison.

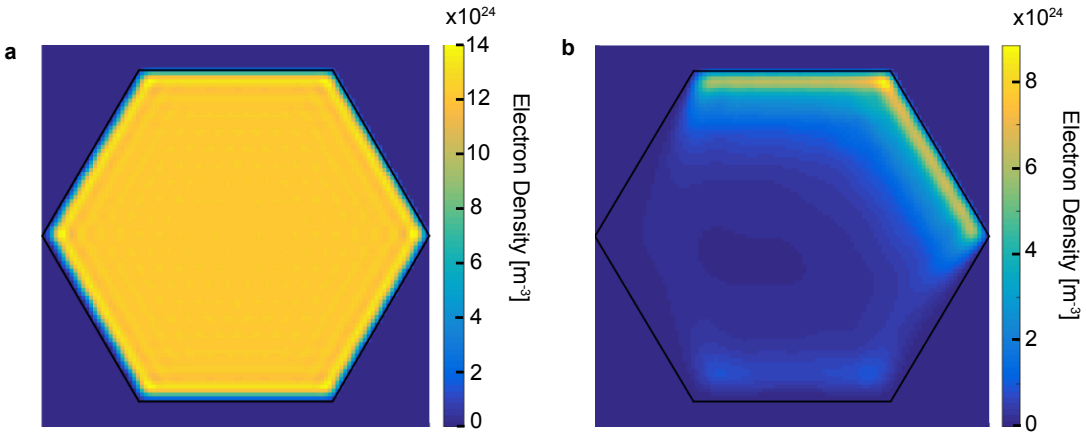

*Figure 5.3: Result of self-consistent calculation of the density profile in an InAs-Al nanowire with the standard choice of parameters. (**a**) Electron density profile obtained without including electrostatic interaction. In this case the density profile is homogenous with slight oscillations at the edges, where the wave functions must go to zero. (**b**) Electron density profile obtained from the self-consistent Schrödinger-Poisson method. In this case the electron density is mainly localized at the metallic edge but also with some localization at the semiconductor-dielectric interface. This is exactly what one would expect from the electrostatic profile in Fig. 5.2.*

Comparing Fig. 5.3 (**a**) and (**b**) we see that the effect of the electrostatic interaction is indeed a strong localization of the electron density at the edge of the superconductor as well as a weaker localization at the dielectric edge.

Having shown the profile of the electron density in the nanowire it is only natural to address the form of the eigenstates that contribute to this density. We will here focus on the first four occupied states[4] which are shown in Fig. 5.4 along with the ones obtained without electrostatic interaction for comparison.

[4]We focus on the lowest modes since these contribute most significantly to the electron density in the wire. Later we will address the dependence of the number of occupied subbands in our system on various parameters.

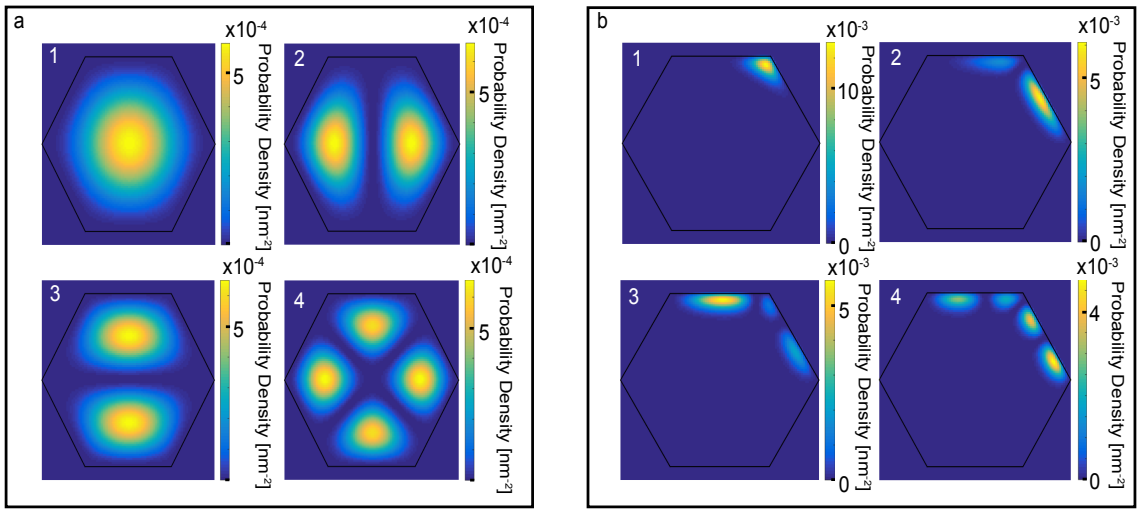

*Figure 5.4: Probability density of the first four eigenstates in our system. (**a**) Eigenstates without electrostatic interaction. In this case the wave functions have close resemblance to the commen eigenstates of L_z and L_z^2. (**b**) Eigenstates obtained from the self-consistent Schrödinger-Poisson method. In this case the wave functions are localized close to the metallic interface, which is in good agreement with the behaviour observed in Fig. 5.2.*

For the wave functions without electrostatic interaction, we see that these have close resemblance to the ones obtained from solving the Schrödinger equation in a circular well[5] with a slight warping due to the hexagonal geometry. Comparing to the self-consistent ones the effect of the electrostatic interaction is evidently a strong localization of the wave functions at the metal interface, which is of course just what we expect from our discussion of the density and electrostatic profile above[6].

5.2.2 Effects of the Gate Electrode

Let us now investigate what happens as we change the value of the gate voltage to negative or positive values. We focus first on the case of a positive value of V_g. Fig. 5.5 shows the results of a self-consistent calculation for $V_G = 10V$ with the standard choice of parameters.

[5]For a treatment of the Schrödinger equation for the circular well see [40]. The eigenstates are essentially the common eigenfunctions of L_z^2 and L_z with the energies depending on m^2, where m denotes the quantum number belonging to L_z. The states are thus two-fold degenerate except for the non-degenerate ground state. This is also reflected in the form of the wave functions in Fig. 5.4 (**a**) with the second and third representing a degenerate pair.

[6]The weak localization of the electron density at the dielectric interface happens for higher energy modes, which have sufficient energy to overcome the electrostatic barrier in the middle of the nanowire.

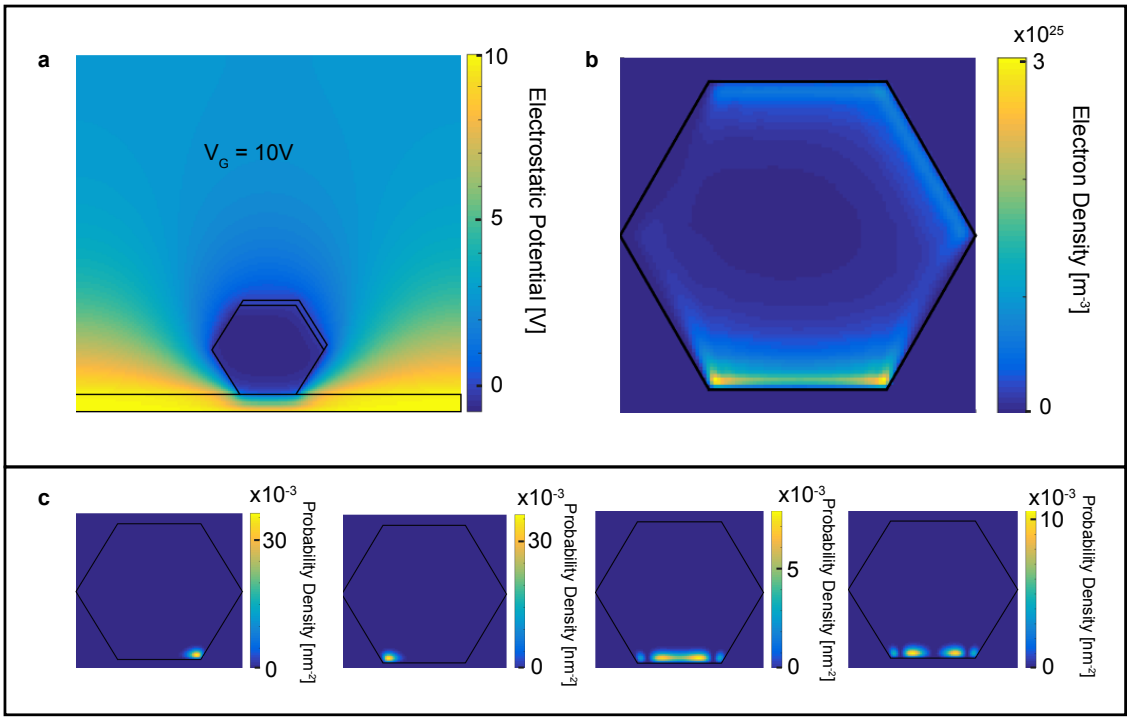

*Figure 5.5: Overview of a self-consistent calculation for $V_G = 10V$. (**a**) Electrostatic profile in the system. In this case the gate forces the electrostatic potential to be larger at the dielectric edge. (**b**) Density profile in the nanowire. In this case the positive gate voltage has shifted the profile of the electron density towards the dielectric interface. There is however still some localization of the density at the metal edge. (**c**) Probability density of the first four eigenmodes obtained from the self-consistent solution. In this case the wave functions are localized at the dielectric edge.*

From Fig. 5.5 we see that the effects of a positive gate voltage is that the density profile now becomes peaked at the bottom of the nanowire. A closer inspection of Fig. 5.5 however also shows that there is a significant density concentrated at the metal interface. The behaviour of the density profile in Fig. 5.5 is thus essentially the same as the one we observed for the gated planar structure in Fig. 4.7, where even high positive gate voltages could not deplete the electron density close to the metal interface.

We next focus on the case of a negative gate voltage. Fig. 5.6 shows the results of a self-consistent calculation for $V_G = -10V$ with the standard choice of parameters. In this case the gate electrode repels the electrons in the nanowire, which has the effect that the electron density becomes even more confined to the metal interface compared to the situation in Fig 5.3.

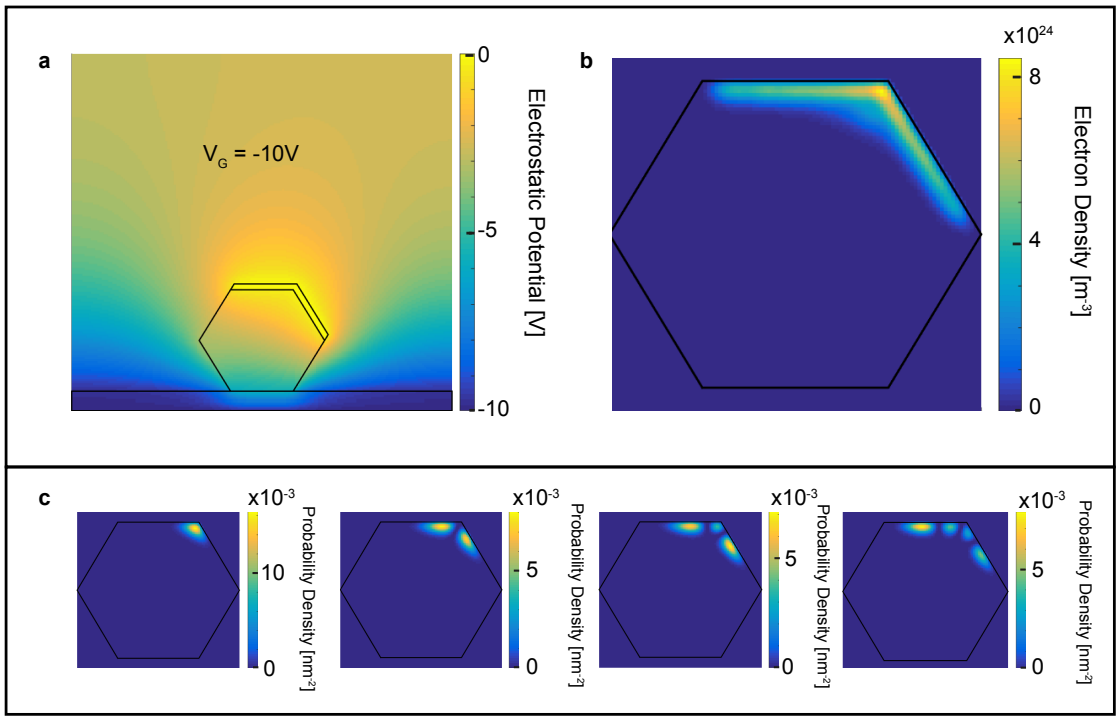

*Figure 5.6: Overview of a self-consistent calculation for $V_G = -10V$. (**a**) Electrostatic profile in the system. In this case the gate repels the electrons thereby pushing them closer to the metal edge. (**b**) Density profile in the nanowire. In this case the negative gate voltage has shifted the profile of the electron density towards the edge of the metallic layer. (**c**) Probability density of the first four eigenmodes obtained from the self-consistent solution. In this case the wave functions are strongly localized at the metallic edge.*

The observations above were based on specific values chosen for the gate voltage. It is of course preferable to have a more general understanding of the effects of the gate voltage on various physical quantities. A step towards this is shown in Fig. 5.7, where we plot the number of occupied wave functions and the evolution of the five lowest subband energies in our system as a function of V_G.

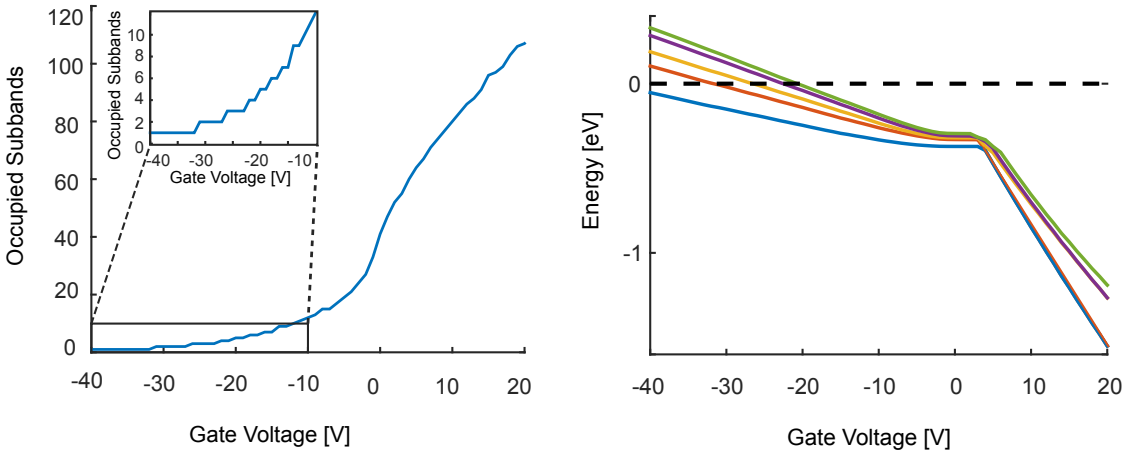

*Figure 5.7: (**a**) Number of occupied modes vs gate voltage with a zoom-in around the negative gate voltages. For very negative gate voltages the wire is almost completely depleted with only one occupied mode. As we approach larger gate voltages more modes start to get populated with increasing speed. (**b**) Evolution of the five lowest subband energies as a function of gate voltage.*

From Fig. 5.7 (**a**) we see that as we increase the gate voltage from negative towards positive values the number of occupied subbands starts to rise, which is of course expected from our earlier observations. What is more interesting is the character of this increase, since we note a clear growth in the steepness. For the subband energies in Fig. 5.7 (**b**) we see a matching behaviour. These first decrease slowly and then suddenly start to decrease drastically at positive gate voltages. This behaviour may be understood from our observations of the fact that the electrostatic interaction tends to create electrostatic well at the edges of the metal and dielectric layer in our system. At large negative gate voltages only the electrostatic well at the metal interface is present and consequently this determines the behaviour of the wave functions and energies in our system. As we then approach positive gate voltages the electrostatic well at the dielectric interface begins to emerge and the sudden change in the subband energies of Fig. 5.7 marks a transition, where the lowest energy states in the system go from being localized at the metallic edge to the dielectric edge.

Let us also comment on the values of the gate voltages in Fig. 5.7. As explained in the introduction of this thesis, the ideal Majorana experiments happen in a regime with few occupied transverse modes in the wire, which is achieved by tuning the gate voltages of the experiment to negative values. Comparing to our numerical simulation in Fig. 5.7 we see that to achieve such a regime, large negative gate voltages must be used, which are significantly more negative than the typical ones used in the experiments [10, 14]. While the reason for this deviation is not known, a likely explanation could be that we are using too large a value for

the offset between the work function and electron affinity, Δ. We will address this in greater detail, when we later vary the value of this parameter.

5.2.3 Alternative Geometries

So far all the results of this chapter were based on the geometry shown in Fig. 5.1. As an interesting side note, we will use this section to demonstrate that our model may also be used to simulate geometries with different placements of the superconducting layer. Such an investigation is especially interesting because the deposition of the superconducting layer on devices such as the one in Fig. 2 is a highly controlled experimental process [12], which thus allows for engineering Majorana devices with many variations in the design.
Fig. 5.8 shows the electrostatic profile and electron density in the system for three alternative geometries which are relevant for current experiments on Majorana devices [12, 15]. The simulations were done using $V_G = 0$.

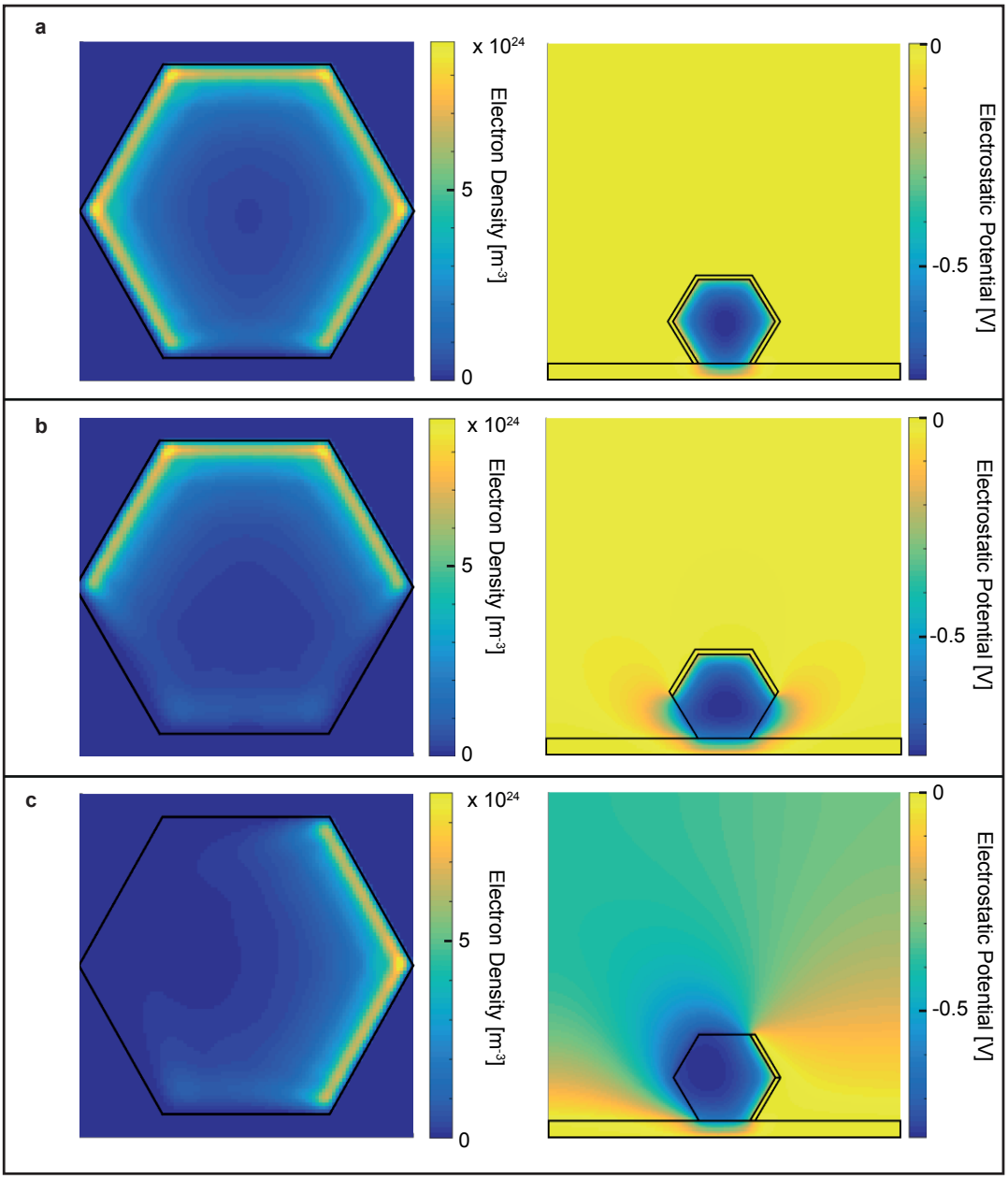

*Figure 5.8: (**a**) Self-consistent calculation of the electrostatic profile and electron density for a wire with five facets covered by a metallic superconductor. (**b**) Self-consistent calculation of the electrostatic profile and electron density for a wire with the upper three facets covered by a metallic superconductor. (**c**) Self-consistent calculation of the electrostatic profile and electron density for a wire with the two side-facets covered by a metallic superconductor.*

Combining results such as the above with more detailed microscopic models including for example effects of spin-orbit coupling [41, 42] could be interesting for future work. For now we will restrict ourselves to studying qualitative differences between the efficiency of the gate electrode for the different geometries of Fig. 5.8. By efficiency we here mean its ability to deplete the wires in Fig. 5.8 of transverse subbands. The result of such an investigation is shown in Fig. 5.9, where we have also included the original geometry of Fig. 5.1.

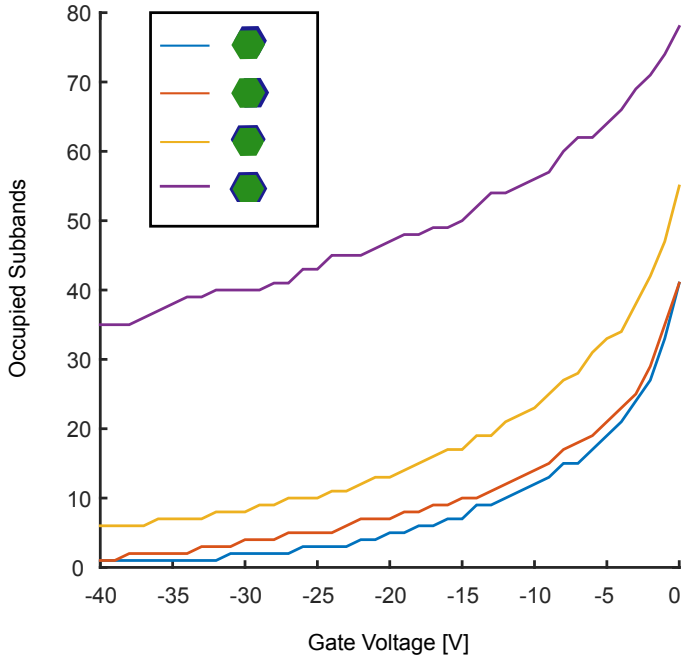

Figure 5.9: Number of occupied subbands in the wire as a function of V_G for different placements of the superconductor.

From Fig. 5.9 we see that the gate is far less effective for the nanowire, where the superconductor covers five facets, which is physically expected since in this case the metallic layer screens the influence of the gate electrode the most. Evidently the geometry which is least affected by the screening from the superconductor is the original geometry of Fig. 5.1.

5.2.4 Varying the Value of Δ

So far all the results of this chapter were obtained for our standard choice of parameters as described in the beginning of the results section. Notably this means that a value of $\Delta = 0.82$eV was used for the offset between the work function of the superconductor and electron affinity of the semiconductor.

In this section we discuss the consequences of using different values for this offset. The result

of such an investigation is shown in Fig. 5.10 (**a**), which shows the number of occupied subbands in the wire as a function of V_G for different values of Δ.

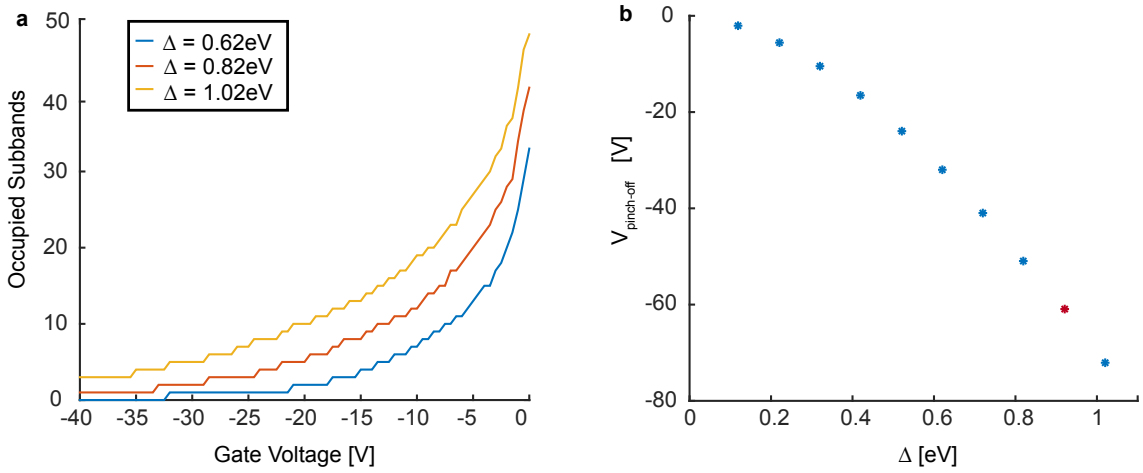

*Figure 5.10: (**a**) Number of occupied subbands in the wire as a function of V_G and for different values of Δ. (**b**) Pinch-off voltage of the wire as a function of Δ. The magenta point corresponds to the value of Δ that was used for the simulations in this chapter.*

Similar to the results obtained for the planar junction, we see that Δ has significant influence on the results obtained from our model, and future work would therefore require a more detailed approach, where our simulation results are compared to experiments in order to extract a reasonable value of this parameter. However, as previously discussed, this value is likely to depend on surface chemical properties, which could fluctuate from experiment to experiment.

Let us also address the previously noted observation, that the gate voltages used in our simulations appear to deviate substantially from the values used in the real experiments on Majorana zero modes [14, 15]. Such values obviously depend on the thickness and quality of the dielectric layer used in the actual experiments and are therefore not readily comparable to our simulations. Even with this in mind, the large negative values of V_G of Fig. 5.7 needed for depleting the wire of subbands still seem suspiciously far from the experimental reality. The point is, however, that these values will also be very sensitive to the value of Δ. This point is illustrated in Fig. 5.10 (**b**), which plots the gate voltage needed for depleting the wire of subbands, the so-called pinch-off voltage, for different values of Δ.

5.3 Convergence and other Numerical Aspects

This concludes the results obtained for the 2D geometry. Similar to the previous chapter, we will now address the convergence of our model as well as the effect of the boundary condition at the vacuum edge (5.14).

5.3.1 Numerical Parameters

All the numerical results of this section were performed with a uniform grid spacing of 0.8nm in the entire geometry of Fig. 5.1. It is clear that this could be greatly optimized for future work by for example using a non-uniform grid distance. This is especially a relevant point, since the wave functions with electrostatic interaction (Fig. 5.5, 5.6 and 5.4) are confined to very narrow regions, where one should therefore optimally use a finer mesh size compared to the rest of the geometry.
For achieving the self-consistent solution the mixing parameter of (2.27) was chosen as $\lambda = 0.1$.

5.3.2 Convergence of the Schrödinger-Poisson Method

In general the simulations for the 2D nanowire geometry showed smooth convergence without substantial oscillations like those found for the planar structure. The results also appeared stable to changing the electrostatic potential used as the initial input. This indicates that the results of this chapter reflect the true self-consistent solutions of the Schrödinger-Poisson problem and are not just artifacts of a local minimum in the iteration process. Fig. 5.11 shows the error in the electrostatic potential and electron density in the system for the case with $V_G = 0$ as a function of the number of self-consistent iterations. Here we have cut out the first points of the iterations process, since the errors of these would overshadow the error of the remaining iterations. The error of the i'th iteration was calculated as $\max(\boldsymbol{\phi}_i - \boldsymbol{\phi}_{i-1})$ and $\max(\boldsymbol{\rho}_i - \boldsymbol{\rho}_{i-1})$, where max() denotes the maximum value of the vectors. Evidently both physical quantities appear to converge.

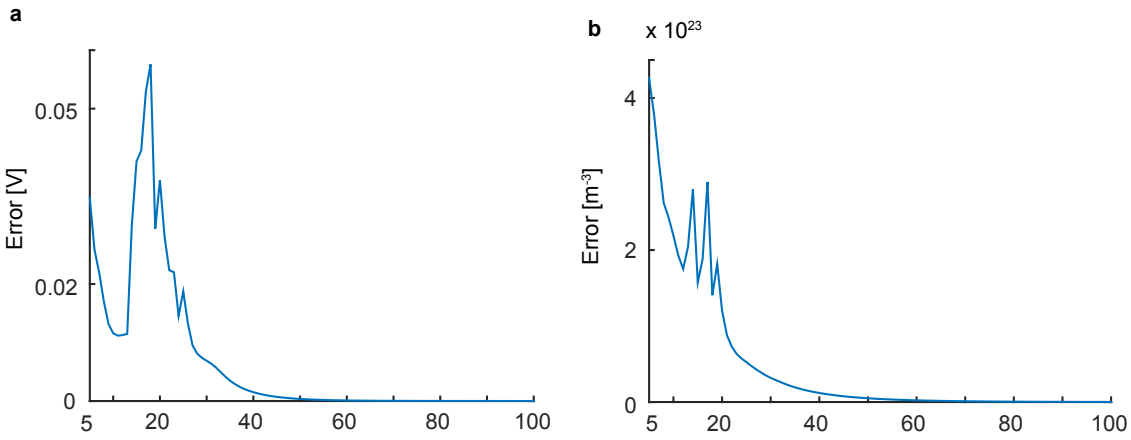

*Figure 5.11: (**a**) Error in the electrostatic profile of our system as a function of the number of self-consistent iterations. (**b**) Error in the electron density profile in our system as a function of the number of self-consistent iterations.*

5.3.3 The Boundary Condition at the Vacuum Edge

When setting up our model we argued that the physical validity of the boundary condition (5.14) used on the surface S_V of Fig. 5.1 is bound to break down close to the gate electrode. In this section we show that this boundary condition has little influence on the physical results obtained from our model. To do so we consider Fig. 5.12, which shows a self-consistent calculation of the electrostatic potential with $V_G = 0$ for three different scenarios. For (**a**) the boundary condition (5.14) was used and a large vacuum region around the wire was included. For (**b**) the boundary condition (5.14) was likewise used but for this simulation the vacuum region was made substantially smaller. For (**c**) a different boundary condition was used, where the electrostatic potential was set to zero on the vacuum edge.

As previously discussed, it is the electrostatic profile inside the wire, which is relevant for our conclusions, since this is where we have a finite charge density. From inspection of Fig. 5.12 it is evident that the boundary condition on the vacuum edge has very little influence on this. This is further illustrated in Fig. 5.12 (**d**) and (**e**), where the absolute value of the difference between the electrostatic profile of 5.12 (**a**) and (**b**) and 5.12 (**a**) and (**c**) is plotted.

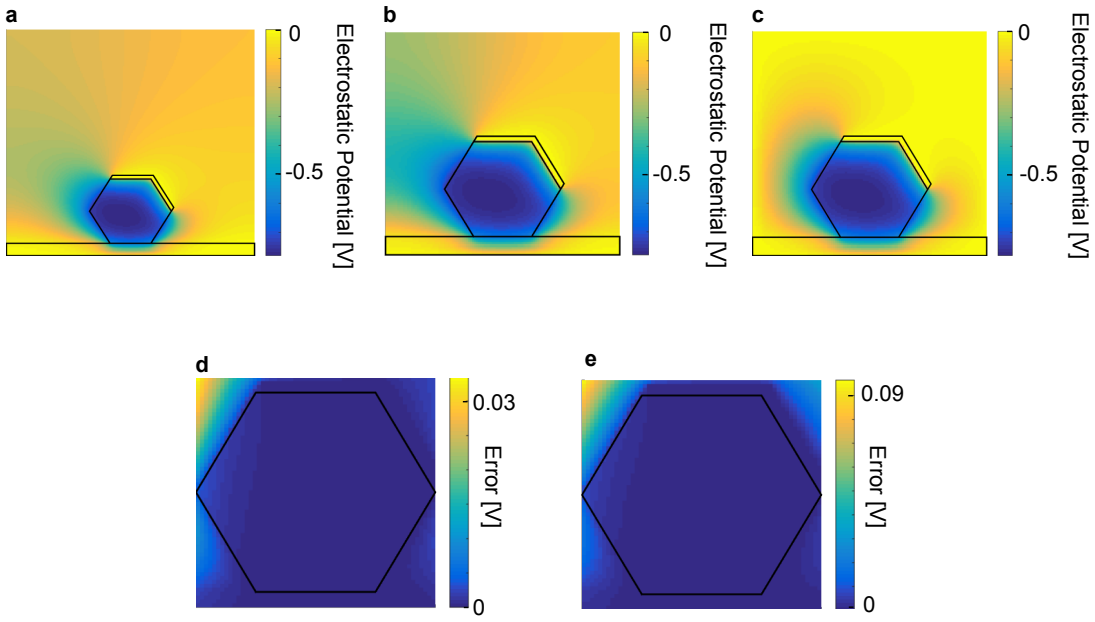

*Figure 5.12: (**a**) Electrostatic profile obtained for a wire with a large vacuum region and using the boundary condition* (5.14)*. (**b**) Electrostatic profile obtained for a wire with a small vacuum region and using the boundary condition* (5.14)*. (**c**) Electrostatic profile obtained for a wire with a small vacuum region and using the boundary condition that $\phi(x, y) = 0$ on the boundary S_V shown in figure 5.1. (**d**) Absolute value of the difference in the electrostatic profile in the wire region between **b** and **a**. (**e**) Absolute value of the difference in the electrostatic profile in the wire region between **c** and **a**.*

Chapter 6

Conclusions and Outlook

In this thesis a simulation model based on the Schrödinger-Poisson method was developed and applied to two geometries inspired by experimental setups used for realizing Majorana zero modes.

The first geometry was a planar semiconductor-metal heterostructure in contact to a gate and dielectric. The structure was assumed translationally invariant in two directions. We showed how to set up the Schrödinger-Poisson problem and notably included hybridization between the semiconductor and metal in the Schrödinger equation. We then presented simulation results based on an InAs-Al junction both for the case with and without contact to a gate and dielectric. Our most important finding was that the electrostatic interaction creates wells at the semiconductor-metal interface as well as at the semiconductor-dielectric interface for positive gate voltages. Our results were then compared to a simpler approach, where the Schrödinger equation was solved only in the semiconductor region. We found that the two approaches produced comparable results with some deviation in the electron density and electrostatic profile at the semiconductor-metal interface. We investigated the differences between using the electrostatic profiles from the two approaches when solving for the wave functions in the hybrid system and found that they were negligible with our parameters. The validity of this conclusion should however be more systematically investigated in future work.

Since the ultimate goal of our work is to understand electrostatic effects on details related to the formation of Majorana zero modes, the next big step will be to combine our description of the electrostatic environment with a more detailed microscopic model. Doing so it will be natural to investigate whether the deviations found between solving the self-consistent problem with and without hybridization are significant for the outcome of the microscopic description. If they turn out not be, which has been made plausible in Section 4.3.1, it will be a significant result, since including hybridization in the Schrödinger-Poisson method is computationally demanding and not a viable approach for more complicated structures such

as the nanowire geometry investigated in Chapter 5.

Another point that must be adressed is the strong dependence of our results on the offset between the work function of the metal and electron affinity of the semiconductor. This dependence is problematic, since the values of these parameters are not known with certainty. A future important task will therefore be to determine more carefully how our conclusions depend on these parameters and ultimately to compare with experimental data to determine more realistic values.

The second geometry was a 2D cross section of a hexagonal nanowire with translational invariance in the longitudinal direction. The wire was placed on a dielectric layer contacted to a gate electrode and covered by a metallic superconductor on two of its facets.

We showed how to set up the Schrödinger-Poisson model but argued that including hybridization between the metal and semiconductor was too computationally demanding. Results were presented based on an InAs nanowire with Al as the superconductor. We found, similar to the planar geometry, that the electrostatic interaction had the effect of creating a well at the semiconductor-metal interface and one at the semiconductor-dielectric interface for positive gate voltages. We then investigated the dependence of the number of occupied subbands on the gate voltage and found large numbers compared to experiments. We argued that this discrepancy could be due to the applicance of too large a value for the offset between the work function of the metal and electron affinity of the semiconductor.

For future work it is clear that the first task will be to heavily optimize our numerical model. Most importantly this would mean developing a more advanced method for varying the grid spacing in our geometry, making it more dense close to the metallic region as well as other locations, where the density and electrostatic profile varies significantly.

Once this has been achieved, the next big step would be to combine our description of the electrostatic environment with a more detailed model including the microscopic components needed for the describing Majorana zero modes. Here we are however restricted by the fact that we cannot describe the hybridization between the metal and semiconductor regions due to limited computational power. The ultimate approach would therefore be to combine our efforts and use the simpler planar geometry for investigating the effects of the semiconductor-metal hybridization on the electrostatic profile. Once this has been completely understood the next challenge will be to combine the conclusions from this investigation with our model of the 2D nanowire geometry.

Altogether, this thesis has laid the first stepping stones towards a full electrostatic description of Majorana devices. A description of such will hopefully prove valuable to the current worldwide efforts of realizing a universal quantum computer.

Bibliography

[1] Chetan Nayak, Steven H. Simon, Ady Stern, Michael Freedman, and Sankar Das Sarma. Non-abelian anyons and topological quantum computation. *Rev. Mod. Phys.*, 80:1083–1159, Sep 2008.

[2] S. Das Sarma, M. Freedman, and C. Nayak. Majorana Zero Modes and Topological Quantum Computation. *ArXiv e-prints*, January 2015.

[3] Martin Leijnse and Karsten Flensberg. Introduction to topological superconductivity and majorana fermions. *Semiconductor Science and Technology*, 27(12):124003, 2012.

[4] Sankar Das Sarma, Chetan Nayak, and Sumanta Tewari. Proposal to stabilize and detect half-quantum vortices in strontium ruthenate thin films: Non-abelian braiding statistics of vortices in a $p_x + ip_y$ superconductor. *Phys. Rev. B*, 73:220502, Jun 2006.

[5] Gregory Moore and Nicholas Read. Nonabelions in the fractional quantum hall effect. *Nuclear Physics B*, 360(2):362 – 396, 1991.

[6] Liang Fu and C. L. Kane. Superconducting proximity effect and majorana fermions at the surface of a topological insulator. *Phys. Rev. Lett.*, 100:096407, Mar 2008.

[7] Yuval Oreg, Gil Refael, and Felix von Oppen. Helical liquids and majorana bound states in quantum wires. *Phys. Rev. Lett.*, 105:177002, Oct 2010.

[8] Roman M. Lutchyn, Jay D. Sau, and S. Das Sarma. Majorana fermions and a topological phase transition in semiconductor-superconductor heterostructures. *Phys. Rev. Lett.*, 105:077001, Aug 2010.

[9] V. Mourik, K. Zuo, S. M. Frolov, S. R. Plissard, E. P. A. M. Bakkers, and L. P. Kouwenhoven. Signatures of majorana fermions in hybrid superconductor-semiconductor nanowire devices. *Science*, 336(6084):1003–1007, 2012.

[10] M. T. Deng, C. L. Yu, G. Y. Huang, M. Larsson, P. Caroff, and H. Q. Xu. Anomalous zero-bias conductance peak in a nb–insb nanowire–nb hybrid device. *Nano Letters*, 12(12):6414–6419, 2012. PMID: 23181691.

[11] H. O. H. Churchill, V. Fatemi, K. Grove-Rasmussen, M. T. Deng, P. Caroff, H. Q. Xu, and C. M. Marcus. Superconductor-nanowire devices from tunneling to the multichannel regime: Zero-bias oscillations and magnetoconductance crossover. *Phys. Rev. B*, 87:241401, Jun 2013.

[12] P. Krogstrup, N. L. B. Ziino, W. Chang, S. M. Albrecht, M. H. Madsen, E. Johnson, J. Nygård, C. M. Marcus, and T. S. Jespersen. Epitaxy of semiconductor-superconductor nanowires. *Nature Materials*, 14:400–406, April 2015.

[13] W. Chang, S. M. Albrecht, T. S. Jespersen, F. Kuemmeth, P. Krogstrup, J. Nygård, and C. M. Marcus. Hard gap in epitaxial semiconductor-superconductor nanowires. *Nature Nanotechnology*, 10:232–236, March 2015.

[14] M. T. Deng, S. Vaitiekenas, E. B. Hansen, J. Danon, M. Leijnse, K. Flensberg, J. Nygård, P. Krogstrup, and C. M. Marcus. Majorana bound state in a coupled quantum-dot hybrid-nanowire system. *Science*, 354(6319):1557–1562, 2016.

[15] S. M. Albrecht, A. P. Higginbotham, M. Madsen, F. Kuemmeth, T. S. Jespersen, J. Nygård, P. Krogstrup, and C. M. Marcus. Exponential protection of zero modes in Majorana islands. *Nature*, 531:206–209, March 2016.

[16] Charles Kittel. *Introduction to Solid State Physics*. John Wiley & Sons, Inc., New York, 6th edition, 1986.

[17] Z. Zanolli, F. Fuchs, J. Furthmüller, U. von Barth, and F. Bechstedt. Model gw band structure of InAs and GaAs in the wurtzite phase. *Phys. Rev. B*, 75:245121, Jun 2007.

[18] Ioffe Physico-Technical Institute. Online database of electronic properties of semiconductors. *http://www.ioffe.ru/SVA/NSM/*, 2001.

[19] Thomas Ihn. *Semiconductor Nanostructures*. Oxford University Press, New York, 3rd edition, 2012.

[20] J. C. Slater. Electrons in perturbed periodic lattices. *Phys. Rev.*, 76:1592–1601, Dec 1949.

[21] Gregory H. Wannier. The structure of electronic excitation levels in insulating crystals. *Phys. Rev.*, 52:191–197, Aug 1937.

[22] Richard A. Morrow. Establishment of an effective-mass hamiltonian for abrupt heterojunctions. *Phys. Rev. B*, 35:8074–8079, May 1987.

[23] G. T. Einevoll, P. C. Hemmer, and J. Thomsen. Operator ordering in effective-mass theory for heterostructures. i. comparison with exact results for superlattices, quantum wells, and localized potentials. *Phys. Rev. B*, 42:3485–3496, Aug 1990.

[24] Handbook of Chemistry and Physics. Online database for work functions from photoelectric effect. `http://hyperphysics.phy-astr.gsu.edu/hbase/Tables/photoelec.html`.

[25] Alexander Novikov. Experimental measurement of work function in doped silicon surfaces. *Solid-State Electronics*, 54(1):8 – 13, 2010.

[26] RayMond T. Tung. Schottky-mott model. *http://academic.brooklyn.cuny.edu/physics/tung/Schottky/S-M.htm*, 2001.

[27] J. Tersoff. Schottky barrier heights and the continuum of gap states. *Phys. Rev. Lett.*, 52:465–468, Feb 1984.

[28] J. Tersoff. Schottky barriers and semiconductor band structures. *Phys. Rev. B*, 32:6968–6971, Nov 1985.

[29] M. Schluter. Theoretical models of schottky barriers. *MRS Proceedings*, 10, 1981.

[30] Richard R. Martin. *Electronic Structure: Basic Theory and Practical Methods*. Cambridge University Press, Cambridge, 7th edition, 2013.

[31] David J. Griffiths. *Introduction to Electrodynamics (3rd Edition)*. Benjamin Cummings, 1998.

[32] R. LeVeque. *Finite Difference Methods for Ordinary and Partial Differential Equations*. Society for Industrial and Applied Mathematics, 2007.

[33] H. Wang, G. Wang, S. Chang, and Q. Huang. Accelerated solution of poisson-schrodinger equations in nanoscale devices by anderson mixing scheme. *IET Micro Nano Letters*, 4(2):122–127, June 2009.

[34] C. G. Broyden. A class of methods for solving nonlinear simultaneous equations. *Mathematics of Computation*, 19:577–593, 1965.

[35] L. F. J. Piper, T. D. Veal, M. J. Lowe, and C. F. McConville. Electron depletion at inas free surfaces: Doping-induced acceptorlike gap states. *Phys. Rev. B*, 73:195321, May 2006.

[36] Natalia Tomaszewska, Lukasz Walczak, Jakub Lis, and Jacek J. Kolodziej. Surface states and charge accumulation states on reconstructed inas(001) surfaces. *Surface Science*, 632:103 – 110, 2015.

[37] Cristina Bena. Friedel oscillations: Decoding the hidden physics. *Comptes Rendus Physique*, 17(3–4):302 – 321, 2016. Physique de la matière condensée au {XXIe} siècle: l'héritage de Jacques Friedel.

[38] Herbert B. Michaelson. The work function of the elements and its periodicity. *Journal of Applied Physics*, 48(11):4729–4733, 1977.

[39] A. Vuik, D. Eeltink, A. R. Akhmerov, and M. Wimmer. Effects of the electrostatic environment on the Majorana nanowire devices. *New Journal of Physics*, 18(3):033013, March 2016.

[40] R. W. Robinett. Quantum mechanics of the two-dimensional circular billiard plus baffle system and half-integral angular momentum. *European Journal of Physics*, 24:231–243, May 2003.

[41] Wan-Tsang Wang, C. L. Wu, S. F. Tsay, M. H. Gau, Ikai Lo, H. F. Kao, D. J. Jang, Jih-Chen Chiang, Meng-En Lee, Yia-Chung Chang, Chun-Nan Chen, and H. C. Hsueh. Dresselhaus effect in bulk wurtzite materials. *Applied Physics Letters*, 91(8):082110, 2007.

[42] Dong Liang and Xuan P.A. Gao. Strong tuning of rashba spin–orbit interaction in single inas nanowires. *Nano Letters*, 12(6):3263–3267, 2012. PMID: 22545669.